Synthesis and Characterization of Garnet-Type $Li_7La_3Zr_2O_{12}$ Solid Electrolyte Materials

By

Xingxing Zhang

A dissertation submitted to the Graduate Faculty of
Auburn University
In partial fulfillment of the
Requirements for the Degree of
Doctor of Philosophy

Auburn, Alabama
May 1, 2021

Keywords: garnet electrolyte, phase stabilization, densification, site occupancy, Li-ion conductivity

Approved by

Dr. Jeffrey W. Fergus, Chair, Professor of Materials Engineering
Dr. Dong-Joo (Daniel) Kim, Professor of Materials Engineering
Dr. Majid Beidaghi, Assistant Professor of Materials Engineering
Dr. Tae-Sik Oh, Assistant Professor of Chemical Engineering

Abstract

Garnet-type $Li_7La_3Zr_2O_{12}$ (LLZO) has attracted much attention because of its promising properties for all-solid-state lithium-ion batteries, such as high ionic conductivity of 3×10^{-4} S/cm at 25°C, good chemical stability against Li metal, and good mechanical strength. In this work, using doping elements of Al and Ta through a co-precipitation method, the cubic phase garnet structure has been stabilized from the tetragonal phase structure, which has a lower ionic conductivity than that of cubic phase structure. Both Al-doped and Ta-doped LLZO pellets were porous (relative density of ~60%), thereby leading to low room temperature Li-ion conductivities (4.5×10^{-6} S/cm for Al-doped LLZO and 1.9×10^{-5} S/cm for Ta-doped LLZO).

A dense microstructure is needed to obtain a high Li-ion conductivity. $Li_{6.75}La_3Zr_{1.75}Ta_{0.25}O_{12}$ (LLZTO) with a relative density of 92% was prepared by a simple co-precipitation method with cold uniaxial pressing and sintering in a lithium-rich air atmosphere, which was created by the addition of LiOH to the LLZTO cover powder. This LiOH-containing cover powder (15Li+LiOH) has been shown to improve densification and increase the room temperature Li-ion conductivity to 4.6×10^{-4} S/cm. This 15Li+LiOH cover powder results in the formation of an Al-containing interparticle phase, which facilitates the densification of LLZTO. The aluminum concentration increases during sintering and is located in the grain boundary. As the lithium content increases, the portion of lithium occupying the 96h octahedral site increases, which due

to the higher mobility of these sites, and leads to an increase in the Li-ion conductivity.

Chlorine, which was detected in the interparticle phase for LLZTO with a short sintering time of 1 or 2 hours, is not necessary for the densification, as LLZTO prepared with no Cl-containing salt also densified under the same experiment settings. However, LLZTO prepared with no Cl-containing salt of $Zr(OH)_4$ showed a little lower relative density, which resulted in a slightly lower Li-ion conductivity than that prepared with $ZrOCl_2*8H_2O$ (2.3×10^{-4} S/cm vs 3.4×10^{-4} S/cm, all sintered at 1100°C for 16 hours).

Dense LLZO-PEO ($LiClO_4$) composites with continuous LLZO ceramic body prepared in this work have low Li-ion conductivities due to the exposure to the air in both the sample preparation and conductivity test. Composite prepared by the one-time dip process has a larger total conductivity than that prepared by multi-time dip process (1.15×10^{-6} S/cm vs 7.2×10^{-7} S/cm).

Acknowledgments

It is with my deepest appreciation to my academic advisor Dr. Jeffrey W. Fergus to whom enabled me to pursuit a Ph. D. with this dissertation. He is not only my advisor in academic research, but also a mentor in my life. I will cherish all advices and experiences he shared to me for the rest of my life. It is one of my greatest luck to study under his advices.

I would like to express my gratitude to my committee members, Dr. Dong-Joo (Daniel) Kim, Dr. Majid Beidaghi, Dr. Taesik Oh, and Dr. Minseo Park, for their constructive advices and insightful suggestions. Due to their professional suggestions on my research, my Ph.D. study could be much developed and progressed.

I would like to thank my group members and friends for the help and friendship, Honglong Wang, Ashley Baerlocher, Weili Liu, Zhicheng Zhao, Kai Roebbecke, Ralf Fischer, Yinghui Li, Mingyuan Chang, Zhongtian Zhang, Siyao Li, Eunji Lee, Hossein Talebinezhad, Lang Zhou, Jiahui Xu, Xue Li, Yuxin Cai, Yang Wen. Especially, thank Mr. Steven Moore and Ms. Cheryl Rhodes for many services in the material engineering department.

I also thank NASA for the financial support under award number NNX15AP44A.

Finally, I would like to thank my husband Cheng Chen and my family in China for their love, support and encouragement. Thank my baby girl Eileen Chen for providing me great happiness.

Table of Content

List of Tables

List of Figures

Chapter 1. Introduction

As an environment friendly and rechargeable energy system, lithium-ion batteries are receiving significant attention for various applications ranging from portable electronics to electric vehicles. Despite their promising applications, lithium-ion batteries have a few disadvantages mainly due to currently used organic carbonate liquid electrolytes. For example, the dendrite formed between anode and cathode lowers the cycling efficiency and ultimately causes internal short-circuiting of the batteries [1]. Flammability of this organic liquid electrolyte can also lead to problems. Reactions between battery components and electrolytes sparked by unforeseen local overheating or short circuits can produce a rapid increase in battery temperature and, eventually, trigger a fire or explosion [2]. Therefore, there is a great interest in finding and developing new solid-state electrolytes that are thermally and chemically stable.

Solid-state electrolytes used in lithium-ion batteries could be divided into two categories: polymers and ceramics [3]. Polymer electrolytes are formed by dissolving lithium salt, such as $LiClO_4$, $LiBF_4$, $LiN(CF_3SO_2)_2$, lithium bis(trifluoromethyl sulfonyl)-methide (LiTFSM), and bis(trifluoromethane)sulfo-nimide lithium salt (LiTFSI), in a polymer host [4,5]. Various solid polymer electrolytes are based on high molecular weight polymers, such as poly (ethylene oxide) (PEO), polyacrylonitrile (PAN), poly(vinylidene fluoride) (PVDF), and poly(methyl methacrylate) (PMMA) [6]. There are two subclasses of solid polymer electrolytes (SPE) and gel polymer

electrolytes (GPE). PEO and PVDF-based matrices are widely used to prepare SPE and GPE, respectively [7,8]. SPEs are usually prepared by solvent casting, hot pressing, lamination extrusion and so on [4,9–13]. While GPEs are mostly prepared by swelling a polymer matrix with an electrolyte solution. The swelling liquids include ethylene carbonate (EC), diethyl-carbonate (DEC), dimethyl carbonate (DMC), and so on [4,8,10,14]. Solid-state polymer electrolytes have advantages of easy processibility and flexibility. But new problems have been brought by poor electrochemical stability, and low lithium ionic conductivity and mechanical strength [6,7].

Ceramic electrolytes have high chemical and electrochemical stability and high mechanical strength, although they have high elastic moduli and are thus not flexible. Much effort has been made toward the development of solid-state ceramic electrolytes, such as perovskite-type titanates (LLTO), NASICON-like (sodium super ionic conductor) oxide electrolytes, sulfide-type and garnet-type materials [3]. The bulk ionic conductivity of LLTO could reach as high as 1×10^{-3} S/cm at room temperature (RT), but its grain boundary conductivity is quite low, typically much less than 1×10^{-5} S/cm at room temperature, and the grain boundary conduction dominates the total ionic conductivity [7]. NASICON has a disadvantage of low chemical stability to Li metal, which hinders its use as the choice for solid-state electrolytes in high voltage batteries [15]. Sulfide-type electrolytes have extremely high bulk ionic conductivity of over 10^{-2} S/cm at room temperature, but they have low chemical stability to moisture in air [16,17]. Garnet-type $Li_7La_3Zr_2O_{12}$ (LLZO) has attracted much attention because of its

promising properties. In particular LLZO has a high ionic conductivity of 3×10^{-4} S/cm at 25℃, and a grain boundary conductivity comparable to the bulk conductivity [18,19]. In addition, it shows advantages over other solid-state electrolytes, such as good chemical stability against Li metal, and good mechanical strength [20].

1.1 The structure of garnet type LLZO

Cubic phase garnet type $Li_7La_3Zr_2O_{12}$ was synthesized by Murugan et al. [18] in 2007, who reported a bulk ionic conductivity of 4.67×10^{-4} S/cm, a total ionic conductivity of 3×10^{-4} S/cm with an activation energy of 0.31 eV. In 2009, Awaka et al.[21] reported the same composition, but with a tetragonal crystal structure. The conductivity of the tetragonal garnet phase is 2-3 orders of magnitude lower than that of cubic garnet phase (e.g. a bulk ionic conductivity of 1.63×10^{-6} S/cm and grain boundary ionic conductivity of 5.59×10^{-7} S/cm). Therefore, a cubic phase garnet-type LLZO is desired.

Crystal structures of cubic and tetragonal garnet-type LLZO are shown in Figure 1.1. In the cubic phase, which is shown in Figure 1.1 (a), Li ions occupy two types of crystallographic sites. Li(1) ions are at tetrahedral sites and Li(2) ions are at distorted octahedral sites [22]. In tetrahedral phase garnet-type structure, which is shown in Figure 1.1 (b), Li ions occupy three types of crystallographic sites. Li(1) ions occupy tetrahedral sites, and Li(2) and Li(3) ions occupy two distorted octahedral sites [21].

The lower conductivity of the tetragonal crystal structure has been attributed to the

ordering of Li atoms and Li vacancies in the tetrahedral and octahedral sites, as the tetrahedral or distorted octahedral sites are either full or empty [23]. In the cubic phase structure, however, the Li sub-lattice is disordered, both Li sites are partially occupied and the Li ion vacancies are also not ordered [23–25]. In the tetragonal phase structure, all Li sites are fully occupied (g=1), while a reduced site occupancy of Li(1) site (g=0.94) and Li(2) site (g=0.35) were found in the cubic phase structure [21,26]. Thus, compared to the tetragonal phase, in the cubic phase structure the larger number of lithium vacancies and the disorder in the Li sub-lattice enable a lower activation energy for Li motion, which enhance the Li-ion conductivity [27].

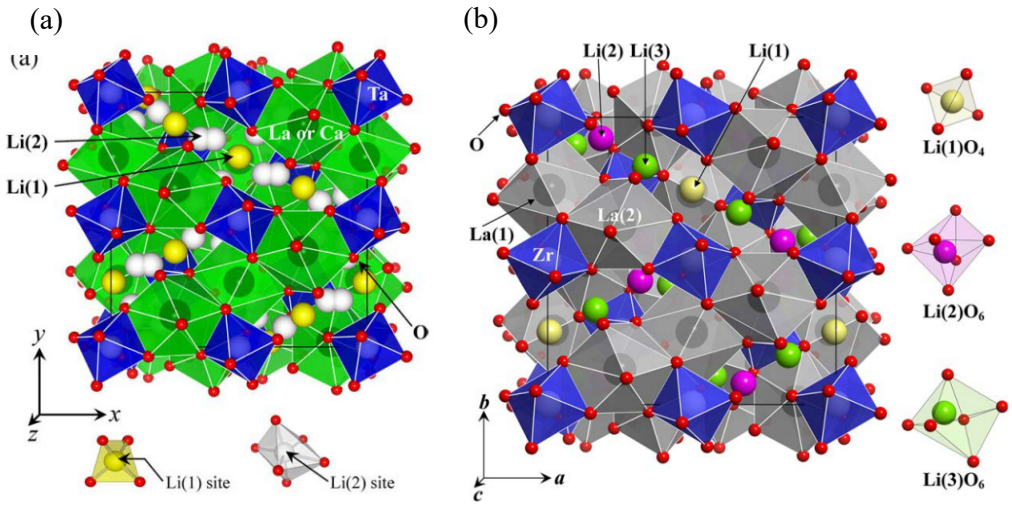

Figure 1.1 Crystal structure of (a) cubic phase [22], (b) tetragonal phase [21]

1.2 The stabilization of cubic garnet-type phase by elemental doping

The driving force behind the tetragonal to cubic transition was studied by Bernstein et al. using MD method together with variable cell shape density-functional theory (DFT) [23]. In cubic phase structure, as Li sites are partially occupied, the Li sub-lattice is always disordered. While in the tetragonal phase structure it is ordered, as Li sites are fully occupied [23]. Besides, the tetragonal to cubic transition temperature was found to decrease with increasing Li vacancy concentration [23].

Elemental doping is an effective way to stabilize the cubic phase structure. Some works claim that the doping elements could stabilize the cubic phase by substitution, change the lithium concentration and create the lithium vacancies [7,23,28]. The elemental doping introduces vacancies into the Li sublattice because of the charge compensation, increasing the overall entropy and reducing the free energy gain from ordering, eventually leading to disorder and a transition to cubic symmetry, in other words, stabilizing the cubic phase [23].

The substitution of Al, Ga, Fe for Li [2,29–33], Rb, Nd, Ca, Ba for La,[34–36]and/or Nb, Ta, W for Zr [34,37–39] have been reported. Regardless of specific dopant or doping site used, a minimum Li vacancy concentration of 0.4 per formula unit (pfu) is needed to stabilize the cubic phase [23], which is based on variable cell shape density-functional theory (DFT) plus molecular dynamics (MD) simulation of LLZO. To determine which cations have high solubility in cubic LLZO, the defect energies and site preference of all possible dopants in cubic LLZO was calculated by

Miara et al. using density-functional theory (DFT) [28]. Figure 1.2 shows the site and oxidation state preference for the dopant elements studied [28]. The dopant of Al^{3+}(Li) is widely used as it is an inexpensive material and could be introduced into the garnet structure unintentionally by using the Al_2O_3 crucible during the sintering [2]. From Figure 1.2, the dopant of Ta^{5+}(Zr) has a defect energy of 0.94 eV, which is smaller than Al^{3+}(Li) of 1.36 eV [28]. The high conductivity of over 10^{-3} S/cm was reported for Ta-doped LLZO [40]. However, the repeatability of the reported conductivity value needs further confirmation as lower conductivity values for the similar composition were also reported [41–45]. Therefore, in this work, Al and Ta were selected as the doping elements.

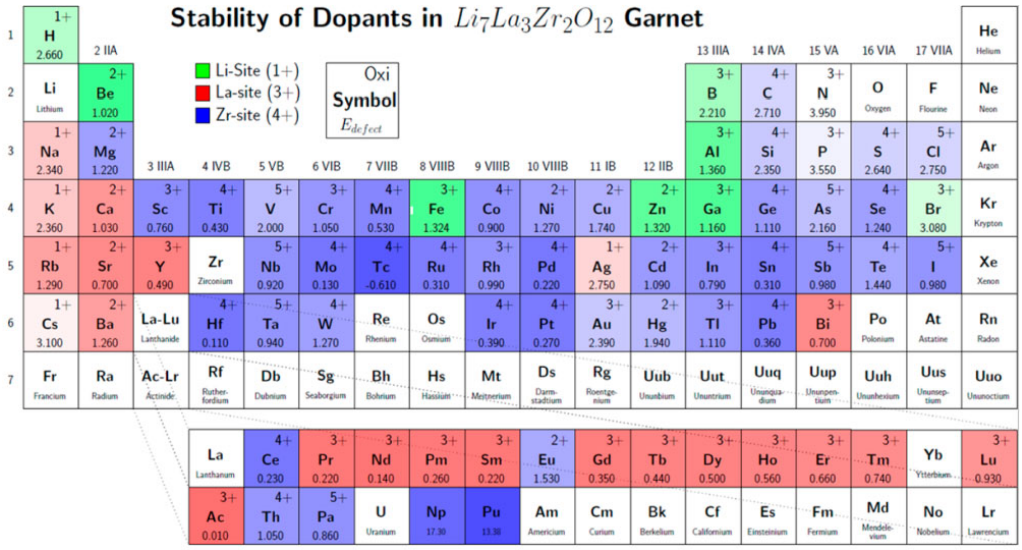

Figure 1.2 Site and oxidation state preference for the dopant elements in cubic LLZO studied. The color shows the most stable cation site (green for Li-site, red for La-site, and blue for Zr-site). The darker colors signify lower defect energy, such that Al^{3+}(Li) is darker than B^{3+}(Li). The box also shows the preferred oxidation state and the defect energy (in eV) [28].

The doping element of Al substitutes for Li. Al contamination from the crucible was found to help with the stabilization of the cubic phase by Gerger et al. in 2011 [2]. Aluminum introduces vacancies into the Li sublattice because of the charge compensation, thereby increasing the overall entropy and reducing the free energy gain from ordering, eventually stabilizing the cubic phase [23]. Gerger et al. [2] suggested that the reaction between Al_2O_3 from the crucible and LiOH or Li_2CO_3 resulted in the production of a minor liquid phase, which has also been reported in other works [29,46]. The Al molar concentration will affect the garnet-type structure. It is reported that the tetragonal LLZO formed at Al molar concentration between 0.074 and 0.1 mole pfu, while cubic LLZO formed at an amount of 0.204-0.389 mole pfu[47]. At a fixed Al concentration of 0.24 mole pfu, when the Li content was further increased from 6.24 to 7.32 mole pfu, a transformation from cubic to tetragonal occurred [47].

The doping element of Ta substitutes for Zr. Ta could stabilize the cubic phase with a doping level at low as 0.2 mole pfu [48]. And the lattice parameter of Ta-doped LLZO is found to decrease linearly with the increasing Li content [40]. The conductivity values of Ta-doped LLZO could reach 1×10^{-3} S/cm [40], while the conductivity of Al-doped LLZO is reported to be around 3×10^{-4} S/cm [49–52]. Therefore, it is our interest to study these two different doping elements of Al and Ta.

1.3 Li-ion Conductivity and Transport Study

1.3.1 AC EIS Impedance Study

Alternating current (AC) electrochemical impedance spectroscopy (EIS) is the most common way to characterize the conductivity of solid electrolytes. Figure 1.3 shows a typical AC impedance plot (complex plane plots, imaginary part Z" vs the real part Z') of $Li_{6.5}La_{2.5}Ba_{0.5}ZrTaO_{12}$ [53]. The coupling of R (resistances) and CPE (constant phase element) produces a depressed semicircle. The "tail" appears at low frequencies and indicates the conductivity of the material is ionic in nature [25]. The solid line in Figure 1.3 represents fitted data based on an equivalent circuit of $(R_bCPE_b)(R_{gb}CPE_{gb})CPE_e$, the subscript b, gb and e refers to bulk, grain boundary, and electrode responses. The ionic conductivity σ could be determined by equation, $\sigma=(RL)/A$, where R is the resistance, L is the thickness of the pellet and A is the cross-sectional area of the pellet.

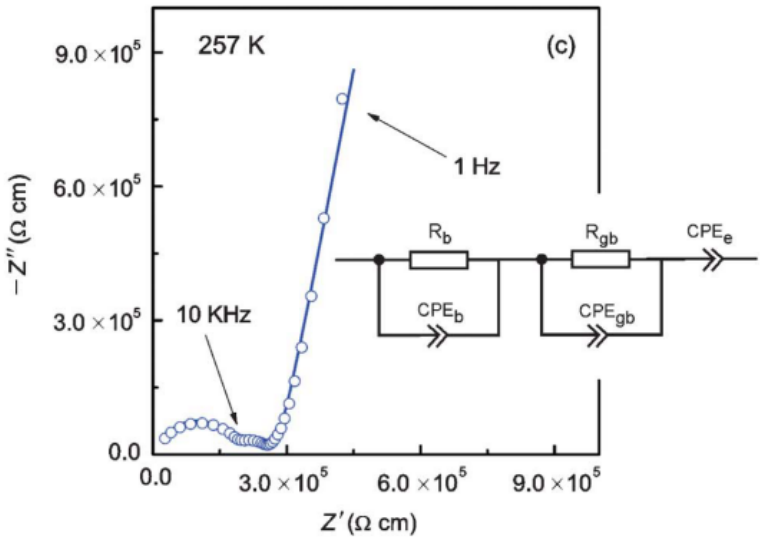

Figure 1.3 Typical AC impedance plot of $Li_{6.5}La_{2.5}Ba_{0.5}ZrTaO_{12}$ measured in air at 16°C using Au electrodes [53]

Figure 1.4 shows a different equivalent circuit of $(R_tCPE_t)CPE_e$ [54]. The tail at low frequency also indicates the investigated materials is ionically conducting in nature. At high frequency, the semicircle represents the total (bulk + grain) ionic conductivity. In this case, the bulk and grain boundary resistance could not be well resolved [54], which is consistent with other works [43,47,55,56].

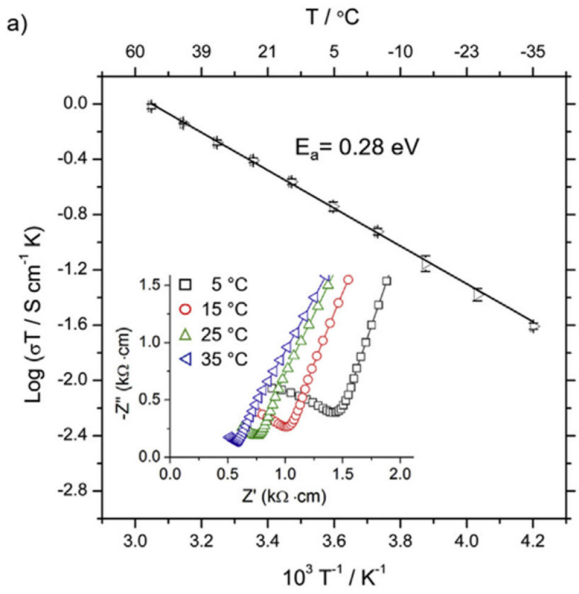

Figure 1.4 AC impedance plot of $Li_{6.25}Ga_{0.25}La_3Zr_2O_{12}$ measured in air at selected temperatures [54]

AC EIS is a powerful technique to study the impedance characteristics, but interpretation of the results can be complicated and is sometimes ambiguous. The results are typically interpreted using equivalent circuit models, which are analogs, not physicochemical models. In addition, several different electrical equivalent models could give similar fitted lines [57]. Table 1.1 shows capacitance values and their possible interpretation [58]. Figure 1.5 [49] shows a similar AC impedance with Figure 1.3, but the equivalent circuit interpretation is different. The high frequency semicircle is assigned to grain-boundary contribution, while the intermediate frequency semicircle is characteristic of a surface layer effect.

Table 1.1 Capacitance values and their possible interpretation [58]

Capacitance (F)	Phenomenon Responsible
10^{-12}	bulk
10^{-11}	minor, second phase
10^{-11}-10^{-8}	grain boundary
10^{-10}-10^{-9}	bulk ferroelectric
10^{-9}-10^{-7}	surface layer
10^{-7}-10^{-5}	sample-electrode interface
10^{-4}	electrochemical reaction

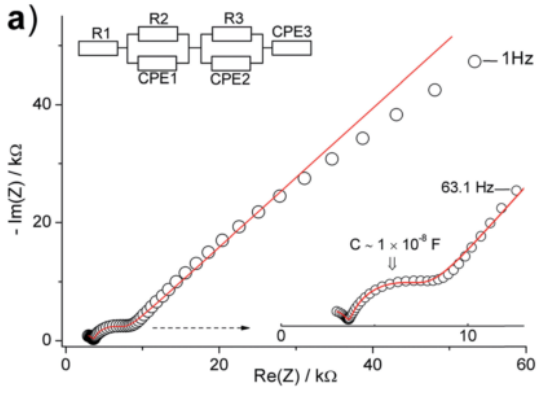

Figure 1.5 A typical AC impedance plot of LLZO (2 wt.% Al) calcined at 1000°C measured at room temperature using gold electrodes [49]

1.3.2 Li-ion conductivity of Al-doped and Ta-doped LLZO

The substitution of one Al ion on one Li site creates twice as many lithium vacancies compared to substitution of one Ta at Zr site (Kröger-Vink notation, $[Al_{Li}^{\cdot\cdot}]=2[V_{Li}^{\prime}]$ vs $[Ta_{Zr}^{\cdot}]=[V_{Li}^{\prime}]$). In addition, Al ions occupy Li(1) site, which is important for Li ion conduction pathway [2,38], while Ta ions reside in the Zr site. Therefore, the Li ion conductivity would be affected differently by the two dopants. LLZO pellets doped c Table 1.2 shows that the highest conductivity values for the Al-doped is smaller than that of Ta-doped (4×10^{-4} S/cm [47] vs 8.7×10^{-4} S/cm [38]).

Table 1.2 Reported Li-ion conductivity and the corresponding composition of Al-doped and Ta-doped LLZO

Nominal composition	Molar ratio					RT total	Ref.
	Li	La	Zr	Ta	Al	σ_{Li+} (S/cm)	
$Li_7La_3Zr_2O_{12}$	6.1	3	1.8	-	0.18	-	[2]
$Li_{6.75}La_3Zr_{1.75}Ta_{0.25}O_{12}$	6.4	3.11	1.75	0.25	0.15	6.55×10^{-4}	[59]
$Li_{6.75}La_3Zr_{1.75}Ta_{0.25}O_{12}$	-	-	-	-	-	8.7×10^{-4}	[38]
$Li_{6.5}La_3Zr_{1.5}Ta_{0.5}O_{12}$	6.39	3	1.48	0.5	-	6.1×10^{-4}	
$Li_{6.15}Al_{0.2}La_3Zr_{1.75}Ta_{0.25}O_{12}$	-	-	-	-	-	3.7×10^{-4}	
$Li_{6.4}La_3Zr_{1.4}Ta_{0.6}O_{12}$	6.32	2.91	-	0.6	0.08	1×10^{-3}	[40]
$Li_{6.28}Al_{0.24}La_3Zr_2O_{12}$	6.24	-	-	-	0.24	4×10^{-4}	[47]
$Li_{6.25}Al_{0.25}La_3Zr_2O_{12}$	5.65	2.97	1.88		0.63	1.81×10^{-4}	[56]

1.3.3 Dynamic behavior of lithium in tetragonal and cubic LLZO

Li jump statistics were studied by Chen et.al through a novel density-based clustering of trajectories (DCT) method which was based on *ab initio* molecular dynamic (MD) simulation [60]. This work noticed that in cubic phase LLZO despite the high jump rate, it is highly probable that Li returns to the original site after hopping to the neighboring site, which is referred to a back-and-forth type jump. At room temperature, the Li jumps consist mostly of a back-and-forth type. As the net displacement of the Li is zero in the back-and-forth jumps, this type of jumps does not contribute to the effective diffusion. This study also shows that increasing vacancy concentration is an effective strategy to reduce the back-and-forth jumps, thereby resulting in more effective Li diffusional rates [60]. Li diffusion is relatively short ranged because continuously open channels are missing. When Li vacancy concentration increases, more sites will be created for the hopping of Li ions. Therefore, it is also expected by this work that doping the LLZO with higher valence cations increase the Li vacancy concentration and enhance the Li self-distribution [60].

The lithium ion self-diffusion coefficient and the diffusion barriers as function of lithium ion concentration was calculated by Andriyevsky et al. based on MD simulation [61]. In tetragonal LLZO, activation energy (E_a) of lithium ion diffusion was found to increase with the unit cell lithium content. As a result, the diffusion coefficient

($D=D_0exp(-E_a/kT)$) was found to be a decreasing function of the unit cell lithium content (D_0 is a prefactor). This study also found out that the larger the frequency width of the spectral density of states lithium ion distribution, the larger is the anharmonicity of the effective lithium ion vibration, which facilitates bond breaking and migration events in the material. Further, this leads to an overall increase of the diffusion coefficient [61].

1.3.4 Li site occupancy at different Li content

Lithium on equilibrium tetragonal site was found to be immobile compared to that in the octahedra site by O'Callaghan et al. [62] using solid state nuclear magnetic resonance (NMR). This research group also found that lithium ions on tetrahedral sites form an ordered structure and do not exchange with the lithium in the octahedral sites. Therefore, this study indicates that the lithium conduction in the garnet structure occurs via a network of distorted oxide octahedra [62].

The Li ions on the octahedral site (96h) are highly mobile and are involved in the hopping from one edge shared oxide octahedron to another, so when the occupancy at 96h Li site is low, the Li ion conductivity is also low (10^{-6} S/cm) [63–65]. An increase in the concentration of Li ions on the 96h Li site significantly improves the conductivity [40,50,65–68]. The Li ion on the tetrahedral site is referred to Li 24d. Li occupancy can be determined using Rietveld structure refinements based on neutron diffraction or x-

ray diffraction. Reported work of Li occupancy on different Li site and the corresponding Li-ion conductivity are listed in Table 1.3 and plotted in Figure 1.6 and Figure 1.7.

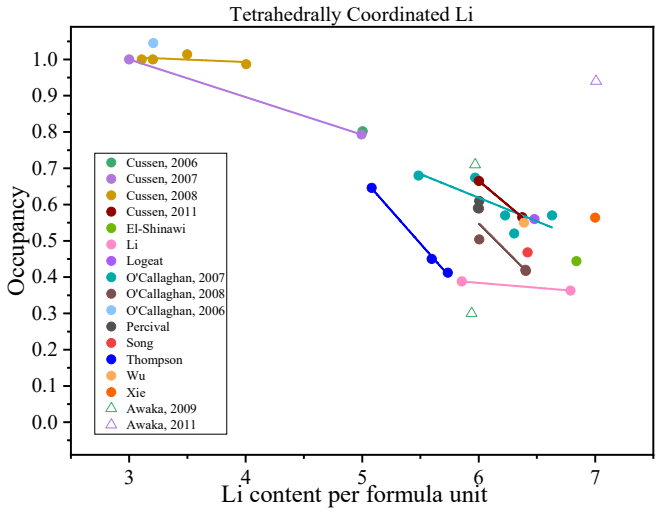

Figure 1.6 The occupancy of tetrahedral site (24d) occupied by Li ions at different Li concentrations

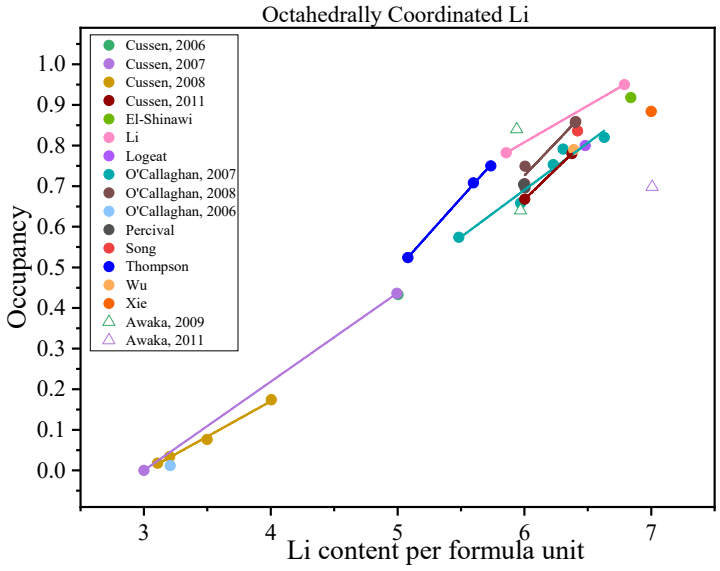

Figure 1.7 The occupancy of octahedral site (96h) occupied by Li ions at different Li concentrations

Table 1.3 The nominal composition, Li content used in the refinement, Li site occupancy from Rietveld refinement (room temperature) and RT total σ_{Li+} for different samples

Nominal composition	Li content in refinement	Li 24d occupancy	Li 96h occupancy	RT σ_{Li+} (S/cm)	Radiation	Ref.
$Li_3Nd_3Te_2O_{12}$	3.2	1.045	0.012	-	neutron	[64]
$Li_3Nd_3W_2O_{12}$	3	1	0		neutron	[69]
$Li_5La_3Sb_2O_{12}$	5	0.793	0.436	-		
$Li_{3.1}Nd_3Te_{1.9}Sb_{0.1}O_{12}$	3.1	1	0.018	-	neutron	[62]
$Li_{3.2}Nd_3Te_{1.8}Sb_{0.2}O_{12}$	3.2	1	0.034	-		
$Li_{3.5}Nd_3Te_{1.5}Sb_{0.5}O_{12}$	3.5	1.014	0.076	-		
$Li_4Nd_3Te_{0.5}Sb_{1.5}O_{12}$	4	0.987	0.174	-		
$Li_5La_3Ta_2O_{12}$	5	0.802	0.433	-	neutron	[70]
$Li_{5.5}La_3Zr_{0.5}Ta_{1.5}O_{12}$	5.08	0.646	0.524	8.00×10^{-5}	neutron	[67]
$Li_{6.25}La_3Zr_{1.25}Ta_{0.75}O_{12}$	5.60	0.45	0.708	3.90×10^{-4}		
$Li_{6.5}La_3Zr_{1.5}Ta_{0.5}O_{12}$	5.74	0.412	0.75	8.16×10^{-4}		
$Li_6CaLa_2Ta_2O_{12}$	5.97	0.71	0.64	2.2×10^{-6}	X-ray	[22]
$Li_6BaLa_2Ta_2O_{12}$	5.94	0.3	0.84	1.3×10^{-5}		
$Li_{5.5}Ba_{0.5}La_{2.5}Ta_2O_{12}$	5.48	0.68	0.574	-	neutron	[71]
$Li_6BaLa_2Ta_2O_{12}$	5.97	0.674	0.658			
$Li_{6.2}Ba_{1.2}La_{1.8}Ta_2O_{12}$	6.23	0.57	0.753	-		
$Li_{6.4}Ba_{1.4}La_{1.6}Ta_2O_{12}$	6.31	0.52	0.791	-		
$Li_{6.6}Ba_{1.6}La_{1.4}Ta_2O_{12}$	6.63	0.57	0.82	-		
$Li_6La_2CaNb_2O_{12}$	6	0.61	0.696	-	neutron	[72]
$Li_6La_2SrNb_2O_{12}$	6	0.59	0.704	-		
$Li_6SrLa_2Sb_2O_{12}$	6	0.504	0.749	-	neutron	[73]
$Li_{6.4}Sr_{1.4}La_{1.6}Sb_2O_{12}$	6.4	0.42	0.857	-		
$Li_6SrLa_2Ta_2O_{12}$	6	0.589	0.706	-		
$Li_{6.4}Sr_{1.4}La_{1.6}Ta_2O_{12}$	6.4	0.417	0.859	-		
$Li_6CaLa_2Sb_2O_{12}$	6	0.665	0.668	-	neutron	[74]
$Li_{6.4}Ca_{1.4}La_{1.6}Sb_2O_{12}$	6.4	0.565	0.78	-		
$Li_{6.40}Ga_{0.20}La_3Zr_2O_{12}$	6.4	0.55	0.79	8.7×10^{-4}	neutron	[66]
$Li_{6.5}La_3Ta_{0.5}Zr_{1.5}O_{12}$	6.5	0.56	0.8	-	neutron	[75]
$Li_{6.5}La_3Zr_{1.5}Ta_{0.5}O_{12}$	5.86	0.388	0.782	9.2×10^{-4}	neutron	[40]
$Li_7La_3Zr_2O_{12}$	6.79	0.363	0.95	1.4×10^{-4}		
$Li_7La_3Zr_2O_{12}$	7	0.564	0.884	-	neutron	[76]
$Li_7La_3Zr_2O_{12}$ with 2 wt.%Al	6.84	0.444	0.918	3×10^{-4}	neutron	[77]
$Li_7La_3Zr_2O_{12}$	7	0.94	0.698	-	X-ray	[26]
$Li_{7.1}La_3Zr_{1.95}Ca_{0.05}O_{12}$	6.42	0.468	0.836	5.2×10^{-4}	neutron	[68]

The octahedral Li occupancy ($Li_{octahedral}$) is calculated as $Li_{octahedral}$ = 2*Occupancy $_{Li96h}$, as there are two distorted octahedral 96h sites inside the Li(2) octahedra. In structural models in the literature works using a combination of the 48g (center octahedral site) and 96h (distorted octahedral site), the octahedral Li occupancy is calculated as $Li_{octahedral}$ = 2*Occupancy $_{Li96h}$+ Occupancy $_{Li48g}$, as the Li(2) octahedra may contain one 48g site or two 96h sites inside the Li(2) octahedra. In Figure 1.6 and 1.7, each point represents one Li content while the lines are the fitting lines for sets of data when multiple lithium contents are reported in given work. The occupancy results from Rietveld structure refinements based on x-ray diffraction are labeled by symbol "△", while others labeled by symbol "●" are based on neutron diffraction data. From Figure 1.6 and 1.7, in the range of 3-7 Li per formula unit (pfu), it is concluded that the occupancy of 24d Li site decreases and 96h Li site increases with the increasing Li content. There is one report of a 24d Li site occupancy of 0.94 at 7 Li pfu which was obtained from x-ray data and is significantly higher than other reports [26].

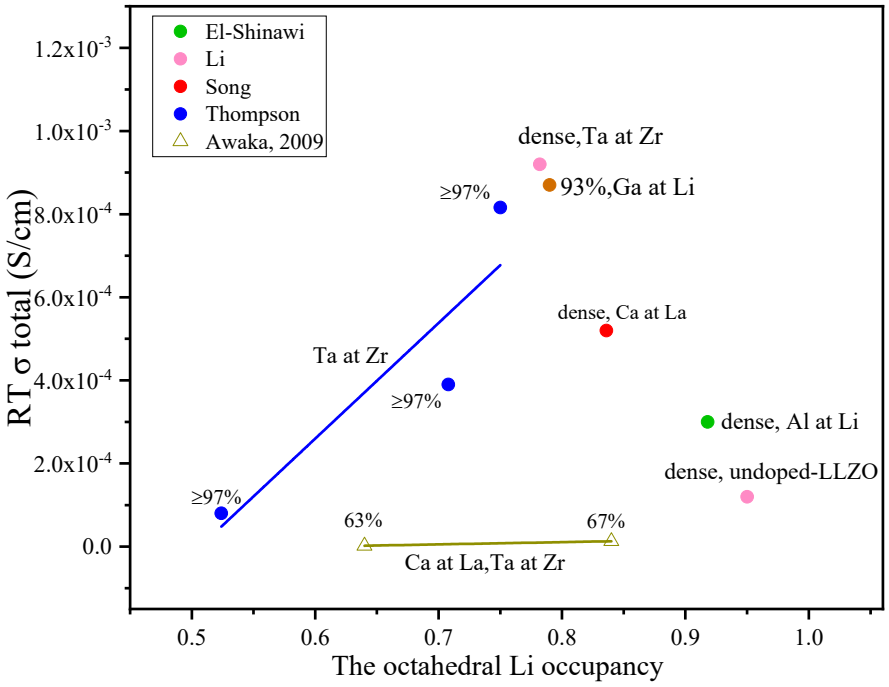

Figure 1.8 RT total σ_{Li+} at different 96h Li site occupancy, ● work based on neutron diffraction, △work based on XRD

As it is reported that the occupancy at 96h Li site plays an important role in the RT total σ_{Li+} [40,50,65–68], to determine the relationship between 96h Li site occupancy and the conductivity, the RT total σ_{Li+} at different 96h Li site occupancy are plotted in Figure 1.8 [22,40,67,68,77]. Each point represents one Li content while the lines are the fitting lines for sets of data when multiple lithium contents are reported in given work. The two lines show that with the similar relative density, the RT total σ_{Li+} increases with the increasing 96h Li site occupancy.

As the maximum occupancy of Li^+ in the garnet structure is 7.5 pfu [34,78,79] and maximum Li content in Table 1.3 is 7 pfu, the focus of this study is to study the Li site

occupancy and the corresponding RT total σ_{Li+} with a high Li content in the range of 6.5-7.5 pfu.

1.4 The densification of LLZO

In addition to a cubic crystal structure, a dense microstructure is also needed to obtain a high Li-ion conductivity, as porous microstructures result in much lower Li-ion conductivities (e.g. 8.9×10^{-6} S/cm at 25°C [80]). Successful approaches introduce a secondary driving force for densification, e.g. hot-pressing [47,81,82], hot isostatic pressing [83,84], field assisted sintering / spark plasma sintering / induced hot pressing [68,85–90]. In hot-pressing, the LLZO powders are hot-pressed at high temperature with certain pressure for some time under air [47,81,82]. In hot pressing, the uniaxial pressure is used. During hot isostatic pressing, the pellet is isostatically pressed under high gas pressure and sintered at the same time [83,84]. The way of applying the pressure is the difference between hot pressing and hot isostatic pressing. Field assisted sintering is also known as spark plasma sintering, induced hot pressing. Compared to hot pressing, in field assisted sintering, a pulse current was applied through the sample as well as the surrounded graphite die. The current generates large local joule heat to facilitate sintering [68,85–90]. In all above discussed techniques, the samples are sintered at 1000-1100°C with a sintering time shortened to less than 1 hour. However, these methods are high cost and are not suitable for continuous mass production.

Table 1.4 The additives used in LLZO, the corresponding densities and room temperature (RT) total Li-ion conductivities

Additive	Dopant	Synthesis	No additive		**With additive**		Reference
			Relative density (%)	RT σ_{total} (S/cm)	**Relative density (%)**	**RT σ_{total} (S/cm)**	
Li_4SiO_4	Al	Sol-gel, 1200°C, 12 h	79	1.1×10^{-4}	**96**	**6.1×10^{-4}**	[91]
Li_3BO_3					**76**	**1.3×10^{-5}**	
Li_3PO_4					**79**	**3.5×10^{-4}**	
$La_2Zr_2O_7$	Ta	Solid-state reaction, cold uniaxial pressing, 1100°C, 10 h	77	3.5×10^{-5}	**90**	**1.9×10^{-4}**	[92]
Li_2O	Ta	Solid-state reaction, 1170°C, 6 h	92	2.2×10^{-4}	**97**	**6.4×10^{-4}**	[43]
LiOH	Nb	Sol-gel, 900°C, 10 h	50	8×10^{-7}	**77**	**2.0×10^{-6}**	[93]
$LiBO_2$	Nb	Sol-gel, 900°C, 10 h	55	1×10^{-7}	**93**	**3×10^{-5}**	[94]
Li_3BO_3					**86**	**7×10^{-5}**	

When the simple method of cold uniaxial pressing and sintering in air is used, additives are typically needed to obtain high density, details of which could be found in Table 1.4 [43,91–94]. Additions of $La_2Zr_2O_7$ and Li_2O to Ta-doped LLZO and Li_4SiO_4

to Al-doped LLZO have led to improvements of 6-17% in density which increased conductivity 3-5 times [43,91,92]. Even larger increases in densities have been reported with additions of LiOH, Li_3BO_3 and $LiBO_2$ to Al- and Nb-doped LLZO, but the conductivities are all smaller than 1×10^{-4} S/cm [91,93,94]. Samples with conductivities larger than 1×10^{-4} S/cm were sintered at temperature above 1100°C or prepared with cold uniaxial pressing [43,91,92].

1.5 LLZO based composites

LLZO has good chemical stability and high ionic conductivity, but they are rigid and brittle, which may result in poor contact with electrodes and mechanical failure [95,96]. Solid polymers are flexible and easy to prepare, but their low ionic conductivity hinders them to be widely applied in solid-state lithium ion batteries [4]. Composite electrolytes, which combine the advantages of both LLZO and solid polymer electrolytes, are promising solid electrolytes with high ionic conductivity, good chemical stability and mechanical properties. Table 1.5 lists Li-ion conductivity of several composites with LLZO.

Table 1.5 Chemical composition and ionic conductivity of different LLZO based composites

Composite	Weight ratio (SPE/Li compound: LLZO)	Total σ_{Li+} (S/cm)	Test temperature	Ref.
PEO-$LiClO_4$	-	1×10^{-7}	27°C	[4]
		10^{-5}-10^{-8}	35-65°C	[97]
t-$Li_7La_3Zr_2O_{12}$(particles)-PEO ($LiClO_4$)	0.475:0.525	4.42×10^{-4}	55°C	[98]
c-$Li_{6.4}La_3Zr_2Al_{0.2}O_{12}$(particles) -PEO ($LiClO_4$)-TEGDME	0.4:0.4:0.2	5.15×10^{-5}	RT	[99]
c-$Li_{6.4}La_3Zr_{1.4}Ta_{0.6}O_{12}$ (particles)-PEO ($LiClO_4$)	0.7:0.3	4.8×10^{-4}	60°C	[100]
PAN($LiClO_4$)	-	4.06×10^{-7}	20°C	[101]
c-$Li_{6.5}La_3Zr_{1.5}Ta_{0.5}O_{12}$ (nanowires) - PAN($LiClO_4$)	0.95:0.5	1.5×10^{-4}	20°C	[101]
c-$Li_{6.28}La_3Zr_2Al_{0.24}O_{12}$ (nanowires) - PAN($LiClO_4$)	0.95:0.5	1.27×10^{-4}	20°C	[101]
c-$Li_{6.4}La_3Zr_2Al_{0.2}O_{12}$ (nanowires)- PEO(LiTFSI)	-	2.5×10^{-4}	RT	[102]
c-$Li_{6.1}La_3Zr_2Al_{0.3}O_{12}$-$Li_3BO_3$	0.064:1	1×10^{-4}	30°C	[103]
c-$Li_7La_3Zr_2O_{12}$-Li_3BO_3	0.08:1	1.94×10^{-5}	28°C	[104]
Li_3PS_4	-	1.6×10^{-4}	25°C	[105]
c-$Li_7La_3Zr_2O_{12}$	-	4.0×10^{-4}	25°C	[105]
c-$Li_7La_3Zr_2O_{12}$-Li_3PS_4	0.7:0.3	5.36×10^{-4}	25°C	[105]
c-$Li_7La_3Zr_2O_{12}$-$Li_{0.35}La_{0.55}TiO_3$	0.95:0.05	1.2×10^{-4}	RT	[106]
t-LLZO is tetragonal phase LLZO, c-LLZO is cubic phase LLZO				

LLZO-PEO ($LiClO_4$) composite membrane could be obtained by tape casting method [99,101,107] and has a higher ionic conductivity (4.42×10^{-4} S/cm at 55°C [98]) than PEO-$LiClO_4$ composite (10^{-5}-10^{-8} S/cm in the range of 358-65°C [97]). LLZO electrolytes in different shapes, such as nanowires and particles, have been fabricated. In the shape of nanowires, an ionic conductivity of 1.5×10^{-4} S/cm at 55°C was obtained by Yang et al. [101]. This research found different composite samples of undoped, Al-doped and Ta-doped cubic phase LLZO nanowires have similar ionic conductivities. Also in the shape of nanowires, Fu et al. obtained an ionic conductivity of 2.5×10^{-4} S/cm at room temperature [102]. In the shape of particles, Zheng et al. prepared LLZO-PEO ($LiClO_4$) films with cubic phase Al-doped LLZO particles, and a plasticizer of tetraethylene glycol dimethyl ether (TEGDME). An ionic conductivity of 5.15×10^{-5} S/cm at room temperature was obtained [99]. Another group prepared similar composites with cubic LLZO particles in PEO ($LiClO_4$) matrix. And an ionic conductivity of 4.8×10^{-4} S/cm at 60°C was obtained [108]. By using the same shape of particles but tetragonal phase LLZO, LLZO-PEO ($LiClO_4$) films was found to have an ionic conductivity of 4.42×10^{-4} S/cm by Choi et al. [98]. In this work, PEO-$LiClO_4$ is selected as PEO has relatively high ionic conductivity and good stability with lithium metal [3], and $LiClO_4$ is a common lithium salt.

Lithium compounds instead of polymer have also been used with LLZO to prepare composites, such as Li_3BO_3, $LiBO_2$, Li_3PS_4, and so on. Li_3BO_3 was used as a sintering additive for producing LLZO at a low sintering temperature [103,104]. The ionic

conductivity was found to be different with different Li_3BO_3 content. It is 1×10^{-4} S/cm when the mole ratio of Li_3BO_3/LLZO was 0.68 [103]. When the mole ratio is 0.84 (recalculated from the weight percentage of 8 wt.% BO_3), the ionic conductivity is 1.94×10^{-5} S/cm [104]. Li compound of $LiBO_2$ was also used to decrease the sintering temperature of LLZO. However, impurity of $Li_2Zr_2O_7$ was detected in this case, while pure cubic phase was obtained in the case of Li_3BO_3 [109]. Li_3PS_4-LLZO composite was found to have the best ionic conductivity of 5.36×10^{-4} S/cm when the mass ratio was 70:30 (Li_3PS_4 : LLZO) [105]. Perovskite type lithium lanthanum titanate has also been reported to be used with LLZO to prepare composites. $Li_{0.35}La_{0.55}TiO_3$ sintered with 5 wt.% LLZO exhibited an ionic conductivity of 1.2×10^{-4} S/cm [106]. In this work, several types of second phase will be tried, such as perovskite-type titanates (LLTO), NASICON-like oxide electrolytes, LiOH, and so on.

1.6 Research objective

The research objective of this project is the preparation of garnet-type LLZO with high Li-ion conductivity and the understanding of the Li transport.

LLZO with different doping elements of Al and Ta will be prepared and characterized. Simple techniques for obtaining dense Ta-doped garnet-type $Li_7La_3Zr_2O_{12}$ solid electrolyte materials will be studied. The mechanism for the densification would also be the focus of this work.

A detailed study of the Li ion transport properties of LLZO will be studied. The conductivity and activation energy will be studied by AC impedance. The occupancy of different Li site would be obtained from the neutron diffraction to better understand how the crystal structure affect the Li-ion conductivity.

LLZO based composites of LLZO-PEO ($LiClO_4$) with a continuous LLZO ceramic body will be prepared by a dipping process and characterized by AC impedance for conductivity, scanning electron microscope for morphology.

Chapter 2. Experimental methods

2.1 The synthesis of LLZO by co-precipitation method

Garnet-type LLZO was prepared by the co-precipitation method. LiOH (Alfa, anhydrous, 98%), $La(OH)_3$ (Alfa, 99.95% REO), $ZrOCl_2 \cdot 8H_2O$ (Alfa, 98%), $Zr(OH)_4$ (Sigma, 97%), Ta_2O_5 (Alfa, 99%, metal basis), and Al_2O_3 (Johnson Matthey, 99.9+ %, metals basis), nitric acid (Alfa, 67-70%), ammonium hydroxide (Alfa, 5.0 N) were used as starting materials. Due to evaporation losses of lithium during heat treatment, 15 wt.% excess of LiOH was added. The process flow is shown in Figure 2.1(a). According to the nominal composition, such as $Li_{6.28}La_3Zr_2Al_{0.24}O_{12}$ and $Li_{6.75}La_3Zr_{1.75}Ta_{0.25}O_{12}$, the calculated amount of LiOH and $La(OH)_3$ were dissolved in HNO_3 and $ZrOCl_2 \cdot 8H_2O$ in deionized water, respectively. Before mixing these two solutions, Ta_2O_5 or Al_2O_3 powders were added into the nitric acid solution. After mixing, the precipitates were obtained by the addition of NH_4OH to the mixture. The final mixture has a pH value of 10 or above. The precipitates were dried at 80°C for 48 hours and then heated at 700°C under flowing air for 2 hours. The dried powders or the dried powders with additional LiOH were ball milled with zirconia balls in a planetary ball milling machine (Across International, PQN2 gear-drive planetary ball mill) at 500 rpm for 4 hours with 2-propanol as the dispersing reagent. The ratio of amount of the powders, 2-propanol and zirconia balls is 1:1:3. After drying at 80°C for 24 hours, the powders were cold pressed into pellets (10 mm in diameter and 1-3 mm in thickness) at a pressure of 200 MPa.

The pellets were fully covered with cover powders, placed in an alumina crucible or a modified alumina crucible (shown in Figure 2.1 (b)), with an alumina lid and sintered in air with a heating rate of 1°C/min to 1100°C for 1-32 hours. The modified alumina crucible was used in the densification of LLZTO. And the reason of using this crucible is presented in Appendix I. Other experiments all used the original alumina crucible.

During sintering, the pellets were covered with powders to reduce the loss of lithium which is shown in Figure 2.2. The cover powder is the powder after the heat-treatment of 700°C and before the ball milling and has the same composition of the pellets. Four columns, with four pellets in each column, of samples were sintered at one time. Only the middle two pellets were used, as the bottom pellet was in contact with the crucible and the top pellet exhibited different sintering behavior, presumably because the atmosphere was different as it was closer to the air above the cover powder.

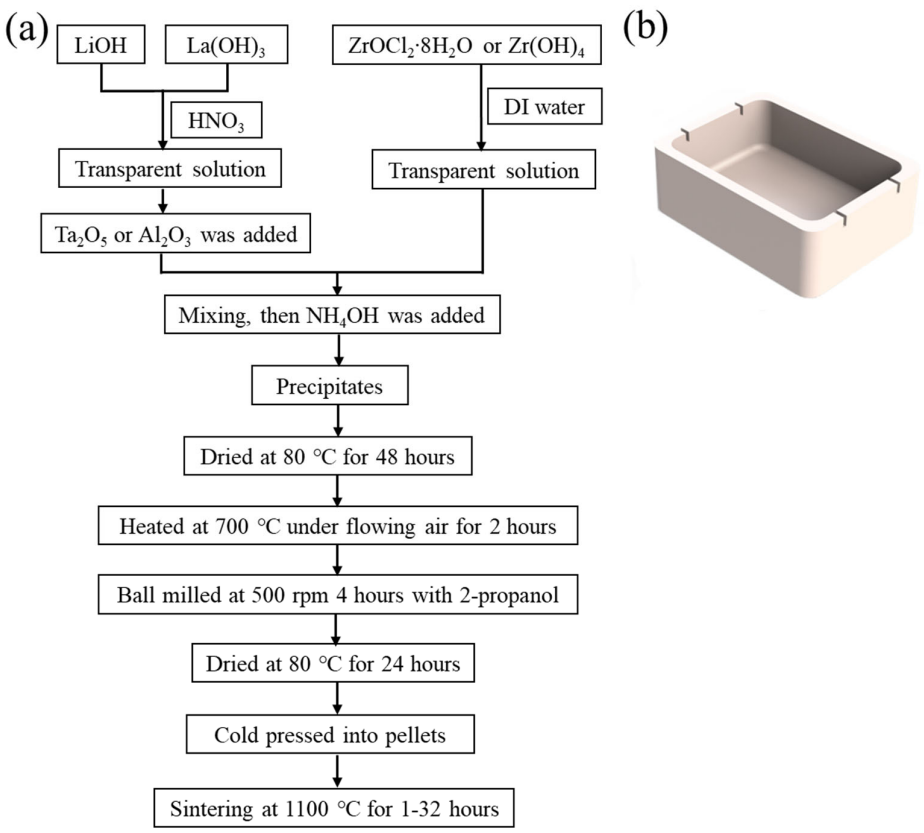

Figure 2.1 (a) Flow chart for the preparation of LLZO by a co-precipitation method. (b) Image of the modified alumina crucible (54mm length × 38mm width × 20 mm height) with four notches (1 mm width × 3 mm depth)

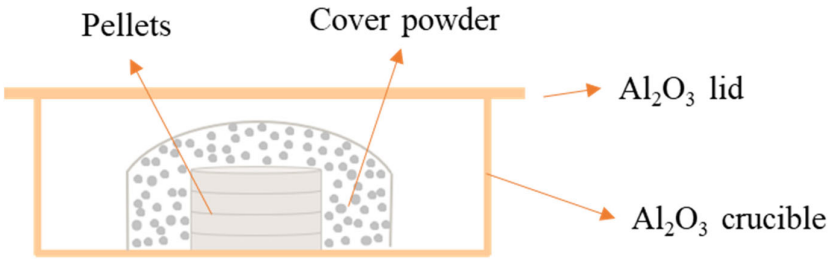

Figure 2.2 The schematic of the pellets with the crucible for sintering

2.2 The synthesis of LLZTO-based composite

To obtain LLZTO (Ta-doped LLZO)-PEO($LiClO_4$) composites, a PEO($LiClO_4$) solution was prepared separately. Appropriate amounts of polyethylene oxide (PEO) (Alfa, M.W. 100,000) and $LiClO_4$ (Alfa, anhydrous, 99%) were dissolved in acetonitrile (Alfa, 99%) and stirred in a magnetic stirrer until a transparent solution was obtained. The molar ratio of ethylene oxide segments to lithium ions was kept at EO/Li=10. LLZTO-PEO($LiClO_4$) composites were obtained by a one-time dip process and a multi-time process. In the one-time dip process, the LLZTO pellets were immersed in sufficient PEO($LiClO_4$) solution for 24 hours, and then dried in vacuum oven at 50°C for 72 hours. In the multi-time dip process, LLZTO pellets were dipped into PEO($LiClO_4$) solution for 30 seconds. Then the pellets were dried in the vacuum oven at 50 ºC for 24 hours. This dipping and drying process was repeated for 6-10 times until there was a thin layer of polymer on the surface of LLZTO pellets.

2.3 Materials characterization

Phase analysis was performed by XRD using a Bruker D8 diffractometer with Cu X-ray source. The working current and voltage were 40 mA and 40 kV. XRD measurements were done with a scan speed of 4 degrees per minute. Morphology and elementary mapping were obtained by using a JEOL JSM-7000F scanning electron microscope (SEM) equipped with an energy dispersive spectrometer (EDS) and a backscattered electron (BSE) detector. LLZO pellets were broken for the cross-section area. A gold coating was performed on the cross-section area with the facility of Sputter

Coater SC-6 to prevent surface charging.

The relative density was tested according to ASTM C20-00 by the Archimedes method in ethanol. Firstly, the dry weight, *D*, was determined in 4 decimals in grams. Then the sample was put in ethanol and boil for 2 hours. During boiling, the specimens should be totally immersed in ethanol and no contact with the container's bottom. After boiling, the suspended weight, *S*, was determined by suspending the sample in ethanol in 4 decimals in grams. Finally, the saturation weight, *W*, was determined after remove the ethanol on the surface. The relative density value was determined by dividing the bulk density by the theoretical density of tetragonal LLZO (~5.108 g/cm^3) [21]. The equations are listed below.

$$\text{Exterior volume, cm}^3\text{, } V = W - S$$

$$\text{Bulk density, g/cm}^3\text{, } B = D / V$$

$$\text{Relative density} = B / 5.108$$

The chemical analysis of the Li, Al and Zr content was carried out by inductively coupled plasma-optical emission spectrometry (ICP-OES) (Perkin Elmer Model Optima 4300DV). The chemical analysis of La content was carried out by inductively coupled plasma-mass spectrometry (ICP-MS) (Perkin Elmer Model ELAN 6000). Pellets were ground into powders by mortar and pestle. 0.2 g powders were put into in 20 mL 12 wt.% HNO_3 and stirred for 7 days to obtain a transparent and homogeneous

solution. Then 1 mL of this solution was dilute in a 50 mL volumetric flask with 12 wt.% HNO_3 to obtain the final solution for ICP test.

Thermal properties of co-precipitates were measured by Thermogravimetric Analysis (TGA) using a TA Instruments TGA Q500 thermogravimetric analyzer. The appropriate amount of the dried precipitates was placed in the testing device and the temperature ramped from room temperature to 900°C with a ramp rate of 10°C per minute in an air environment.

Conductivity was analyzed by AC impedance spectroscopy using a frequency response analyzer (Solartron 1260, USA) in the frequency range 0.5 Hz-15 MHz with amplitude of 50 mV. The temperature was ramped from 20°C to 160°C in increments of 10-20°C and 30 minutes was allowed for temperature equilibration after each temperature change. Silver paste was painted by a wood rod in air on both sides of the pellets and they were cured at room temperature for 2 hours to remove the organic binders. The impedance spectra were fit to equivalent circuit models using ZView software.

Neutron diffraction experiment was performed at the POWGEN instrument, at the Spallation Neutron Source (SNS). Approximately 1 g powder was loaded into a 6 mm vanadium sample can, which was loaded into the POWGEN autochanger (PAC) can. Each dataset was gathered for 7.5 C accumulated proton charge, followed by standard data reduction routine. Data was gathered at room temperature (300K), with additional scan at 100 K was carried out for the sample of $Li_{6.75}La_3Zr_{1.75}Ta_{0.25}O_{12}$ (with 65 wt.%

Li, it is referred to 65Li in Chapter 5). The center wavelength of 1.5 Å was selected, covering incident beam wavelength 1.0-2.0 Å and corresponding to a d spacing range of 0.5-11.0 Å. Rietveld refinements were conducted using TOPAS 6 Academic [110] with the initial structure from *Ia*-3*d* [111].

The grain composition of $Li_{6.75}La_3Zr_{1.75}Ta_{0.25}O_{12}$ was analyzed by atom probe tomography. The atom probe specimen was prepared using a FEI Quanta 200 3D dual beam electron focus ion beam (FIB) microscope equipped with an Omniprobe micro-manipulation system. APT was performed at 40K, 100 kHz, and 100-200 pJ pulse energy with a target evaporation of 1 per pulse. The atom probe data was analyzed using the IVAS 3.6 software package.

Laser ablation inductively coupled plasma mass spectrometry (LA-ICP-MS) line scanning was performed on one $Li_{6.75}La_3Zr_{1.75}Ta_{0.25}O_{12}$ sample for the determination of the element of Si. All LA-ICP-MS tests were carried out using an Element Scientific instrument resolution 193 nm excimer laser coupled to ICP-MS (Agilent 7900). The pellet was ground to obtain a shiny surface and mounted on a computer-controlled xy-stage of an Olympus BX51 microscope. The line scan has a length of 425 μm. The scan speed is 5μm/sec. NIST SRM 610 and 612 glasses were used as the primary standard.

Chapter 3. The stabilization of cubic garnet-type phase

As described in chapter 1, the cubic garnet-type phase is desired as its conductivity is two orders of magnitude higher than that of the tetragonal phase. In this chapter, results on the stabilization of cubic garnet-type phase are presented.

3.1 The effect of co-precipitates processing on the phase stabilization

To understand the decomposition process so that unwanted chemicals could be removed from the co-precipitates, thermal gravimetric analysis (TGA) was used as described in Chapter 2. The TGA curve of 0.24 mol% Al-doped LLZO ($Li_{6.28}Al_{0.24}La_3Zr_2O_{12}$) precipitates in Figure 3.1 shows that there is little mass change after 670°C. Therefore, 700°C seems to be the promising sintering temperature to remove unwanted chemicals from co-precipitates.

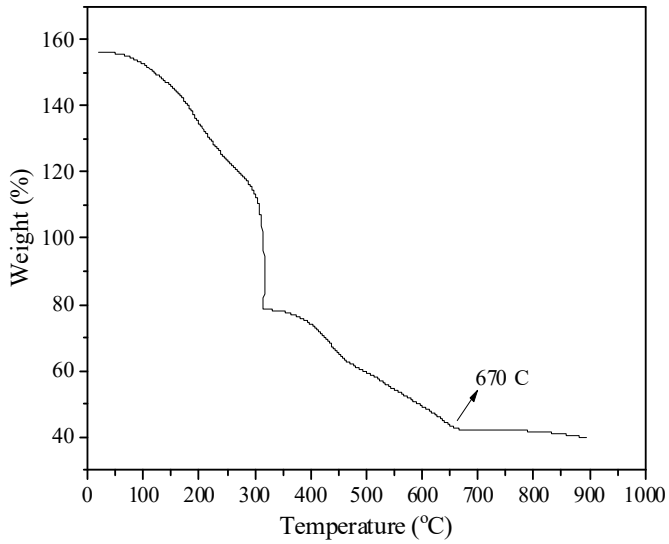

Figure 3.1 TGA curve of $Li_{6.28}Al_{0.24}La_3Zr_2O_{12}$ co-precipitates

To determine the sintering temperature of the co-precipitates, pellets of Al-doped LLZO ($Li_{6.28}Al_{0.24}La_3Zr_2O_{12}$) and Ta-doped LLZO ($Li_{6.75}La_3Zr_{1.75}Ta_{0.25}O_{12}$) were sintered at the same final sintering temperature but using different pre-sintering temperature of 500°C and 700°C.

The XRD results for Al-doped LLZO are shown in Figure 3.2. At the pre-sintering temperature of 700°C, impurities of $LaAlO_3$ (indicated by *) and ZrO_2 (indicated by +) were found. Pure cubic garnet-type structure was obtained at the pre-sintering temperature of 500°C. This indicates that the loss of Li at the sintering of 700°C is larger than the excess Li added for the Li compensation. Therefore, 500°C was chosen as the pre-sintering temperature for the co-precipitates of Al-doped LLZO.

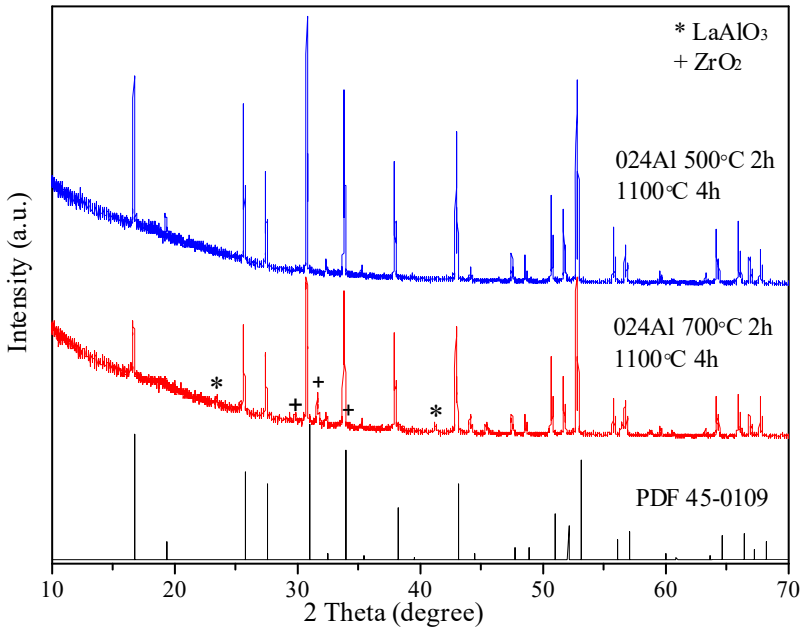

Figure 3.2 XRD patterns of $Li_{6.28}Al_{0.24}La_3Zr_2O_{12}$ sintered at different pre-sintering temperature, * $LaAlO_3$, + ZrO_2

The XRD results for Ta-doped LLZO are shown in Figure 3.3. Impurities were found at both pre-sintering temperature. At 500°C, impurities of $La_2Zr_2O_7$ (indicated by *) and ZrO_2 (indicated by +) were found. While at 700°C, only $La_2Zr_2O_7$ was found. Therefore, 700°C is chosen as the pre-sintering temperature for Ta-doped LLZO.

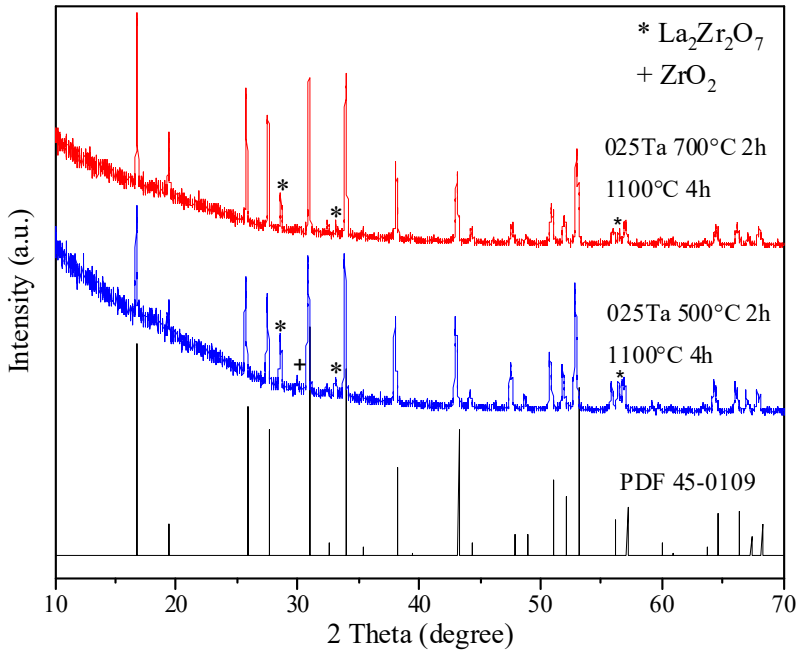

Figure 3. 3 XRD patterns of $Li_{6.75}La_3Zr_{1.75}Ta_{0.25}O_{12}$ samples sintered at different pre-sintering temperature, * $La_2Zr_2O_7$, + ZrO_2

3. 2 The effect of no doping elements on the phase stabilization

An experiment was conducted first to evaluate the effect of doping elements on the formation of cubic garnet-type LLZO. The XRD result of LLZO pellet without doping elements is shown in Figure 3.4. The tetragonal phase can be identified by peak doublets [21,47,112]. Without doping elements, the tetragonal phase was obtained.

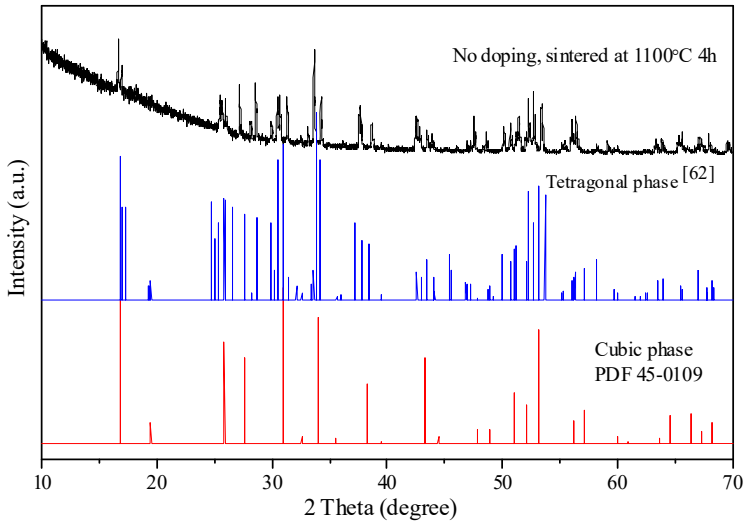

Figure 3.4 XRD pattern of LLZO pellets without doping elements sintered at 1100°C [112]

3.3 The phase stabilization of cubic garnet-type phase by Al doping

3.3.1 The effect of sintering temperature

The XRD patterns of $Li_{6.28}Al_{0.24}La_3Zr_2O_{12}$ pellets sintered at same sintering time of 4 hours but different sintering temperature of 1000°C, 1050°C and 1100°C are shown in Figure 3.5. At 1000°C, besides the cubic phase, peaks for $La_2Zr_2O_7$ (indicated by *) were observed. The $La_2Zr_2O_7$ pyrochlore phase was not presented at 1050°C, but ZrO_2 (indicated by +) was observed. At the sintering temperature of 1100°C, the pure cubic garnet-type phase was obtained. Therefore, 1100°C for 4 hours was chosen as sintering parameters for Al-doped LLZO.

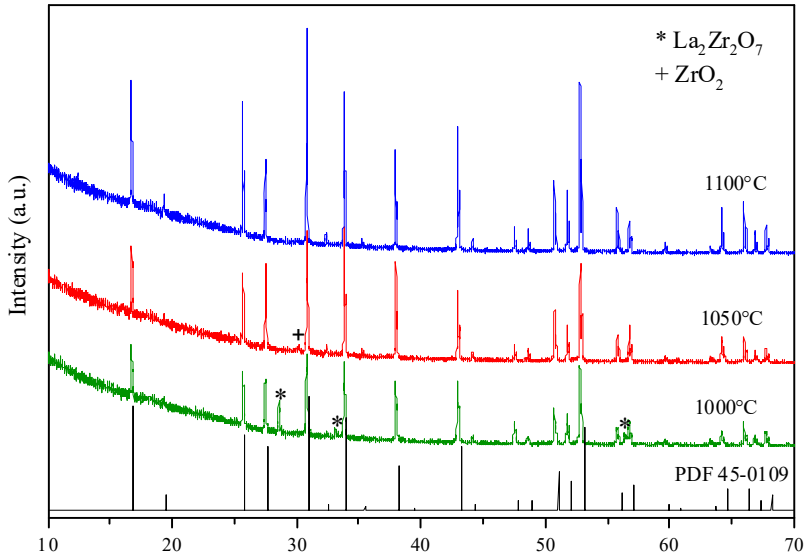

Figure 3.5 XRD patterns of $Li_{6.28}La_3Zr_2Al_{0.24}O_{12}$ pellets sintered at different temperature, * $La_2Zr_2O_7$, + ZrO_2

3.3.2 The structure through the whole pellet

Loss of lithium from the pellet during sintering could result in differences between the lithium content at the surface and that in the interior of the pellet. To check if the structure is uniform through the whole pellet, one pellet of $Li_{6.28}La_3Zr_2Al_{0.24}O_{12}$ was ground to different thicknesses and XRD was performed for each thickness. This sample has a thickness of 1.08 mm. The depth of one surface was set as 0 mm (t=0 mm). And the depth of the other surface was referred to the other side. The XRD patterns are shown in Figure 3.6. From the XRD results, it is found that the structure was the same at different depths. The phase ZrO_2 was present because the co-precipitates were sintered at 700°C. The cubic phase and ZrO_2 phase were all found at different depths.

The ratios of the peak intensity of ZrO_2 2θ=32° (labeled by +) to the peak intensity of LLZO at 2θ=31° (the peak on the left of the labeled ZrO_2 peak) for different depths are listed in Table 3.1. There are no significant differences between all the ratios, which are in the range of 0.13 to 0.21. The ZrO_2 phase is uniformly distributed in the sample. Therefore, the structure through the whole $Li_{6.28}Al_{0.24}La_3Zr_2O_{12}$ pellet is the same.

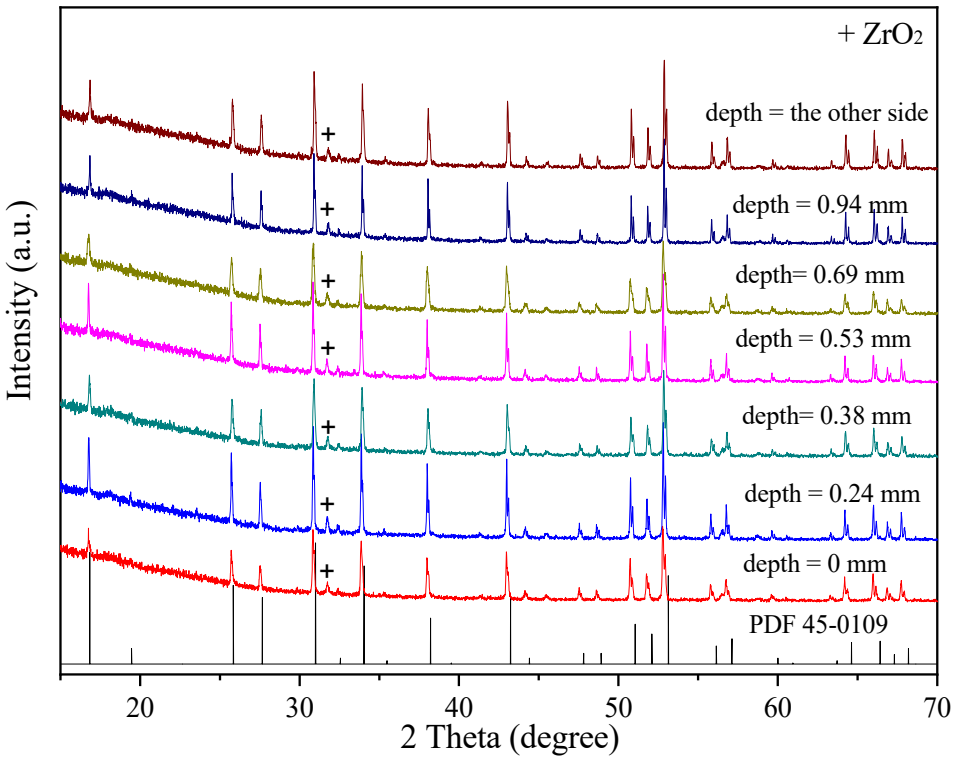

Figure 3.6 XRD patterns of one $Li_{6.28}Al_{0.24}La_3Zr_2O_{12}$ pellet at different depths, sintered at 700°C for 2 hours and 1100°C for 4 hours, + ZrO_2

Table 3.1 The ratio of the peak intensity of ZrO_2 at 2θ=32° (labeled by +) to the peak intensity of LLZO at 2θ=31° (the peak on the left of the labeled ZrO2 peak) for one $Li_{6.28}Al_{0.24}La_3Zr_2O_{12}$ pellet at different depths, which was sintered at 700°C for 2 hours and 1100°C for 4 hours

Depth (mm)	The ratio = ZrO_2 peak intensity (2θ=32°) / LLZO peak intensity (2θ=31°)
0	0.19
0.24	0.14
0.38	0.17
0.53	0.15
0.69	0.21
0.94	0.15
The other side	0.13

From the XRD results, the lattice parameters were calculated and listed in Table 3.2 and plotted in Figure 3.7. The lattice parameter ranged from 12.967 Å to 12.975 Å. The difference between the lattice parameter and the average value (12.971 Å) is only 0.004 Å. Therefore, the lattice parameter slightly varies at different thickness of the pellet. At the middle of the pellet, the lattice parameter is a little smaller than other places.

Table 3.2 Lattice parameters of one $Li_{6.28}Al_{0.24}La_3Zr_2O_{12}$ pellet at different depths

Depth (mm)	0	0.24	0.38	0.53	0.69	0.94	1.08
Lattice parameter (Å)	12.975	12.971	12.972	12.967	12.969	12.973	12.972

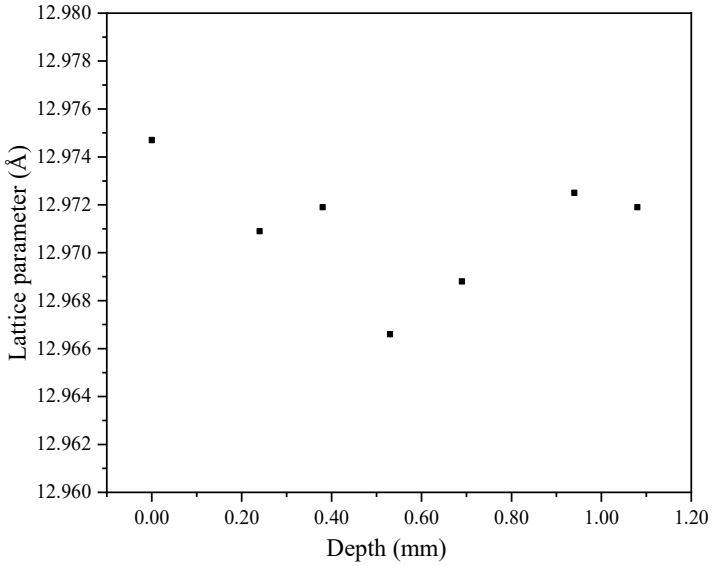

Figure 3.7 Lattice parameters of one $Li_{6.28}Al_{0.24}La_3Zr_2O_{12}$ pellet at different depths

3.3.3 The effect of Al doping level on the structure

XRD patterns of Al-doped LLZO samples with different Al molar concentrations were sintered at 1100°C for 4 hours are shown in Figure 3.8. When there is 0.1 mol.% Al, two additional phases were present, $La_2Zr_2O_7$ (indicated by *) and La_2O_3 (indicated

by #). When the Al molar concentration is above 0.2, but smaller than 0.3, only the pure cubic phase was observed. When the Al molar concentration reached 0.3 mol.%, $La_2Zr_2O_7$ phase presented again. At an Al molar concentration of 0.67 mol%, cubic phase and $LaAlO_3$ phase (indicated by +) were obtained. The presence of $LaAlO_3$ indicates that the solubility limit of aluminum in the cubic LLZO structure had been exceeded. Therefore, to obtain pure cubic phase, a molar concentration between 0.2 mol.% and 0.3 mol.% is required.

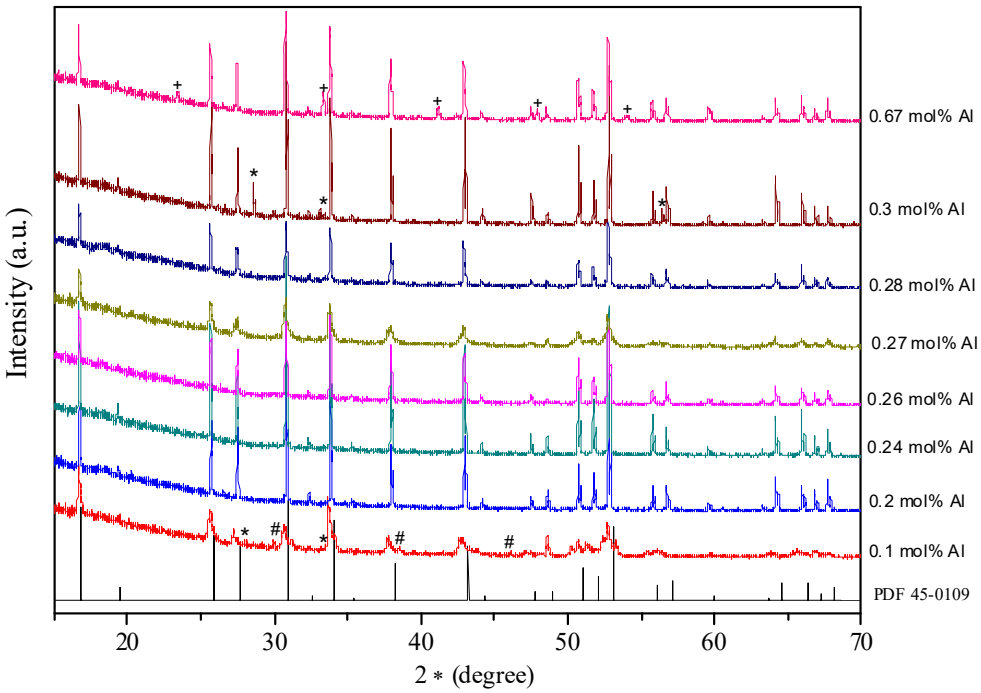

Figure 3.8 XRD pattern of Al-doped LLZO pellets with different Al molar concentration, * $La_2Zr_2O_7$, # La_2O_3, + $LaAlO_3$

The lattice parameters of cubic phase Al-doped LLZO structure determined from XRD results in Figure 3.7 are summarized in Table 3.3 and plotted in Figure 3.9. With 0.1 mol.% Al, the lattice parameter was not calculated because of the broad XRD peaks in Figure 3.8. When Al molar concentration is in the range of 0.2-0.67 mol%, the lattice parameters are independent of Al content, and they are around 12.960 Å, which is in good agreement with reported results of 12.95-12.97 Å [25,49].

Table 3.3 Lattice parameters of LLZO with different Al molar concentration

Aluminum content (mol%)	0.20	0.24	0.26	0.27	0.28	0.30	0.67
Lattice parameter (Å)	12.960	12.951	12.971	12.965	12.971	12.953	12.953
Average Lattice parameter (Å)	12.961						

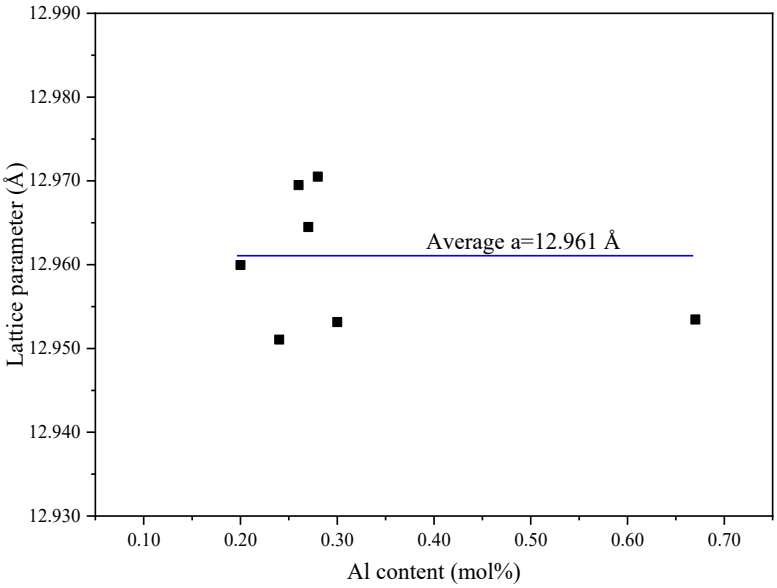

Figure 3.9 Lattice parameters of Al-doped LLZO with different Al molar concentration

3.4 The phase stabilization of cubic garnet-type phase by Ta doping

3.4.1 The effect of sintering parameters

XRD patterns for $Li_{6.75}La_3Zr_{1.75}Ta_{0.25}O_{12}$ samples sintered at same sintering time of 4 hours but different temperature of 1100°C, 1150°C, and 1200°C are shown in Figure 3.10. The patterns are not pure cubic phase. Two additional phases, $La_2Zr_2O_7$ (indicated by *) and ZrO_2 (indicated by +), were present in all these XRD patterns.

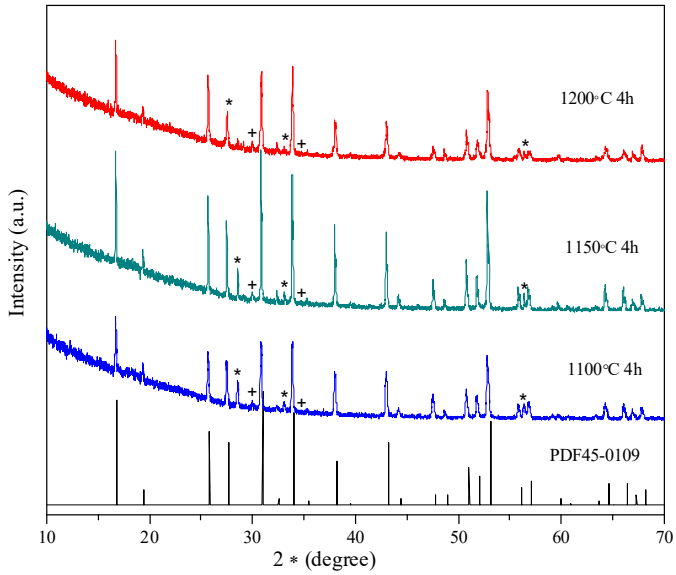

Figure 3.10 XRD patterns of $Li_{6.75}La_3Zr_{1.75}Ta_{0.25}O_{12}$ samples sintered at different temperature, * $La_2Zr_2O_7$, + ZrO_2

To remove the impurities, the sintering time was increased to 8 hours at 1100°C and 12 hours at 1150°C. All XRD patterns, shown in Figure 3.11, are not the pure cubic phase. The same impurities, $La_2Zr_2O_7$ (indicated by *) and ZrO_2 (indicated by +), were still present in all these samples.

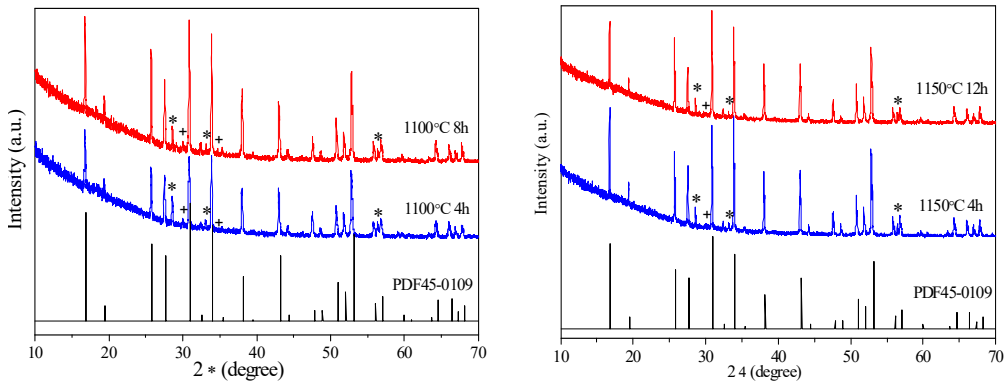

Figure 3.11 XRD patterns of $Li_{6.75}La_3Zr_{1.75}Ta_{0.25}O_{12}$ samples sintered at different sintering time, * $La_2Zr_2O_7$, + ZrO_2

3.4.2 The effect of Li excess amount

The presence of $La_2Zr_2O_7$ is likely due to an insufficient amount of Li, as Li is volatilized during the high temperature sintering. When the amount excess of LiOH was increased from 15 wt.% to 30 wt.%, the $La_2Zr_2O_7$ phase and ZrO_2 phase were removed and the pure cubic phase was obtained. The XRD patterns are shown in Figure 3.12. Therefore, 30 wt.% excess Li instead of 15 wt.% (which is used in Al-doped LLZO) is needed to obtain the pure cubic garnet-type phase for Ta-doped LLZO pellets sintered at 1100°C for 16 hours.

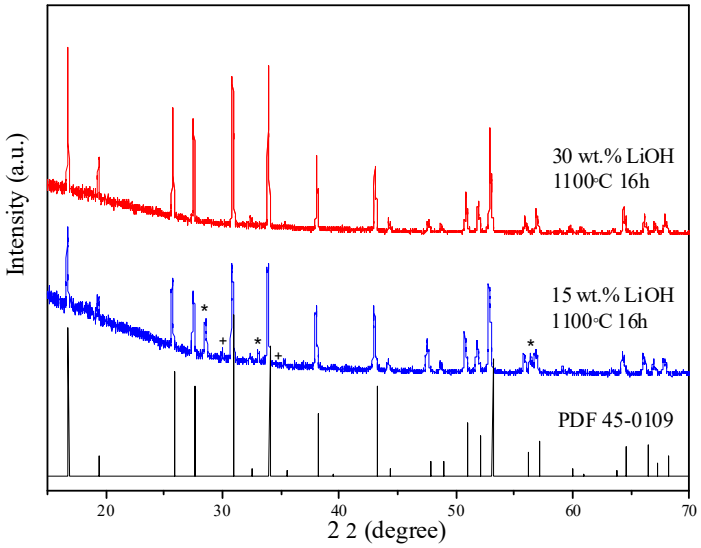

Figure 3.12 XRD patterns of $Li_{6.75}La_3Zr_{1.75}Ta_{0.25}O_{12}$ pellets, * $La_2Zr_2O_7$, + ZrO_2

The lattice parameters of cubic phase $Li_{6.75}La_3Zr_{1.75}Ta_{0.25}O_{12}$ determined from above XRD results are summarized in Table 3.4. The lattice parameter is a little smaller for pellet sintering with 30 wt.% excess LiOH. But the difference between all these samples is small. Therefore, the lattice parameter of $Li_{6.75}La_3Zr_{1.75}Ta_{0.25}O_{12}$ is independent of sintering parameters, and is around 12.95 Å, which is similar with the lattice parameter of $Li_{6.28}Al_{0.24}La_3Zr_2O_{12}$ of 12.951 Å. These two compositions of Al-doped and Ta-doped LLZO will be used in the following chapter.

Table 3.4 Lattice parameters of $Li_{6.75}La_3Zr_{1.75}Ta_{0.25}O_{12}$ pellets at different sintering parameters

Sintering parameters	1100°C		1150°C		1200°C 4h	1100°C 16hrs 30 wt.% excess LiOH
	4 h	8 h	4 h	12 h		
Lattice parameter (Å) (mean ± SD)	12.952 ±0.007	12.959 ±0.002	12.959 ±0.001	12.961 ±0.002	12.940 ±0.003	12.936±0.003
Average lattice parameter (Å)	12.951					

3.5 Conclusion

The cubic phase structure has been stabilized by doing elements of Al and Ta. For Al-doped LLZO, to obtain the pure cubic phase structure, an Al molar concentration in the range of 0.2-0.3 mol.%. Two additional phases of $La_2Zr_2O_7$ and La_2O_3 were observed when the Al concentration is 0.1 mol.%, while $LaAlO_3$ phase was obtained when the Al concentration is 0.67 mol%. For Ta-doped LLZO pellets sintered at 1100°C for 16 hours, 30 wt.% excess Li instead of 15 wt.% (which is used in Al-doped LLZO) is needed to obtain the pure cubic garnet-type phase. The larger Li loss in Ta-doped LLZO is mainly due to the higher precipitation processing temperature (700°C vs 500°C).

Chapter 4. The effect of cation substitution on the morphology, composition and Li-ion conductivity of LLZO

In this chapter, the composition of $Li_{6.28}Al_{0.24}La_3Zr_2O_{12}$ (15 wt.% Li excess) and $Li_{6.75}La_3Zr_{1.75}Ta_{0.25}O_{12}$ (65 wt.% Li excess) will be used. The sintering parameters to obtain the pure cubic garnet-type phase are 1100°C for 4 hours for $Li_{6.28}Al_{0.24}La_3Zr_2O_{12}$ and 1100°C for 16 hours for $Li_{6.75}La_3Zr_{1.75}Ta_{0.25}O_{12}$. The morphology, composition and Li-ion conductivity results are presented in this chapter.

4.1 Morphology

4.1.1 Al-doped LLZO

SEM images of the fracture cross section area of $Li_{6.28}Al_{0.24}La_3Zr_2O_{12}$ pellet are shown in Figure 4.1. Large connected pores were found, which indicates a low relative density. Measurement of the relative density was not possible because powders came off the pellets during the boiling step. From Figure 4.1(b), the fracture surface were smooth and necks between grains were found. By comparing Figure 4.1 (c) and (d), which were taken from different locations at the middle of the cross-section area but with the same magnification, it is found that the grain size is not uniform through the cross section. Some particles are over 25 μm × 15 μm, but some are less than 10 μm × 10 μm.

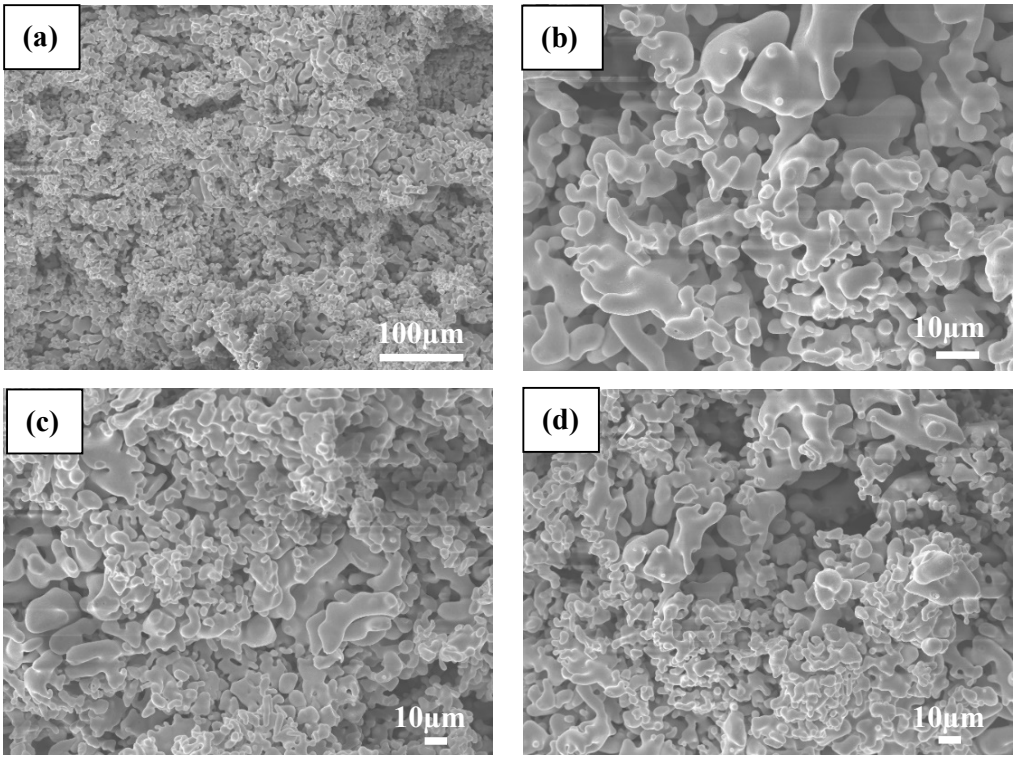

Figure 4.1 SEM images of fracture cross sections of $Li_{6.28}Al_{0.24}La_3Zr_2O_{12}$ pellet

4.1.2 Ta-doped LLZO

SEM images of the fracture cross section area of $Li_{6.75}La_3Zr_{1.75}Ta_{0.25}O_{12}$ pellet are shown in Figure 4.2. Ta-doped LLZO SEM images at different magnifications also showed that the pellet is porous. The relative density was measured to be around 60% by Archimedes method using alcohol as the immersion medium. Figure 4.2(b) shows that necks were found between adjacent particles, and the pores are too big to be filled, which is similar to Al-doped LLZO. It is also found that the grain size is not uniform through the cross section from Figure 4.2(c)(d). By comparing Figure 4.2(c)(d) with

Figure 4.1(c)(d) of Al-doped LLZO, it is found that the difference between gains in Ta-doped LLZO is smaller than that in Al-doped LLZO. Grains are around 15 μm × 10 μm or smaller than 10 μm × 10 μm, while Al-doped LLZO has some particles of a size over 25 μm × 15 μm and some of less than 10 μm × 10 μm. In addition, transgranular facture surface was observed, while a smooth fracture surface was found in Al-doped LLZO, which indicates that grains in Ta-doped LLZO were better connected.

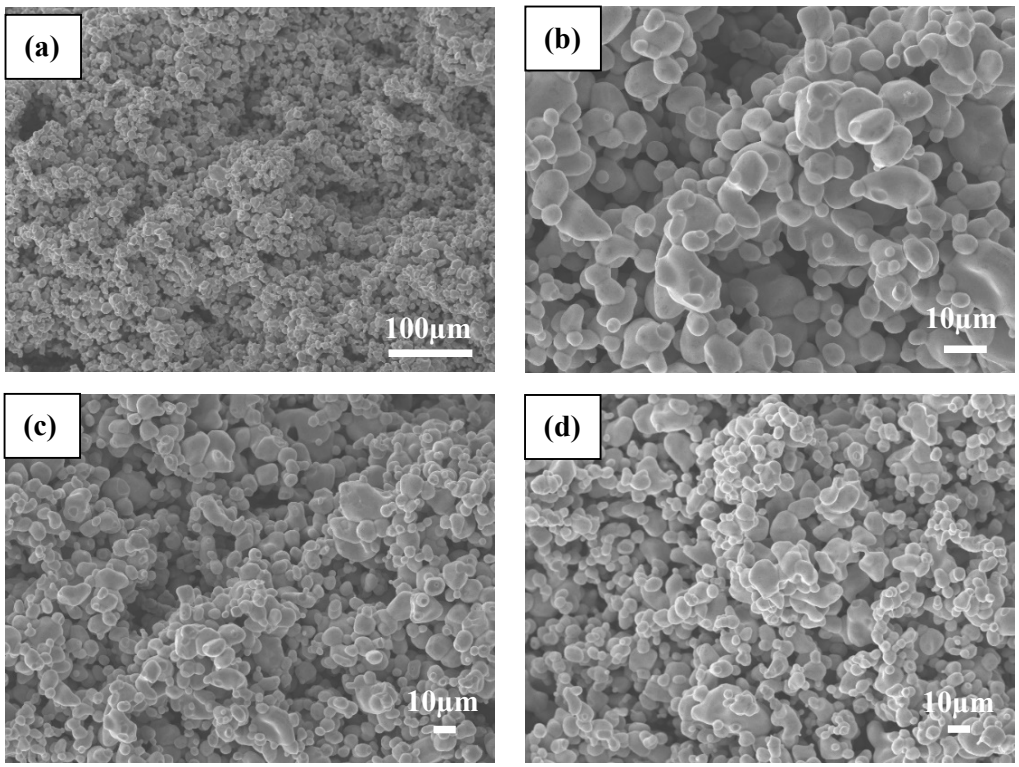

Figure 4.2 SEM images of fracture cross sections of $Li_{6.75}La_3Zr_{1.75}Ta_{0.25}O_{12}$ pellet

4.2 Composition

4.2.1 Al-doped LLZO

The atomic ratios of Al:La:Zr for $Li_{6.28}Al_{0.24}La_3Zr_2O_{12}$ pellet determined by EDS are 0.14:3:1.6. The Li content could not be detected by EDS, so ICP-OES was used to determine the compositions, which are listed in Table 4.1. Aluminum was detected in all samples, including one undoped LLZO sample. The Al in the undoped LLZO was presumably from Al_2O_3 crucible. The addition Al source of Al_2O_3 crucible also resulted in higher Al compositions in samples than that of the nominal composition. Besides, as three sample with the same nominal composition of $Li_{6.4}Al_{0.20}La_3Zr_2O_{12}$ have different compositions in the ICP results, there is composition variations between samples. The Li concentrations in all Al-doped LLZO samples are similar to or a little higher than the nominal composition. The undoped LLZO has a lower Li concentration than the nominal composition. This indicates that Al doping may reduce the evaporation of Li. A similar ratio of La/Zr was obtained by both EDS and ICP method. Therefore, this synthesis of Al-doped LLZO could prepare cubic phase garnet-type LLZO with the desired composition.

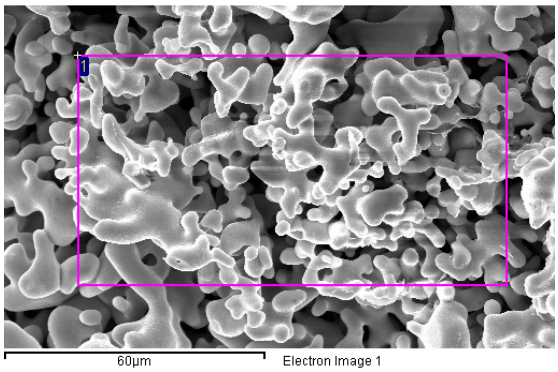

Spectrum	O	Al	Zr	La
1	67	1	11	21
Atomic ratio		0.14	1.6	3

All results are in atomic%

Figure 4.3 EDS results of fracture cross section of $Li_{6.28}Al_{0.24}La_3Zr_2O_{12}$ pellet

Table 4. 1 Composition from ICP analysis of LLZO, Al-doped LLZO with different Al molar concentration, sintered at 1100°C for 4 hours, the ratio is normalized with respect to the La content

Nominal composition		ICP results			
		Li	Al	La	Zr
$Li_7La_3Zr_2O_{12}$		6.42	0.04	3	1.82
$Li_{6.4}Al_{0.20}La_3Zr_2O_{12}$		6.41	0.24	3	1.92
$Li_{6.28}Al_{0.24}La_3Zr_2O_{12}$	Sample 1	6.28	0.24	3	1.90
	Sample 2	6.92	0.32	3	2.05
	Sample 3	6.49	0.31	3	1.94
$Li_{6.22}Al_{0.26}La_3Zr_2O_{12}$		6.35	0.28	3	1.96

4.2.2 Ta-doped LLZO

The atomic ratios of La:Zr:Ta for $Li_{6.75}La_3Zr_{1.75}Ta_{0.25}O_{12}$ measured by EDS are 3:1.4:0.28, which are shown in Figure 4.4. The atomic ratios of Li:Al:La:Zr determined by ICP are 6.73:0.07:3:1.66, which is normalized with respect to the La content. The ICP results indicate that Al was present, presumably came to the pellets from the Al_2O_3 crucible. The composition results also indicate that the Al concentration is too small to be measured in EDS, as Al detected from ICP is 0.2 wt.% while a minimum requirement for EDS is 1 wt.% [113]. The atomic ratio of La/Zr is similar in EDS and ICP.

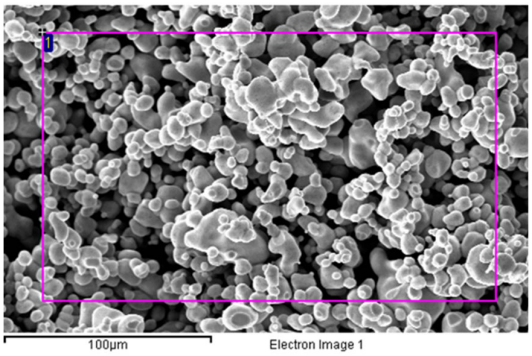

Spectrum	O	Zr	La	Ta
1	67	10	21	2
Atomic ratio		1.4	3	0.28

All results are in atomic%

Figure 4.4 EDS result of fracture cross section of $Li_{6.75}La_3Zr_{1.75}Ta_{0.25}O_{12}$ pellet

4.3 Li-ion conductivity

4.3.1 Al-doped LLZO

The impedance spectra of $Li_{6.28}Al_{0.24}La_3Zr_2O_{12}$ pellet measured at different temperatures of 20-160°C are shown in Figure 4.5. The experimental data was fitted

with an equivalent circuit consisting of $(R_tCPE_t)(CPE_e)$ for temperature 20-80°C and $(R_tCPE_t)(R_sCPE_s)(CPE_e)$ for 100-160°C [33,58,114,115], where R and CPE were the resistance and the constant phase element, and the subscript t, s and e referred to the total, surface layer and electrode contribution, respectively. The first semicircle at high frequency is attributed to the total resistance (bulk + grain boundary). The grain and grain boundary contributions cannot be separated, which is consistent with other works [43,55]. The intermediate frequency semicircle measured at 100-160°C is assigned to surface (interfacial) effect. The corresponding capacitance was calculated to be around 1.5×10^{-8} F, which is consistent with a surface layer contribution [49][58]. The tail at low frequencies indicates the conductivity of the material is ionic nature. The room temperature total Li-ion conductivity of $Li_{6.28}Al_{0.24}La_3Zr_2O_{12}$ sample is 1.9×10^{-6} S/cm. This conductivity is two orders of magnitude lower than reported conductivity of 4×10^{-4} S/cm [47], which is due to the high porosity of the pellet.

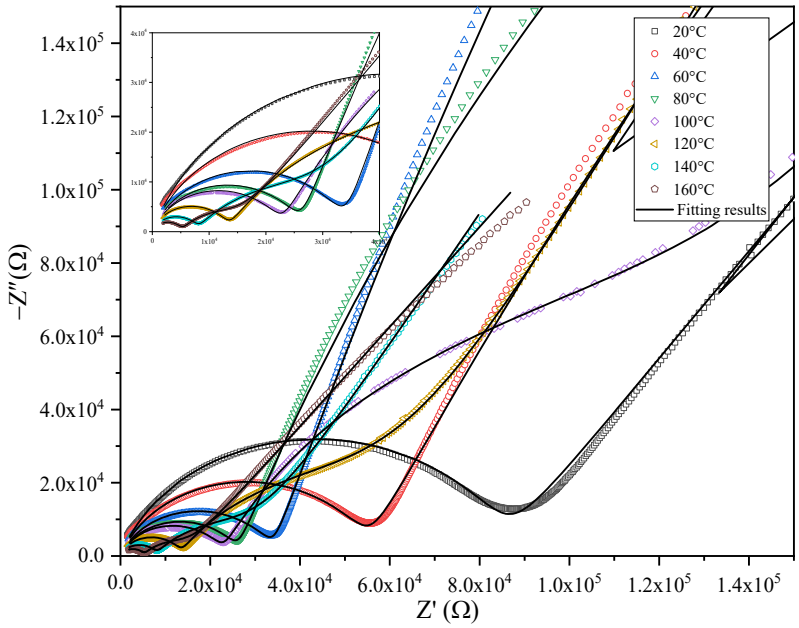

Figure 4.5 Impedance spectra of $Li_{6.28}Al_{0.24}La_3Zr_2O_{12}$ pellets measured at different temperatures. Data were fitted using the equivalent circuit of $(R_tCPE_t)(CPE_e)$ for 20-80°C, $(R_tCPE_t)(R_sCPE_s)CPE_e$ for 100-160°C

Based on the total conductivities calculated from Figure 4.5, Arrhenius plot is plotted in Figure 4.6. The activation energy determined from the slope of the log (σT) versus 1000/T plot is 0.19 eV at low temperature (20-100°C) and 0.39 eV at high temperature (100-160°C). As there are two slopes in Arrhenius plot, two mechanisms of lithium-ion diffusion may exist in the test temperature range of 20-160°C. Recalling the impedance spectra in Figure 4.5, only one semicircle was presented at low temperature of 20-80°C, while two semicircles were presented at the temperature of 100-160°C with one additional semicircle attributed to the surface layer. It is widely reported that the reaction of LLZO materials with humidity and CO_2 leads to the

formation of LiOH and $LiCO_3$, which result in the effect of the surface layer in the impedance test [49,88,116–120]. However, the surface layer effect at high temperature is complex and has not been fully understood. In this work, this surface layer effect was assumed to be related to the formation of LiOH and $LiCO_3$, which became significant when the temperature was 100°C or above and resulted in two different activation energies.

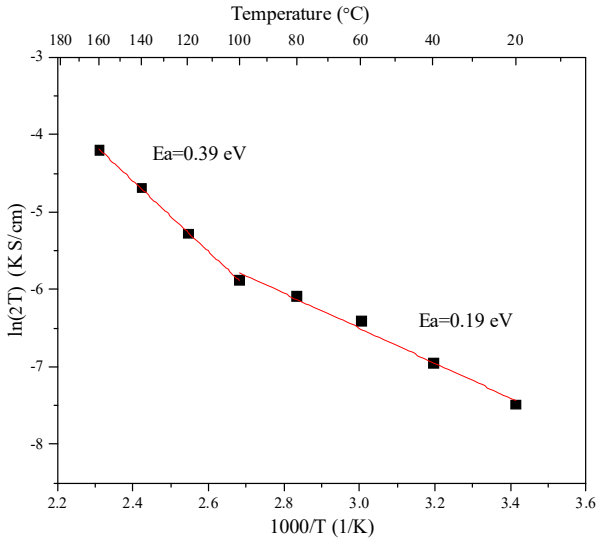

Figure 4.6 Arrhenius plot of total conductivities for $Li_{6.28}Al_{0.24}La_3Zr_2O_{12}$ sample

4.3.2 Ta-doped LLZO

The impedance spectra of $Li_{6.75}La_3Zr_{1.75}Ta_{0.25}O_{12}$ pellet measured at different temperatures of 20-120°C are shown in Figure 4.7. The experimental data was fitted with an equivalent circuit consisting of $(R_tCPE_t)(CPE_e)$, which is the same equivalent

circuit used for Al-doped LLZO tested at 20-80°C. The room temperature total Li-ion conductivity of $Li_{6.75}La_3Zr_{1.75}Ta_{0.25}O_{12}$ sample is 8.9×10^{-6} S/cm, while the reported total conductivity is as high as 8.7×10^{-4} S/cm [38]. The high porosity is the main reason for this low ionic conductivity, as the reported samples with high Li-ion conductivities are dense (~96-98%) [38].

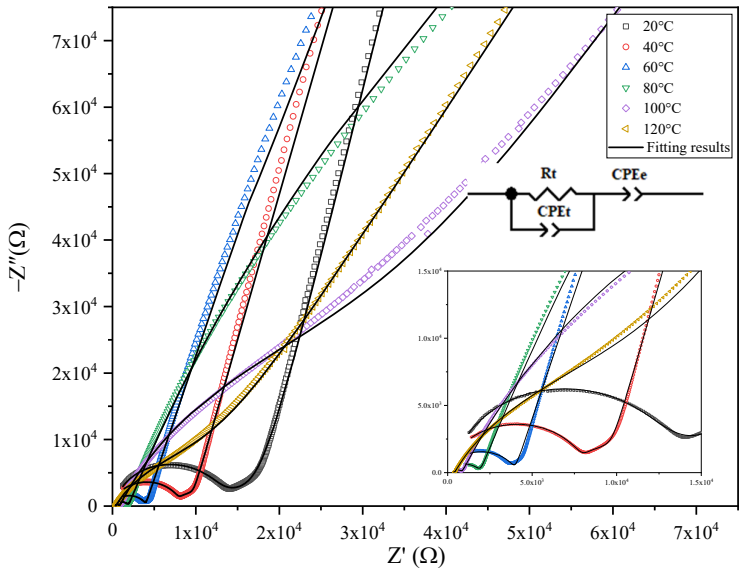

Figure 4.7 Impedance spectra of $Li_{6.75}La_3Zr_{1.75}Ta_{0.25}O_{12}$ pellets measured at different temperatures, data were fitted using the presented equivalent circuit of $(R_tCPE_t)(CPE_e)$

Based on the total conductivities calculated from Figure 4.7, Arrhenius plot is plotted in Figure 4.8. The activation energy determined from the slope of the log (σT) versus 1000/T plot is 0.37 eV. In the temperature range of 20-100°C, Ta-doped LLZO has a higher activation energy than Al-doped LLZO (0.19eV). Only one slope was

observed in the temperature range of 20-120°C, which is different from that of Al-doped LLZO of 20-160°C. If only the same temperature range of 20-100°C is considered, both Al-doped and Ta-doped LLZO has only one slope and the Al-doped LLZO has a lower activation energy (0.19 eV for Al-doped LLZO vs 0.37 eV for Ta-doped LLZO).

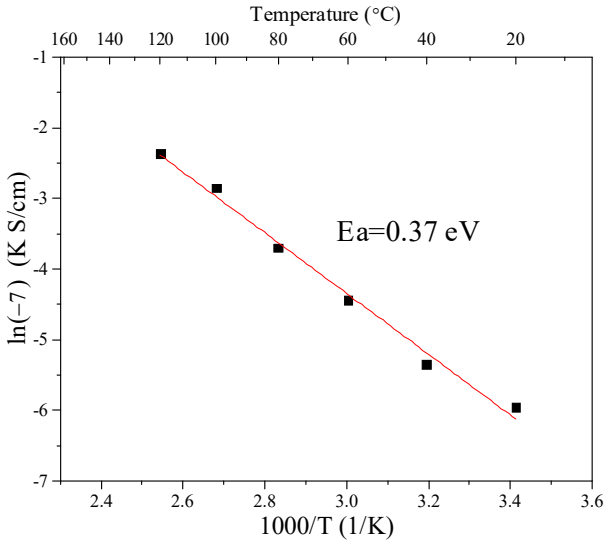

Figure 4.8 Arrhenius plot of total conductivities for $Li_{6.75}La_3Zr_{1.75}Ta_{0.25}O_{12}$ sample

4.3.3 A summary of the RT conductivities of Al-doped and Ta-doped LLZO

The RT conductivities for different Al-doped and Ta-doped LLZO samples are listed in Table 4.2. It is found that Al-doped LLZO has maximum RT total Li-ion conductivity of 4.5×10^{-6} S/cm, and Ta-doped LLZO has a higher maximum RT total Li-ion conductivity of 1.9×10^{-5} S/cm. One possible reason is found to be the better grain

connections in Ta-doped LLZO samples as observed in the SEM images. This was also confirmed by the density measurements as powders came off the Al-doped LLZO during the boiling step for porosity test while the Ta-doped LLZO kept intact during the porosity test.

Table 4.2 RT (20°C) total Li-ion conductivity of $Li_{6.28}Al_{0.24}La_3Zr_2O_{12}$ and $Li_{6.75}La_3Zr_{1.75}Ta_{0.25}O_{12}$ samples

RT total σ_{Li+} (S/cm)	
$Li_{6.28}Al_{0.24}La_3Zr_2O_{12}$	$Li_{6.28}Al_{0.24}La_3Zr_2O_{12}$
4.50×10^{-6}	1.85×10^{-5}
1.92×10^{-6}	1.58×10^{-5}
1.29×10^{-6}	1.54×10^{-5}
4.65×10^{-7}	1.29×10^{-5}
2.23×10^{-7}	8.87×10^{-6}
1.27×10^{-8}	3.86×10^{-6}
1.22×10^{-8}	3.40×10^{-6}
	2.69×10^{-6}
	2.32×10^{-6}
	1.42×10^{-6}
	7.56×10^{-7}

4.4 Conclusion

The Al-doped LLZO has a lower RT total Li-ion conductivity than Ta-doped LLZO, which is due to the worse sintering results of the worse grain connection. Ta-doped LLZO has a maximum RT total Li-ion conductivity of 1.85×10^{-5} S/cm, which is still much lower than the reported value of 1×10^{-3} S/cm [40]. The low relative density of around 60% is the main reason.

Chapter 5. The effect of LiOH cover powders on the structure, morphology, and Li-ion conductivity

The results presented in Chapter 4 show that porous microstructure results in low Li-ion conductivities, so a dense microstructure is needed to obtain a high Li-ion conductivity. In this chapter, Ta-doped cubic garnet-type $Li_{6.75}La_3Zr_{1.75}Ta_{0.25}O_{12}$ (LLZTO) with a relative density of 92% was prepared by a simple co-precipitation method with cold uniaxial pressing and sintering in a lithium-rich air atmosphere, which was created by the addition of LiOH to the LLZTO cover powder.

The cover powders used in this chapter is referred to 15Li, which is the powder with 15 wt.% excess LiOH added at the beginning of the co-precipitation process, after the heat treatment of 700°C and before the ball milling. The cover with the addition of LiOH is referred to 15Li + LiOH, which is a mixture of 15Li and 6 wt.% LiOH. This mixture was jar milled for 12 hours before use in sintering. LLZTO samples in this chapter are named as *x*Li, where *x* refers to the total amount of excess LiOH added at the beginning of the co-precipitation method. 65Li is the same sample used in Chapter 4. Samples in this chapter were sintered with the same sintering parameters of 1100°C for 16 hours, if the sintering parameters are not specified. The effects of LiOH cover powders on the structure, morphology, densification, composition and Li-ion conductivity are presented.

5.1 The effect of LiOH cover powders on LLZTO with different excess Li amount

5.1.1 Structure

The XRD patterns of different LLZTO samples covered with the same cover powder of 15Li are shown in Figure 5.1 (a). For the 25Li sample (25 wt.% excess LiOH), the $La_2Zr_2O_7$ pyrochlore phase was observed in addition to the cubic garnet phase, presumably because of the loss of lithium during sintering. When the excess LiOH was increased to 30 wt.% or larger, a pure cubic garnet phase was obtained. Even at the highest levels of excess LiOH (65 and 75 wt.%), no peaks related to LiOH were observed for any of the samples, indicating that there was no LiOH left or the remaining amount of LiOH was too small to be detected by XRD.

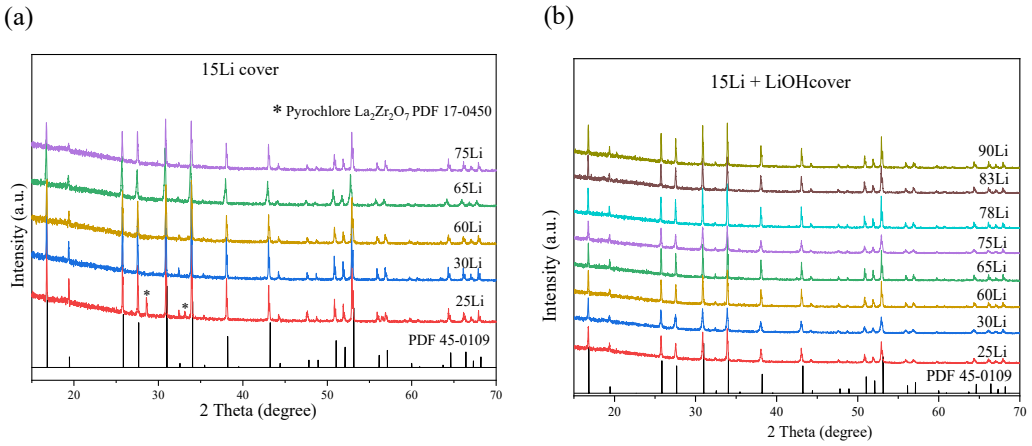

Figure 5.1 XRD patterns of different LLZTO pellets sintered at 1100°C for 16 hours (a) with cover powder of 15Li, (b) with cover powder of 15Li + LiOH

The XRD patterns of LLZTO samples covered with 15Li + LiOH are shown in

Figure 5.1 (b). All spectra contained peaks for only the cubic garnet phase. The LiOH in the cover powder also helped with the phase stabilization, as 25Li contains only the pure cubic garnet phase with the cover of 15Li + LiOH but contained the additional pyrochlore phase with the cover of 15Li.

The lattice parameters calculated from Figure 5.1 are listed in Table 5.1. With the cover of 15Li, the lattice parameter ranged from 12.931 Å to12.939 Å. While the lattice parameter ranged from 12.935 Å to12.942 Å with the cover of 15Li + LiOH, which similar to that of 15Li cover. For samples sintered with the cover of 15Li + LiOH, when excess Li amount increased from 25 to 90 wt.%, the lattice parameters were similar, and they were all around 12.94 Å.

Table 5.1 Lattice parameter of different Li with 15Li and 15Li + LiOH cover, 4-6 samples for each composition

Excess Li amount	Lattice parameter (Å) (mean ± SD)	
	15Li cover	15Li + LiOH cover
25	12.935±0.001	12.939±0.002
30	12.939±0.001	12.938±0.002
60	-	12.939±0.004
65	12.937±0.003	12.942±0.011
75	12.931±0.006	12.935±0.002
78	-	12.937±0.004
83	-	12.935±0.001
90	-	12.937±0.003

5.1.2 Relative density, morphology and composition

The densification results of different LLZTO samples are summarized in Table 5.2. Shrinkage did not occur with the cover of 15Li, except for 75Li, which showed nonuniform shrinkage in Figure 5.2. When the cover was changed to 15Li + LiOH, shrinkage was observed for all samples, except for 25Li which showed nonuniform shrinkage. 30Li and 65Li samples have relative densities of 58 and 55% with the cover of 15Li, respectively. The relative densities were all increased to 92% and 90% when the cover powder contained LiOH. As noted above, 75Li showed nonuniform shrinkage after the sintering with the 15Li cover, which indicates that sufficient excess LiOH could help with the densification. However, without LiOH in the cover, the shrinkage of 75Li was nonuniform. Subsequent studies focused on 30Li and 65Li samples as these samples all uniformly shrank after the sintering with the cover of 15Li + LiOH.

SEM images of fracture cross sections of 30Li and 65Li are shown in Figure 5.3. After sintering with 15Li cover, large pores were observed in Figure 5.3 (a)-(d). When the cover powder contained LiOH, fewer pores were observed as shown in Figure 5.3 (e)-(h). The fracture surface of the pellets sintered with 15Li cover powder consisted of smooth rounded surfaces (Figure 5.3 (b)(d)), but in the sample with 15Li + LiOH cover powder, flat surface indicative of brittle or transgranular facture surface were observed (Figure 5.3 (f)(h)) indicating that the grains are more connected when LiOH was added

in the cover powder. These results indicate that LiOH in the cover powder helped with the sintering of LLZTO.

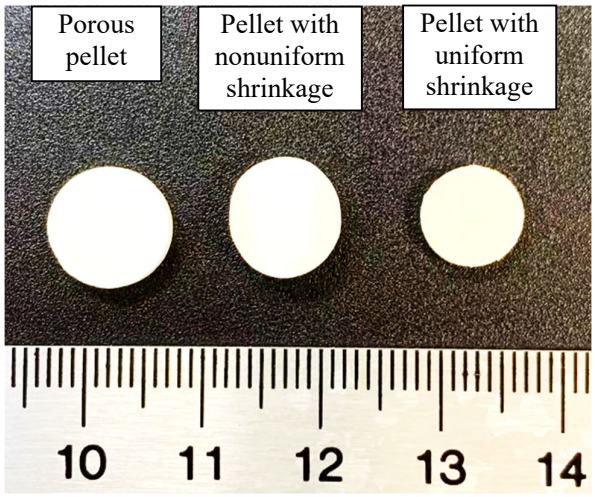

Figure 5.2 The photo of the porous pellet, nonuniform shrinkage pellet and uniform shrinkage pellet (from left to right)

Table 5.2 The shrinkage, relative density (4 samples for each composition), RT (20°C) total Li-ion conductivity, activation energy (Ea) (in the temperature range 20 to 80°C or 20 to 40°C) of samples sintered at 1100°C for 16 hours

Sample	15Li cover				15Li + LiOH cover			
	Shrinkage after sintering	Relative density (mean ± SD)	RT total σ_{Li+} (S/cm)	Ea (eV)	Shrinkage after sintering	Relative density (mean ± SD)	RT total σ_{Li+}(S/cm)	Ea (eV)
25Li	No	-	-	-	Nonuniform	-	-	-
30Li	No	58±2	2.0×10^{-5}	0.28	Uniform	92±2	4.2×10^{-4}	0.37
65Li	No	55±3	1.4×10^{-6}	0.39	Uniform	90±1	4.6×10^{-4}	0.34
75Li	Nonuniform	-	-	-	Uniform	91±1	2.9×10^{-4}	0.23

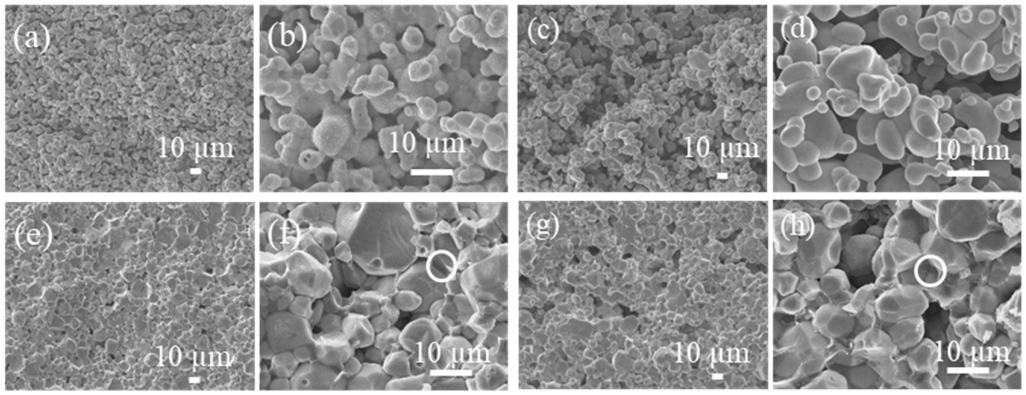

Figure 5.3 SEM images of fracture cross sections of LLZTO sintered at 1100°C for 16 hours with (a)-(d) cover powder of 15Li, (e)-(h) cover powder of 15Li + LiOH, (a)(b)(e)(f) for sample of 30Li, (c)(d)(g)(h) for sample of 65Li

The interparticle phase, which is circled in Figure 5.3(f)(h), contains aluminum according to the EDS results as shown in Figure 5.4. Figure 5.5 shows a fracture cross sectional SEM image of 65Li sintered at 1100°C for 32 hours with 15Li + LiOH cover powder. Corresponding elementary map of Al, Zr, La and Ta are shown in Figure 5.5 (b-e). Aluminum only exists at the phases between grains and this Al-containing phase contains less Zr, La and Ta than the grains.

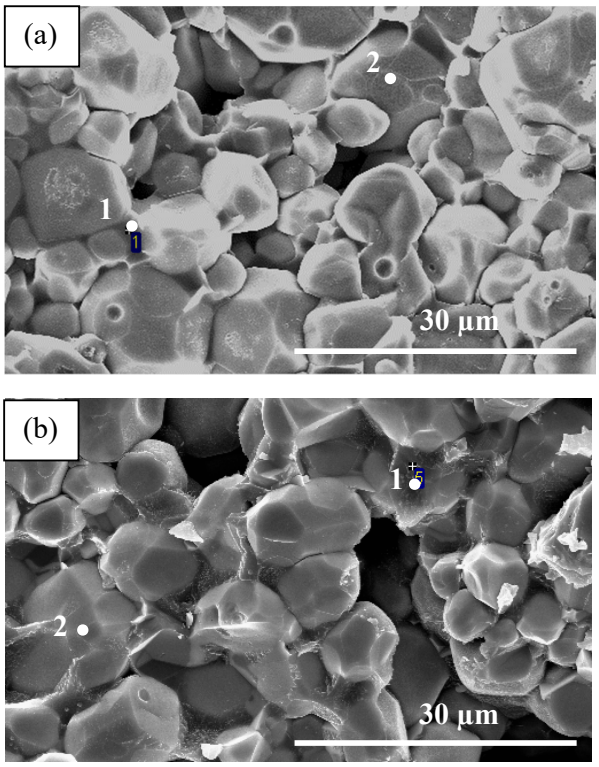

Spectrum	Al	Zr	La	Ta
1	70	10	17	3
2	-	36	55	9

Spectrum	Al	Zr	La	Ta
1	68	16	12	4
2	-	41	54	5

Figure 5.4 EDS results of the interparticle phase, EDS point of spectrum 1, on the sample of (a) 30Li, (b) 65Li, sintered at 1100°C for 16 hours with cover powder of 15Li + LiOH, concentrations are in atomic%

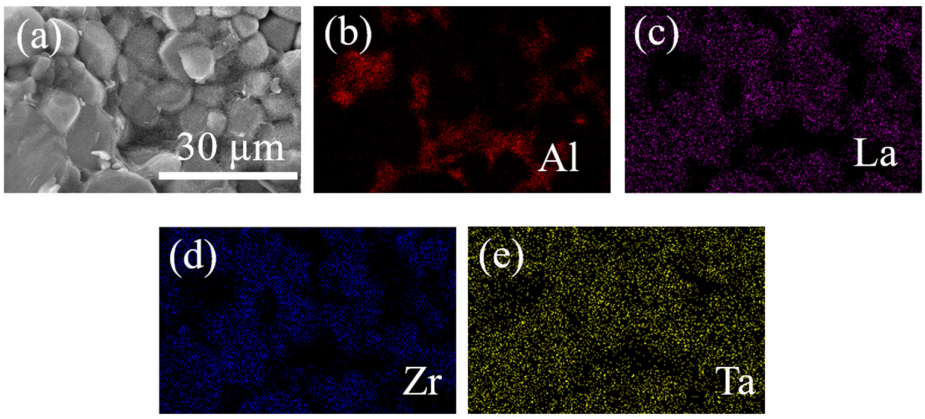

Figure 5.5 (a) SEM image of the fracture cross section of a 65Li pellet sintered at 1100°C for 32 hours with the cover powder of 15Li + LiOH, and the corresponding mapping of (b) Al, (c) La, (d) Zr and (e) Ta obtained from EDS analysis

The ICP results of LLZTO with different excess Li amount, which present the overall sample composition, are listed in Table 5.3, atomic ratios of Li:Al:La:Zr are normalized by La content as shown in the formula of $Li_{6.75}La_3Zr_{1.75}Ta_{0.25}O_{12}$. All samples contain aluminum. The maximum Li content in the garnet structure is 7.5 pfu [34,78,79], so the higher Li contents in 60Li, 75Li and 78Li samples indicate the presence of an additional lithium-containing phase.

Table 5.3 Composition from ICP analysis of $Li_{6.75}La_3Zr_{1.75}Ta_{0.25}O_{12}$ with different Li excess sintered at 1100°C for 16 hours with 15Li + LiOH cover, the ratio is normalized with respect to the La content

Excess Li (wt.%)	Li	Al	La	Zr
30	6.83	0.08	3	1.56
60	7.72	0.47	3	1.56
65	7.35	0.21	3	1.71
75	8.50	0.54	3	1.61
78	7.61	0.36	3	1.54

Compositions from ICP analysis of 65Li sintered with different cover powders are listed in Table 5.4. The amounts of aluminum and lithium are higher when the sample was sintered with a 15Li + LiOH cover. These results suggest that the 15Li + LiOH cover powder reduces the loss of Li and promotes the transfer of aluminum from the crucible to the sample.

Table 5.4 Composition from ICP analysis of 65Li sintered with different cover powders and different sintering hours

Cover powder	Sintering time (hours)	Li	Al	La	Zr
15Li	16	6.73	0.07	3	1.66
15Li + LiOH	16	7.35	0.21	3	1.71
	32	7.39	0.52	3	1.70

5.1.3 Conductivity

Room temperature impedance spectra for LLZTO with different Li excess amounts sintered at 1100°C for 16 hours with cover powders of 15Li or 15Li + LiOH are shown in Figure 5.6. As shown in the typical Nyquist plot for LLZTO pellets in Figure 5.6, the spectra were fit to an equivalent circuit of $L(R_tCPE_t)(R_eCPE_e)$, where L, R and CPE are the inductor, resistor and the constant phase element, and the subscript t and e refer to the total and electrode contribution, respectively. The first semicircle is attributed to the total resistance (R_t). The total conductivity is calculated as $\sigma_{total} = t / (A \times R_t)$, where t is the sample thickness and A is the cross-sectional area of the sample. The grain and grain boundary contributions cannot be separated, which is consistent with other works[43,55].

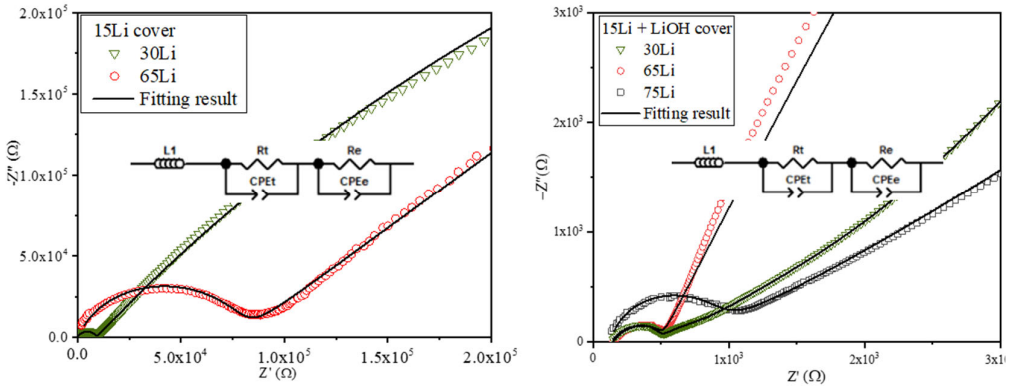

Figure 5.6 RT impedance spectra of LLZTO pellet sintered at 1100°C for 16 hours, (a) with 15Li cover powder, (b) with 15Li + LiOH cover powder. Data were fitted using the presented equivalent circuit of $L(R_tCPE_t)(R_eCPE_e)$.

The RT total Li-ion conductivities of different LLZTO pellets are listed in Table 5.2 and plotted in Figure 5.7. The RT total conductivity of 30Li with 15Li cover powders is 2.0×10^{-5} S/cm, which is significantly lower than that sintered with 15Li + LiOH cover powders (6.9×10^{-4} S/cm). Compared to the 30Li samples, 65Li also showed a lower RT σ_{total} when the cover was 15Li, but similar RT σ_{total} when the cover contained LiOH. 75Li has a RT σ_{total} of 2.9×10^{-4} S/cm, which is very close to the conductivities of 30Li and 65Li. The higher conductivity is consistent with the higher relative density in the samples sintered with 15Li + LiOH cover.

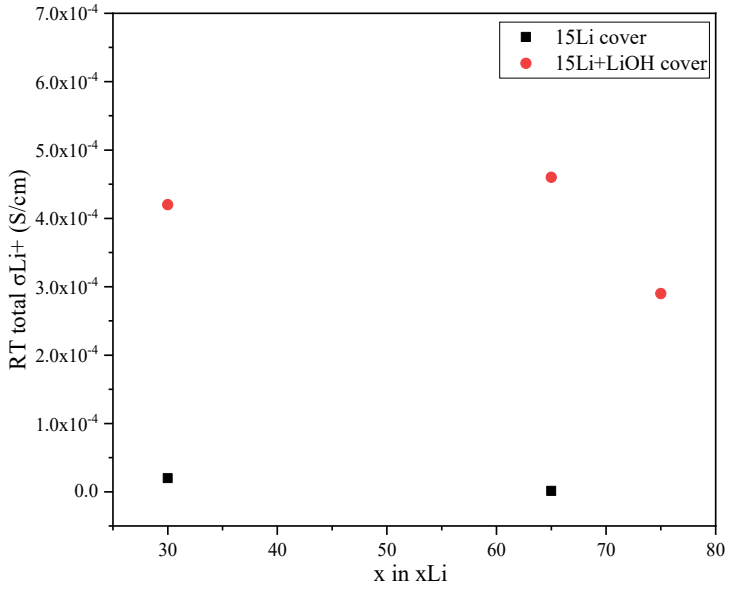

Figure 5.7 The RT total Li-ion conductivities of different LLZTO pellets sintered at 1100°C for 16 hours with different cover powders

Arrhenius plot of total Li-ion conductivities LLZTO samples with different Li excess amount with different cover powders are shown in Figure 5.8 and the corresponding activation energies (E_a) are listed in Table 5.2. The impedance spectra are shown in Appendix II. The activation energy for all samples is from 0.23 to 0.39 eV, but the conductivities of samples sintered with 15Li + LiOH cover powders are significantly higher than those sintered with the 15Li cover powders.

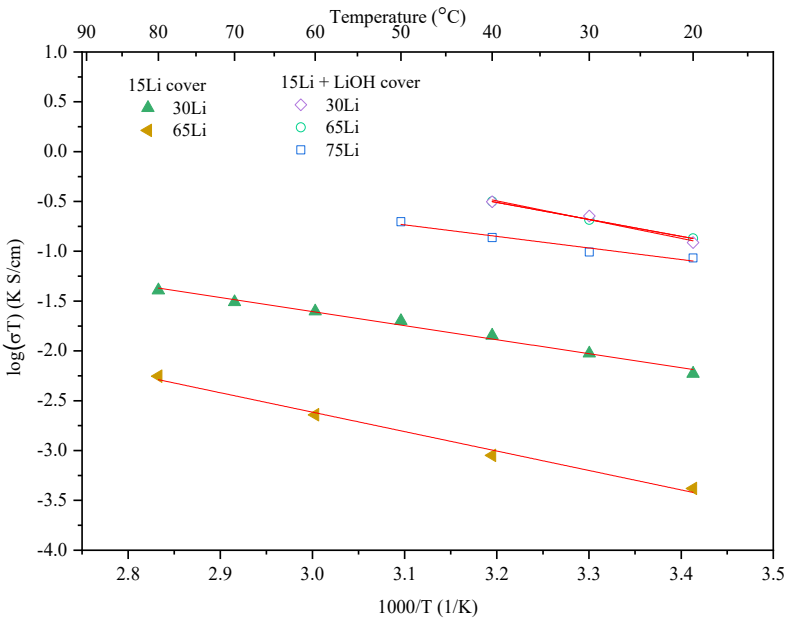

Figure 5.8 Arrhenius plot of total Li-ion conductivities for LLZTO pellets sintered at 1100°C for 16 hours, with cover powders of 15Li or 15Li + LiOH

5.1.4 Li site occupancy

To better understand the mechanism that leads to high Li-ion conductivity, the site occupancy on each of the two Li sites in the cubic phase garnet structure for samples with different Li concentrations sintered with 15Li + LiOH cover have been studied. Neutron diffraction experiments were performed on samples of 30Li, 65Li and 75Li. Compositions for initial refinement were obtained from ICP, the results of which are shown in Table 5.3. When the Li content measured by ICP is higher than 7.5, a lithium content of 7.5 was used as that is the maximum Li amount in the garnet framework [34,78,79]. The Al concentration from ICP result represents the overall bulk

concentration, and EDS indicates that the Al is mostly in the grain boundary phase (Figure 5.4 and 5.5). However, Al may exist in the grains at levels that are is too small to be detected by EDS [113]. To confirm the concentration of Al in the bulk region, atomic probe tomography (APT) was performed in the bulk region of one LLZTO sample ($Li_{6.75}La_3Zr_{1.75}Ta_{0.25}O_{12}$). The SEM image of the tip used for APT is shown in Appendix III. The concentration results from APT of Li/Al/La/Zr/Si/Ta is 7.46/0.012/3/1.62/0.15/0.23, which is normalized by La content. Aluminum was not added deliberately to the sample and presumably was transferred to the sample from the Al_2O_3 crucible during processing.

Atomic probe tomography also indicated the presence of Si, which also was not added deliberately and could have been transported from the Al_2O_3 crucible. The sintering time of 32 hours was only used for the sample used in APT, while samples in other tests are all sintered for 16 hours. It is assumed that Al and Si concentrations in the grains were the same between samples sintered for 16 and 32 hours. The APT test was performed on only one tip with the diameter of around 10 nm, so LA-ICPMS was performed on the same sample to confirm the presence of Si, which is shown in Appendix IV. All 5 line-scans across the surface each with a length of 425 μm confirmed the presence of Si. Therefore, in the Rietveld structure refinement, the Al concentration of 0.012 mole/formula and Si concentration of 0.15 mole/formula from ATP were used for all samples. Ta, which could not be analyzed using ICP, was assumed to be 0.25 mole/formula for all samples. Other concentrations were those determined

by ICP analysis. The Rietveld structure refinements are shown in Figure 5.9 and the refined structural parameters are summarized in Table 5.5. Although no impurities were detected by XRD, neutron diffraction indicated the presence of Li_2ZrO_3 and $LiAlO_2$.

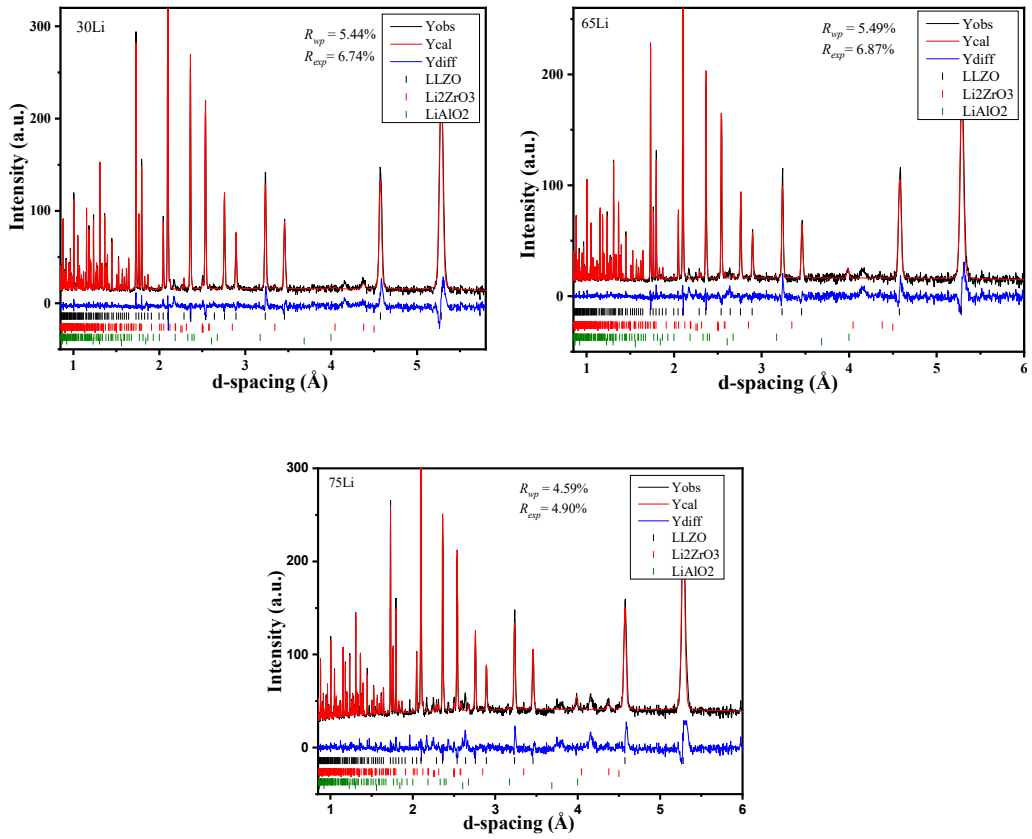

Figure 5.9 Rietveld refinement plot for different LLZTO samples from neutron diffraction data at room temperature (300K) using the space group of *Ia-3d*. The observed pattern, calculated profile and difference curve are plotted. The top markers (black) are for LLZO, the middle markers (red) are for Li_2ZrO_3, and the bottom markers (green) are for $LiAlO_2$

Table 5.5 Refinement structural parameters for different LLZTO samples at room temperature (300K)

	Atom	Site	Occupancy	x	y	z	U_{iso}(Å^2)
30Li	Li1	24d	0.639(21)	0.375	0	0.25	0.052(4)
	Al	24d	0.004	0.375	0	0.25	0.052(4)
	Li2	96h	0.399(8)	-0.5779(6)	0.1007(6)	0.1864(7)	0.026(2)
	La	24c	1	0.125	0	0.25	0.010(1)
	Zr	16a	0.78	0	0	0	0.004(1)
	Si	16a	0.075	0	0	0	0.004(1)
	Ta	16a	0.125	0	0	0	0.004(1)
	O	96h	1	-0.03123(7)	0.05364(8)	0.14823(7)	0.013(1)
	$Li_{6.70}Al_{0.012}La_3Zr_{1.56}Ta_{0.25}Si_{0.15}O_{11.91}$, a=12.94074(4) Å, R_{wp}=5.44%, R_p=6.74%, χ^2=1.9						
65Li	Li1	24d	0.640(24)	0.375	0	0.25	0.042(4)
	Al	24d	0.004	0.375	0	0.25	0.042(4)
	Li2	96h	0.436(9)	-0.5781(7)	0.1005(7)	0.1872(7)	0.030(1)
	La	24c	1	0.125	0	0.25	0.009(1)
	Zr	16a	0.855	0	0	0	0.006(1)
	Si	16a	0.075	0	0	0	0.006(1)
	Ta	16a	0.125	0	0	0	0.006(1)
	O	96h	1	-0.03128(7)	0.05428(8)	0.14890(8)	0.012(1)
	$Li_{7.15}Al_{0.012}La_3Zr_{1.71}Ta_{0.25}Si_{0.15}O_{12.44}$, a = 12.95787(4) Å, R_{wp}=5.49%, R_p=6.87%, χ^2=1.73						
75Li	Li1	24d	0.704(33)	0.375	0	0.25	0.056(5)
	Al	24d	0.004	0.375	0	0.25	0.056(5)
	Li2	96h	0.390(12)	-0.5773(9)	0.1008(9)	0.1863(10)	0.024(4)
	La	24c	1	0.125	0	0.25	0.009(1)
	Zr	16a	0.805	0	0	0	0.004(1)
	Si	16a	0.075	0	0	0	0.004(1)
	Ta	16a	0.125	0	0	0	0.004(1)
	O	96h	1	-0.03120(10)	0.05411(11)	0.14849(11)	0.012(1)
	$Li_{6.79}Al_{0.012}La_3Zr_{1.61}Ta_{0.25}Si_{0.15}O_{12.12}$, a = 12.94312(7) Å, R_{wp}=4.59%, R_p=4.90%, χ^2=2.32						

Table 5.6 The Li concentration, lattice parameter, Li site occupancy based on Rietveld refinement and RT σ_{total} for different samples

sample	Li content from refinement	Lattice parameter (Å)	Li1 24d		Li2 96h		RT total σ_{Li+} (S/cm)
			Site occupancy	Li amount	Site occupancy	Li amount	
30Li	6.70	12.94074(4)	0.639(21)	1.92	0.399(8)	4.78	4.2×10^{-4}
65Li	7.15	12.95787(4)	0.640(24)	1.92	0.436(9)	5.23	4.6×10^{-4}
75Li	6.79	12.94312(7)	0.704(33)	2.11	0.390(12)	4.68	2.9×10^{-4}

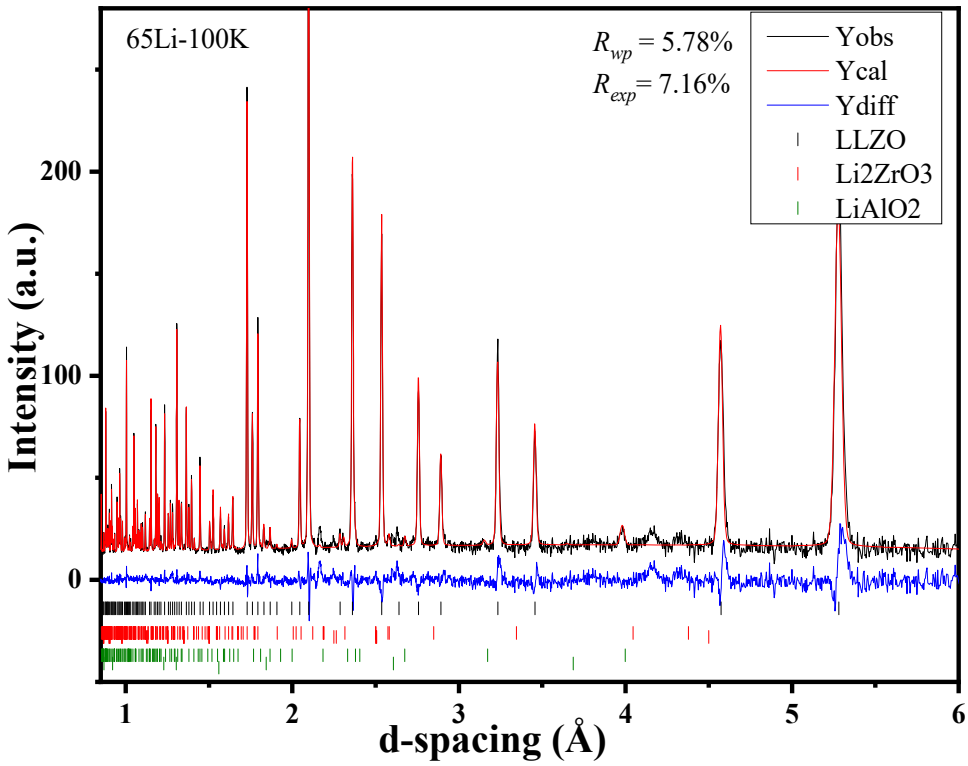

Figure 5.10 Rietveld refinement plot for sample 65Li from neutron diffraction data at 100K using the space group of *Ia-3d*. The observed pattern, calculated profile and difference curve are plotted. The top markers (black) are for LLZO, the middle markers (red) are for Li_2ZrO_3, and the bottom markers (green) are for $LiAlO_2$

Table 5.7 Refinement structural parameters for sample 65Li at 100K

sample	Atom	Site	Occupancy	x	y	z	U_{iso}(Å^2)
65Li	Li1	24d	0.679(24)	0.375	0	0.25	0.038(4)
	Al	24d	0.004	0.375	0	0.25	0.038(4)
	Li2	96h	0.410(9)	-0.5761(6)	0.1008(5)	0.1861(6)	0.016(2)
	La	24c	1	0.125	0	0.25	0.007(1)
	Zr	16a	0.855	0	0	0	0.004(1)
	Si	16a	0.075	0	0	0	0.004(1)
	Ta	16a	0.125	0	0	0	0.004(1)
	O	96h	1	-0.03162(7)	0.05461(8)	0.14913(8)	0.010(1)
	$Li_{7.15}Al_{0.012}La_3Zr_{1.71}Ta_{0.25}Si_{0.15}O_{12.44}$, a=12.93373(5) Å, R_{wp}=5.78%, R_p=7.16%, χ^2=1.88						

Sample 65Li was also tested at 100K. The Rietveld structure refinement are shown in Figure 5.10 and the refined structural parameters are summarized in Table 5.7. Heating from 100K to 300K resulted in an expansion in lattice parameter by 0.186%, a decrease in the 24d Li site occupancy and an increase in 96h Li site occupancy, which is similar to other reported works [65,72,74]. The change in the Li site occupancy also indicated that there was a small redistribution of Li ions from 24d Li site to the 96h Li site.

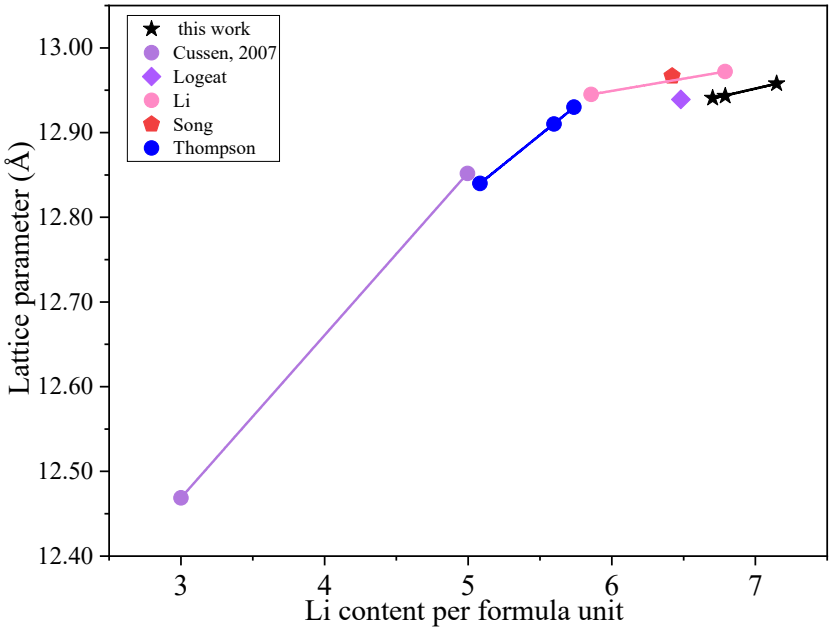

Figure 5.11 The lattice parameter at different Li content, ★ this work [40,67–69,75]

The Li content, lattice parameter, Li site occupancy from the Rietveld refinements and the corresponding RT Li-ion total conductivities are summarized in Table 5.6. The lattice parameters and the corresponding Li content from both this work and reported work are plotted in Figure 5.11. The reported works using the same doping element of Ta are used in this figure. The lattice parameter increases with increasing Li content, which is expected since more Li ions are introduced to the garnet structure while other cations' amount are similar.

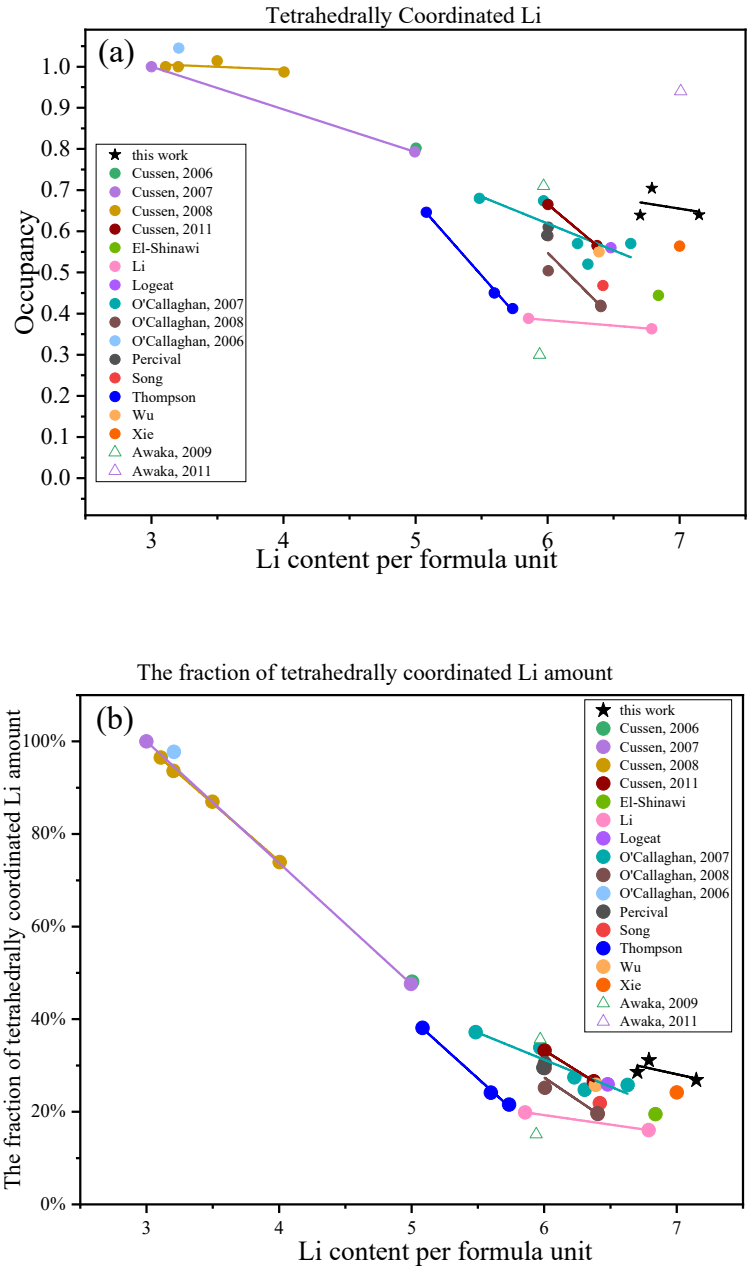

Figure 5.12 (a) The occupancy of tetrahedral site occupied by Li ions at different Li content, (b) the fraction of tetrahedrally coordinated Li amount, ★ this work, ● work based on neutron diffraction, △work based on XRD [22,26,40,62,64,66–77]

The site occupancy on the tetrahedrally ordinated (24d) Li site from both this work

and the literature are plotted in Figure 5.12(a). Each point represents one Li content, while the lines are the fitting lines for different Li contents when multiple concentrations from a given study were reported. In this work (labeled by ★), the Li content is high and is in the range of 6.70-7.15 mole pfu. For a low Li content of 3-4 mole pfu, the 24d sites are almost fully occupied with an occupancy value near 1 [62,64,69]. In the Li content range of 4-6.5 mole pfu, several reports from literature indicate that the 24d site occupancy decreases with the increasing Li content [22,40,65–75]. When the Li content is larger than 6.5 mole pfu, the 24d site occupancy is in the wide range of 0.36-0.70 [26,40,76,77].

To better understand the 24d Li site occupancy at different Li contents, the fraction the Li amount at 24d site (the amount of Li at 24d / total Li content used in the Rietveld refinement) has been calculated and plotted in Figure 5.12(b). This figure indicates that the Li amount at the 24d site decreases with the increasing Li content in the range of 3-7.15 mole pfu. In this work, for the high Li content in the range of 6.70-7.15 mole pfu, although the fraction of 24d Li site decreases with the increasing Li content, the Li content was a little higher than those in the Li content of 6.2-7 pfu in literature.

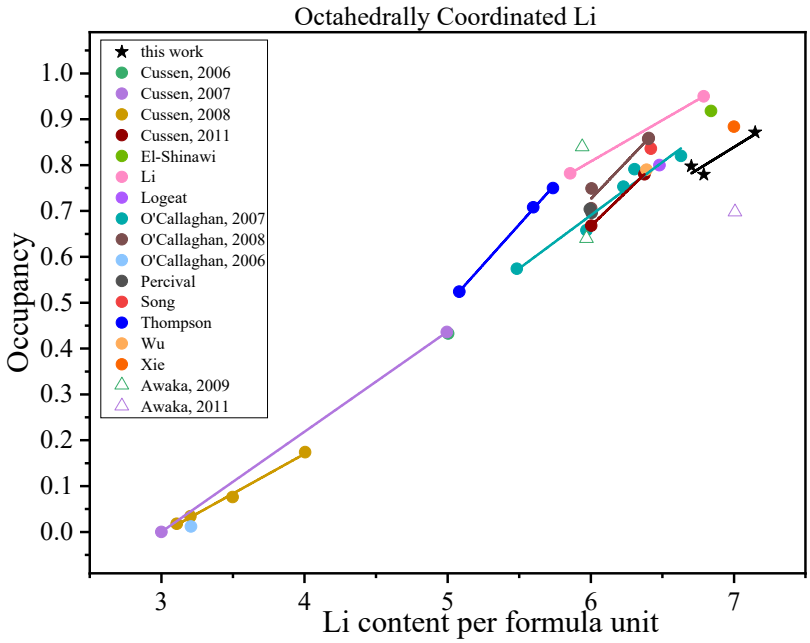

Figure 5.13 The occupancy of octahedral site occupied by Li ions at different Li content, ★ this work, ● work based on neutron diffraction, △work based on XRD [22,26,40,62,64,66–77]

The site occupancy on the octahedrally ordinated (96h) Li site of both this work and the literature are plotted in Figure 5.13. For a low Li content of 3-3.5 mole pfu, the 96h sites are almost empty with an occupancy value smaller than 0.05. The 96h Li site occupancy was found to increase with the increasing Li content in the range of 3-7.25 mole pfu. There is general agreement among the results except for Cussen and O'Callaghan's work that reported 96h Li site occupancy in the range of 0.57-0.82 for Li content in the range of 5.5-6.6 [71]. This 96h Li site occupancy is higher than other reported works and this work, which is 0.32-0.48 for Li content in the range of 5.5-7.15 mole pfu.

The results in Figure 5.12 and 5.13 show that the fraction of Li amount on 24d Li site decreases and 96h Li site occupancy increases with the increasing Li content in the range of 3-7.15 mole pfu. Therefore, in the whole range of 3-7.15 mole pfu, when the Li content increases, the Li ions leave the 24d Li sites and sit on the 96h sites which results in the decreasing in the Li amount on 24d Li site. The 24d Li site occupancy decreases with the increasing Li content in the range of 3-6.5 mole pfu while evenly distributes in the Li content range of 6.5-7.15 mole pfu. The 96h Li site occupancy increases with the increasing Li content in the whole Li range of 3-7.15 mole pfu.

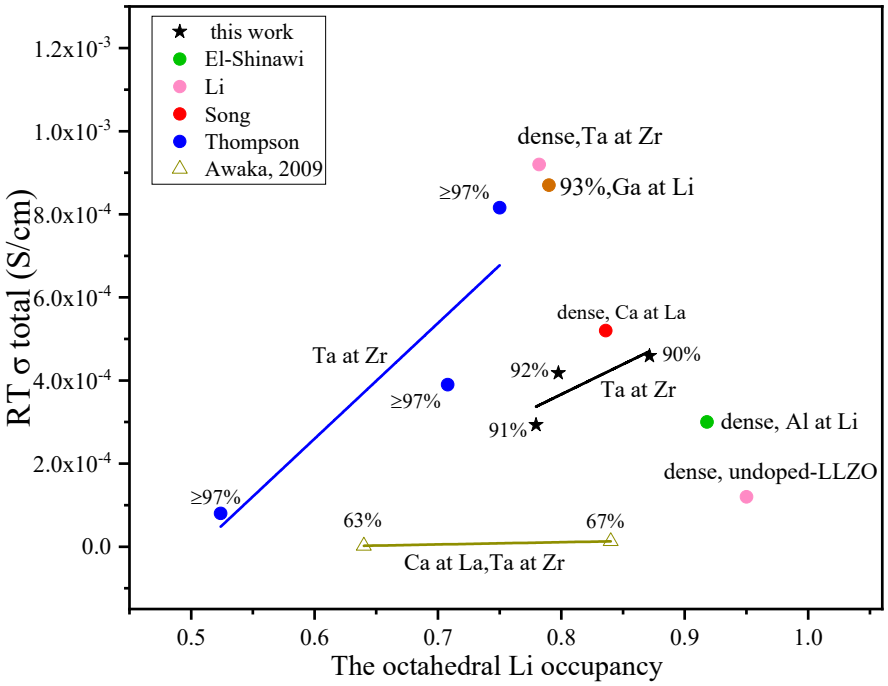

Figure 5.14 The RT Li-ion total conductivities with different occupancies of octahedrally coordinated Li, ★ this work, ● work based on neutron diffraction, △ work based on XRD [22,40,67,68,77]

The Li ions on the octahedral site (96h) are highly mobile and are involved in the hopping from one edge shared oxide octahedron to another, so when the occupancy at 96h Li site is low, the Li ion conductivity is also low (10^{-6} S/cm) [63–65]. Increasing the concentration of Li ions on the 96h Li site significantly improves the conductivity [40,50,65–68]. The RT total Li-ion conductivities and the corresponding 96h Li site occupancy from literature and this work are plotted in Figure 5.14. The relative density and doping information are also presented in the figure as they are also very critical in controlling the Li-ion conductivity. The lines are the linear fits for those studies where in which results for multiple lithium concentrations were reported. For the low relative density of 63-67%, the RT Li-ion total conductivities are low, but slightly increase with the 96h Li site occupancy [22]. From the work of Thompson et al., using the same doping element as in this work, the RT Li-ion total conductivities increased with the increasing 96h Li site occupancy in the occupancy range of 0.26-0.38 [67]. The RT Li-ion total conductivity values in this work are below the fitting line of Thompson et al. work which is probably due to the lower relative densities in this work (~90% vs ≥97% in Thompson et al.) [67]. In this work, except for the lower RT Li-ion total conductivity values, in the occupancy range of 0.39-0.44, the RT Li-ion total conductivities also increased with the increasing 96h Li site occupancy. The dense sample using Ta as the doping element in Li et al. work [40] has the highest 96h Li site occupancy and the highest conductivity value in Figure 5.14. Therefore, the Li-ion conductivity increases

with the octahedral Li occupancy, with an occupancy value in the range of 0.52-0.87. The two samples with Li occupancies greater than 0.9 have lower conductivity which could be the result of the reduction of the number of vacancies on the octahedral sites (i.e. <10%).

5.2 The effect of sintering time on 65Li with 15Li + LiOH cover powders

5.2.1 Structure

The XRD patterns of 65Li samples sintered at 1100°C for 1, 2, 4, 8, 16 and 32 hours with the cover powder of 15Li + LiOH are shown in Figure 5.15. All spectra contained peaks for only the cubic garnet phase.

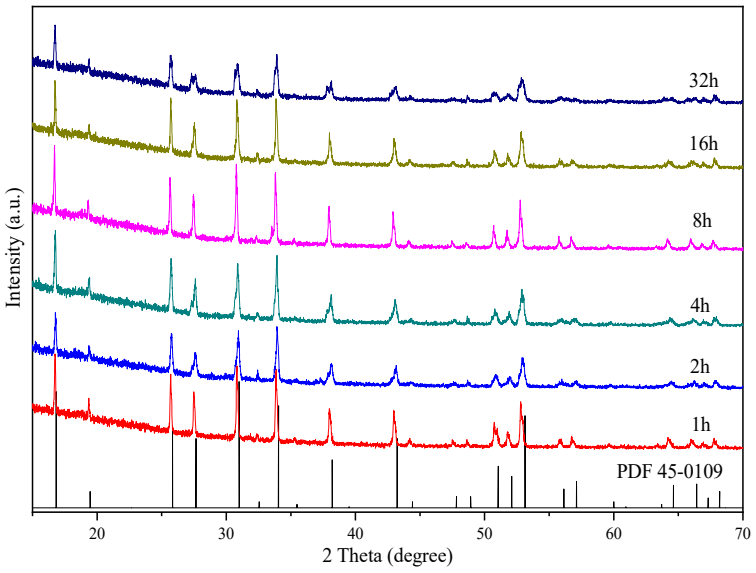

Figure 5.15 XRD patterns of 65Li sintered at 1100°C for different sintering time with cover powder of 15Li + LiOH

The lattice parameters calculated from Figure 5.15 are listed in Table 5.8. The lattice parameter ranged from 12.937 Å to12.968 Å. Pellets sintered at 1 and 8 hours have a lattice parameter around 12.965 Å, which is larger than that of others (~12.940 Å). When the sintering time is 16 hours or longer, the lattice parameter is around 12.945 Å, which are similar to literature [59,121,122].

Table 5.8 Lattice parameter of 65Li sintered at 1100°C for different sintering time with cover powder of 15Li + LiOH, 6 samples for each composition

Sintering time (hours)	Lattice parameter (Å) (mean ± SD)
1	12.965±0.002
2	12.937±0.017
4	12.938±0.005
8	12.968±0.001
16	12.942±0.011
32	12.947±0.013

5.2.2 Morphology, relative densities and composition

SEM and BSE images of fracture cross sections of 65Li sintered at 1100°C for 1, 2, 4, 8, 16 and 32 hours with the cover powder of 15Li + LiOH are shown in Figure 5.16. After sintering for 1 hour (Figure 5.16 (a)), there are connected pores and many small grains with sizes of 2-3 μm connected by an interparticle phase. After sintering

for 4 hours (Figure 5.16 (c)), the grains grew and became better connected. After 8 hours (Figure 5.16 (d)), the grains have continued to grow, and the pores were reduced and did not appear to be connected. The BSE images in Figure 5.16 (g)-(h), in which the interparticle phase is darker than the grains, show that as the grain size increased, the amount of the interparticle phase decreased and the samples are still porous after the sintering of 1 hour to 8 hours (Figure 5.16 (a)-(d)). There is little change between 8, 16 and 32 hours sintering, as shown in Figure 5.16 (d)-(f).

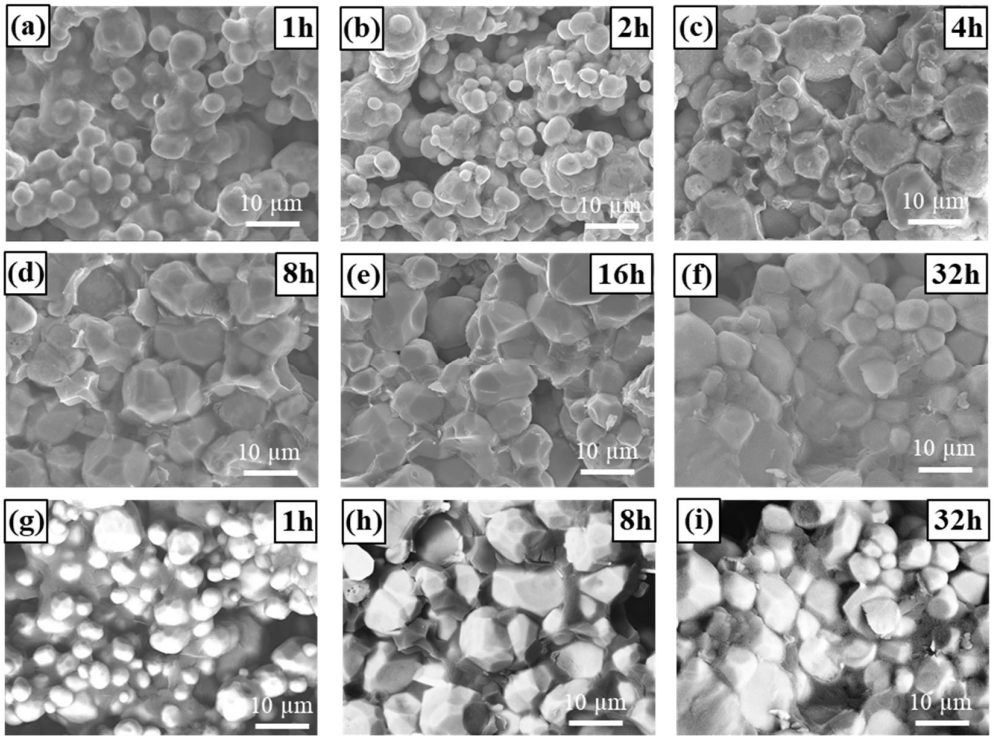

Figure 5.16 (a)-(f) SEM images of fracture cross sections of 65Li sintered at 1100°C for 1, 2, 4, 8, 16 and 32 hours, (g)-(i) BSE images of fracture cross sections of 65Li sintered at 1100°C for 1, 8 and 32 hours, all with the cover powder of 15Li + LiOH

The relative densities of these pellets shown in Table 5.9 follows a similar trend to observation of the morphology. The relative density is only 62% for pellets sintered for 1 hours, and it is larger than 80% for 8 to 32 hours. Samples sintered for 16 and 32 hours have similar relative density of 90%.

Table 5.9 The relative densities of 65Li sintered at 1100°C for 1, 4, 8, 16 and 32 hours (4 samples for each sintering time) with the cover powder of 15Li + LiOH

Sintering time (hour)	Relative density (% mean ± SD)
1	62 ± 3
4	61 ± 10
8	83 ± 3
16	90 ± 1
32	90 ± 2

The elemental concentrations from EDS of the interparticle phase for 65Li sintered at 1100°C for 1, 2, 4, 8, 16, 32 hours are listed in Table 5.10. After sintering for 1 hour, the interparticle phase contains high amounts of Cl but no Al. With continued sintering, the amount of Cl decreased and after 4 hours, Al was present with Cl. After sintering for 8 hours or longer, there was no Cl. This is consistent with the BSE images in Figure 5.16 (g)-(i), in which the interparticle phase is darker than the grains, which means this interparticle phase contains light elements such as Cl, Al and Li. The Cl presumably

comes from the starting material of $ZrOCl_2 \cdot 8H_2O$, while the Al presumably comes from the alumina crucible. Since the sample is not in direct contact with the alumina crucible, the aluminum is likely transferred from the crucible via a vapor phase and/or a liquid phase in a lithium-rich air atmosphere, which is created by the LLZTO + LiOH cover powder. Chlorine is used in chemical vapor deposition and may facilitate transfer of aluminum from the alumina crucible to the sample via a vapor phase [123]. According to the Li_2O-Al_2O_3 phase diagram, a liquid phase exists in the temperature range of 1055-1100°C [124]. This Al-containing liquid phase may also facilitate the transfer of aluminum from the alumina crucible to the sample.

Table 5.10 The elemental information from EDS of the interparticle phase between grains for 65Li sintered at 1100°C for 1, 2, 4, 8, 16, 32 hours with the cover powder of 15Li + LiOH. The composition does not Include Li or O since Li could not be measured, and the amount of O determined by EDS is highly uncertain and may skew the results (concentrations are in atomic%)

Sintering time (hours)	Al	Cl	La	Zr	Ta
1	0	74	18	7	2
2	0	11	57	52	7
4	78	6	4	9	2
8	44	0	29	21	6
16	68	0	12	16	4
32	88	0	4	4	4

Compositions from ICP analysis of 65Li sintered with different sintering times are listed in Table 5.11, atomic ratio of Li:Al:La:Zr is normalized by La content as shown in the formula of $Li_{6.75}La_3Zr_{1.75}Ta_{0.25}O_{12}$. The amount of aluminum increases with increasing sintering time when sintering with a 15Li + LiOH cover. As aluminum only exists at the phases between grains (Figure 5.16), the amount of Al-containing phase in the dense pellets also likely increases with the sintering time.

Table 5.11 Composition from ICP analysis of 65Li sintered with different cover powders and different sintering times

Cover powder	Sintering time (hours)	Li	Al	La	Zr
15Li + LiOH	16	7.35	0.21	3	1.71
	32	7.39	0.52	3	1.70

5.4.2 Conductivity

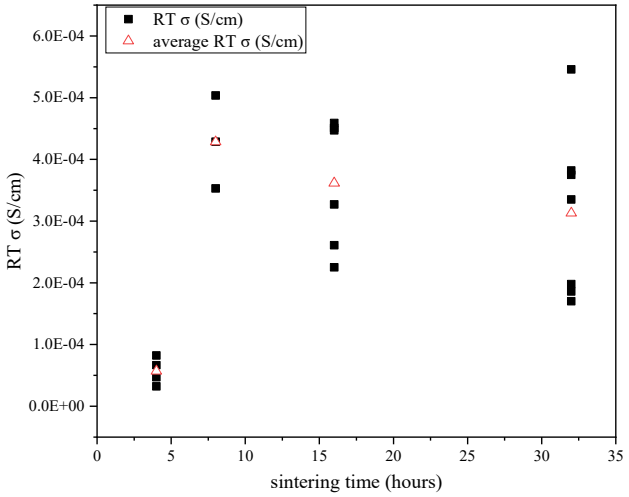

Figure 5.17 RT total Li-ion conductivities of 65Li sintered at 1100°C for different sintering time of 4, 8, 16, and 32 hours with the cover powder of 15Li + LiOH

The RT total Li-ion conductivities of 65Li pellets sintered for 4 to 32 hours are shown in Figure 5.17 and listed in Appendix V. The conductivity increases significantly after 4 hours sintering, and it does not change significantly between 8 and 32 hours. The relative densities of these pellets shown in Table 5.9 follows a similar trend to that of the total Li-ion conductivities. The relative density is only 61% for pellets sintered for 4 hours, and it is larger than 80% for 8 to 32 hours. Samples sintered for 16 and 32 hours have similar relative density of 90%. The increased amount of Al-containing phase in the sample sintered with 32 hours may be one reason that the conductivity does not increase as much as might be expected from the relative density change from 83 to 90%.

5.3 Conclusion

The addition of LiOH to the LLZTO cover powder used to minimize vaporization from the LLZTO pellet during the sintering has been shown to improve densification and increase Li-ion conductivity, such that a relative density of 92% and a total Li-ion conductivity of 4.6×10^{-4} S/cm was achieved through a simple co-precipitation method with cold uniaxial pressing and sintering in air. The 15Li + LiOH cover powder results in the formation of an Al-containing interparticle phase, which facilitates the densification of LLZTO. The aluminum concentration increases during sintering and is located in the grain boundary. The increased aluminum content promoted phase stabilization and densification, but the Al-containing phase also limits LLZTO phase continuity. The Li-ion conductivity value reached 4.28×10^{-4} S/cm at a sintering time of 8 hours and did not change significantly between 8 and 32 hours.

With the increasing Li content in the Li range of 3-7.15 mole pfu, the Li ions leave the 24d Li sites and sit on the 96h sites, and thereby resulting a decreasing in the Li amount on 24d Li site. The RT Li-ion total conductivity increases with the 96h Li site occupancy, which is consistent with the conclusion that the Li ions on the octahedral site (96h) are highly mobile and are involved in the hopping for the Li ion diffusion [63–65].

Chapter 6. The effect of Cl-containing salts on the phase, relative density and Li-ion conductivity of LLZTO

To determine the role of Cl in the densification of $Li_{6.75}La_3Zr_{1.75}Ta_{0.25}O_{12}$ (LLZTO), $ZrOCl_2*8H_2O$, the Cl-containing salt used in the preparation of LLZTO in Chapter 5, was replaced by $Zr(OH)_4$ and the results are described in this chapter. In this chapter, 65 wt.% excess Li (referred to 65Li in Chapter 5) and the cover powder of 15Li + LiOH were used. The structure, morphology, composition and Li-ion conductivity results are presented. The results of LLZTO prepared by $ZrOCl_2*8H_2O$ in Section 5.2 are used for comparison.

6.1 Structure

The XRD patterns of LLZTO sintered at 1100°C for different sintering time are shown in Figure 6.1. The pure cubic phase was obtained for all samples. The corresponding lattice parameters and the lattice parameters of LLZTO prepared with $ZrOCl_2*8H_2O$ (Table 5.7) are listed in Table 6.1. The lattice parameter of LLZTO sintered at 1 hour is not listed in the table as the value is not accurate because of the broad peaks. The lattice parameters for LLZTO sintered with $Zr(OH)_4$ salts are similar at different sintering times and they are in the range of 12.928 Å to 12.939 Å, which are a little smaller than those sintered with $ZrOCl_2*8H_2O$.

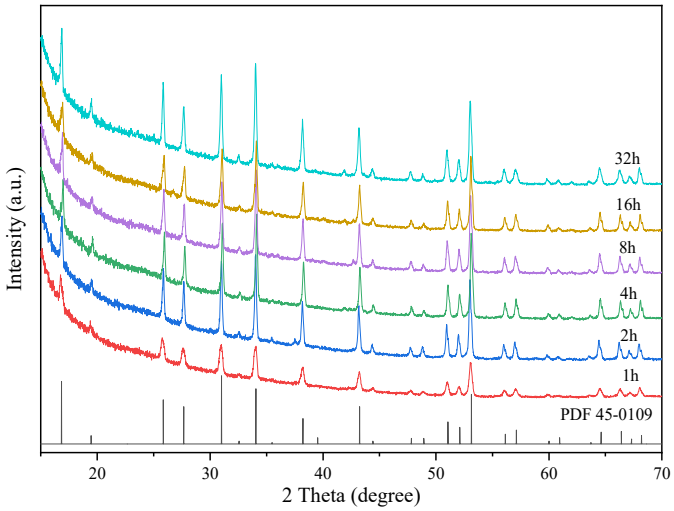

Figure 6.1 XRD patterns of $Li_{6.75}La_3Zr_{1.75}Ta_{0.25}O_{12}$ prepared with $Zr(OH)_4$ salt at 1100°C for different sintering times

Table 6.1 Lattice parameters of LLZTO sintered with different Zr salts for different sintering times

Sintering time (hours)	$Zr(OH)_4$	$ZrOCl_2*8H_2O$
	Lattice parameter (Å) (mean ± SD)	Lattice parameter (Å) (mean ± SD)
2	12.939±0.001	12.937±0.017
4	12.934±0.001	12.938±0.005
8	12.933±0.002	12.968±0.001
16	12.929±0.001	12.942±0.011
32	12.928±0.001	12.947±0.013

6.2 Relative density, morphology and composition

The relative densities of LLZTO sintered at 1100°C for different sintering time are listed in Table 6.2. The LLZTO sintered for 16 hours has a relative density of around 75%, which is larger than the porous LLZTO pellets' relative density of around 55% (Table 5.2). Therefore, the densification also occurred when $Zr(OH)_4$ were used to prepare LLZTO. All the relative densities are in the range of 74-84%. Considering the error range of 3-14%, LLZTO samples sintered with different sintering times have similar relative densities.

Table 6.2 Average relative density (6 samples for each sintering time) and average RT (20°C) total Li-ion conductivity (4-6 samples for each sintering time) of LLZTO prepared with $Zr(OH)_4$ sintered at 1100°C for different sintering time

Sintering time (hours)	Relative density (mean ± SD)	RT total σ_{Li+}(S/cm) (mean ± SD)	Ea (eV) (mean ± SD)
1	80±14	$(2.74\pm0.2) \times 10^{-5}$	0.41±0.08
2	79±8	$(1.32\pm0.9) \times 10^{-4}$	0.32±0.07
4	83±9	$(2.01\pm0.7) \times 10^{-4}$	0.28±0.05
8	74±3	$(1.83\pm0.9) \times 10^{-4}$	0.31±0.04
16	75±5	$(2.31\pm0.9) \times 10^{-4}$	0.28±0.08
32	76±8	$(2.50\pm1.1) \times 10^{-4}$	0.31±0.05

SEM images of the fracture cross sections of LLZTO samples are shown in Figure

6.2 and Figure 6.3. The low magnification SEM images in Figure 6.2 show that LLZTO sintered for 1 and 2 hours contain many connected pores and small grains (size of less than 10 μm). The grain growth began when the sintering time was 4 hours. And the grain size was similar with the sintering time of 8, 16 and 32 hours, which is in the range of 10-30 μm. The high magnification SEM images in Figure 6.3 show a few interparticle phases between grains, which are circled in the images. The interparticle phases were present between all grains when the sintering time is over 8 hours and therefore were not circled in the images. The fracture surfaces and interparticle phases between grains are similar to those LLZTO prepared with Cl-containing salt (Figure 5.3).

The EDS results of LLZTO sintered for 16 hours are shown in Figure 6.4, others could be found in Appendix VI. From the EDS results, the interparticle phase (spectra 1 and 2) contains aluminum as that in the LLZTO prepared with Cl-containing salt. The overall composition of LLZTO sintered with different Zr salts were also found to be similar (spectrum 5 in LLZTO prepared with $Zr(OH)_4$ and spectrum 8 in LLZTO prepared with $ZrOCl_2*8H_2O$).

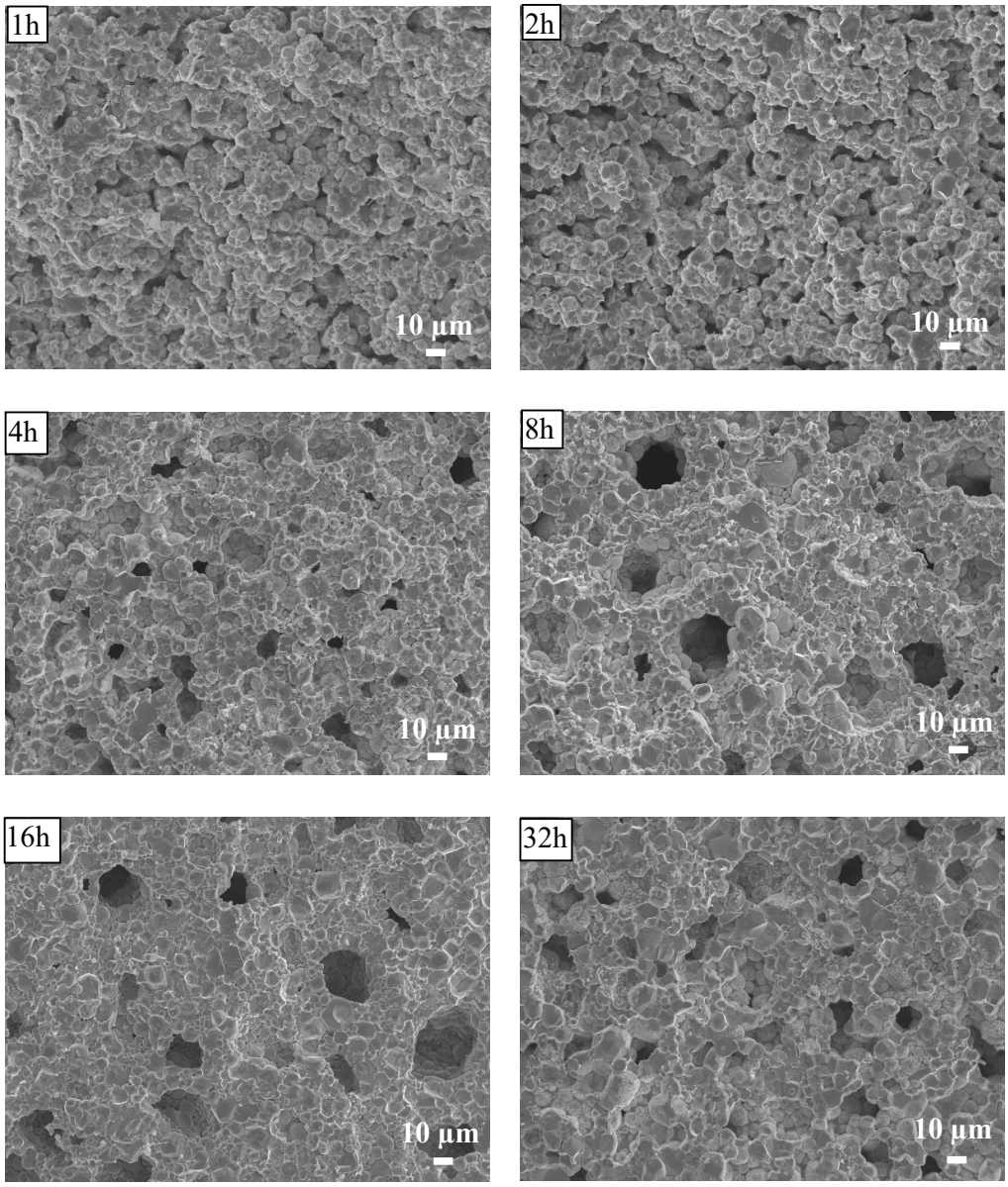

Figure 6.2 SEM images of the fracture cross sections of $Li_{6.75}La_3Zr_{1.75}Ta_{0.25}O_{12}$ prepared with $Zr(OH)_4$ salt and sintered at 1100°C for different sintering times at low magnification

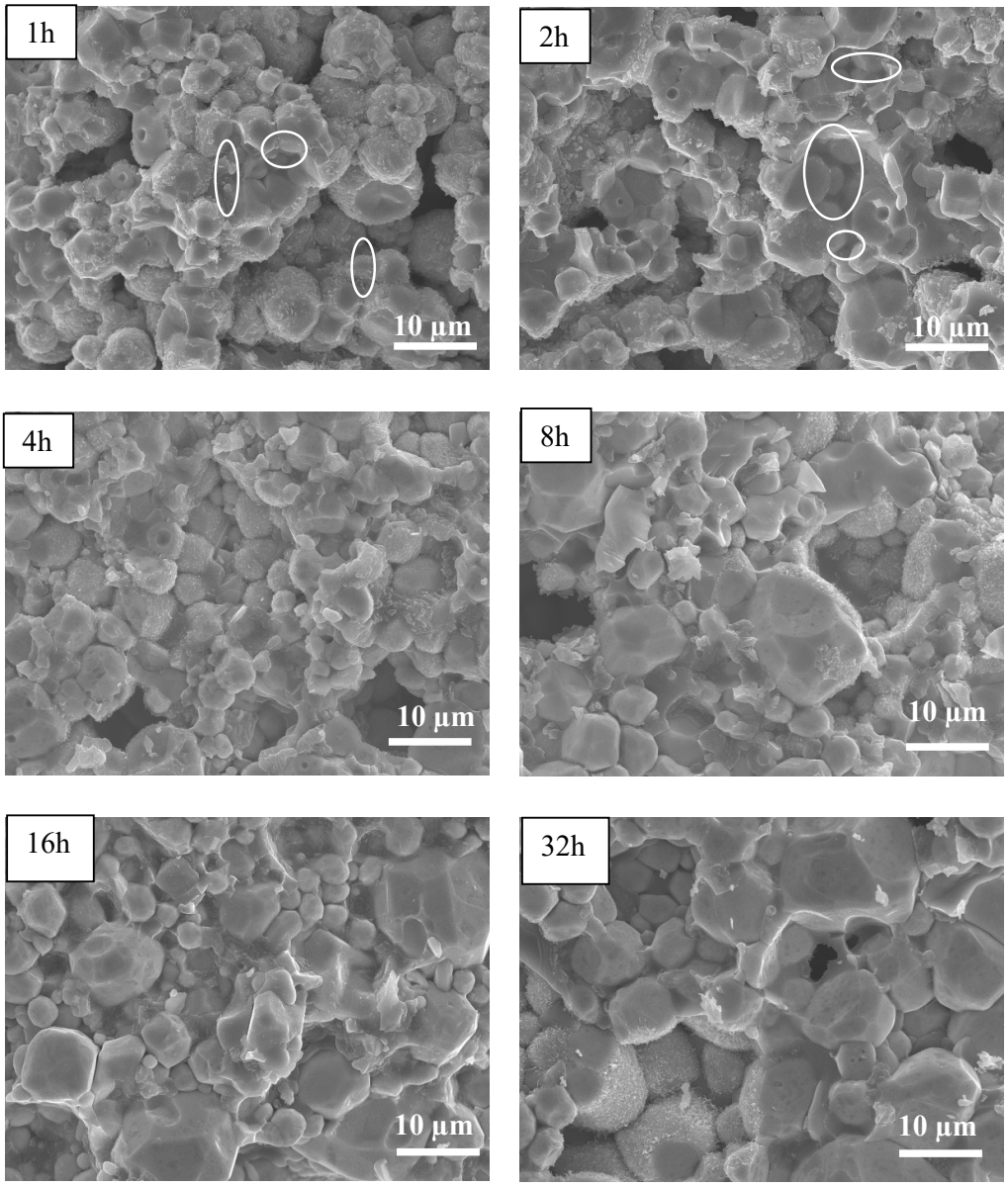

Figure 6.3 SEM images of the fracture cross sections of $Li_{6.75}La_3Zr_{1.75}Ta_{0.25}O_{12}$ prepared with $Zr(OH)_4$ salt and sintered at 1100°C for different sintering times at high magnification

$Zr(OH)_4$

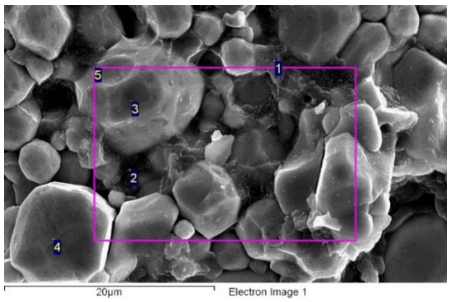

Spectrum	Al	Zr	La	Ta
1	78	9	9	4
2	11	16	68	5
3	0	33	52	15
4	0	38	51	11
5	22	37	30	11

$ZrOCl_2$* $8H_2O$

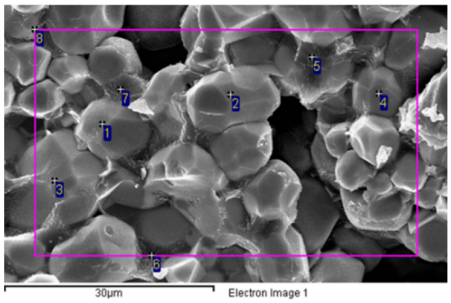

Spectrum	Al	Zr	La	Ta
1	0	44	51	5
2	0	45	50	5
3	0	41	54	5
4	0	47	47	6
5	68	16	12	4
6	63	11	26	0
7	62	18	18	3
8	26	31	37	6

Figure 6.4 EDS results of $Li_{6.75}La_3Zr_{1.75}Ta_{0.25}O_{12}$ prepared with different Zr salts and sintered at 1100°C for 16 hours, all results are in atomic%

6.3 Conductivity

Room temperature impedance spectra for LLZTO sintered with different sintering time are shown in Figure 6.5. All the spectra were fit to an equivalent circuit of $L(R_tCPE_t)(R_eCPE_e)$, the same equivalent circuit used for LLZTO prepared with Cl-containing salt in Chapter 5. The average RT total Li-ion conductivities (RT total σ_{Li+}) are listed in Table 6.2 and plotted in Figure 6.6(a). LLZTO sintered for 1 hour has a much smaller RT total σ_{Li+} than others. The RT total σ_{Li+} increased with sintering time for the 4 hours After 4 hours, RT total σ_{Li+} was around 2×10^{-4} S/cm and changed little with increasing sintering time. All the individual conductivity results with the

corresponding relative densities are plotted in Figure 6.6 (b). The RT total σ_{Li+} increases with the increasing relative density. LLZTO sintered for 1 hour has the lowest RT σ_{total}. The average RT total σ_{Li+} of LLZTO pellets sintered for 2 hours is around 1.32×10^{-4} S/cm, which is just a little smaller than those sintered for 4-32 hours. However, in Figure 6.6(b), with the similar relative densities, LLZTO pellets sintered for 2 hours have a lower RT total σ_{Li+}. The poor grain connection is assumed to be the main reason. When the samples were sintered for 4 hours or longer, all the relative densities and conductivities are in a wide range, which means there is variation in samples. Besides, Figure 6.6(b) shows that to get a RT σ_{total} larger than 2×10^{-4} S/cm, a relative density larger than 75% is needed.

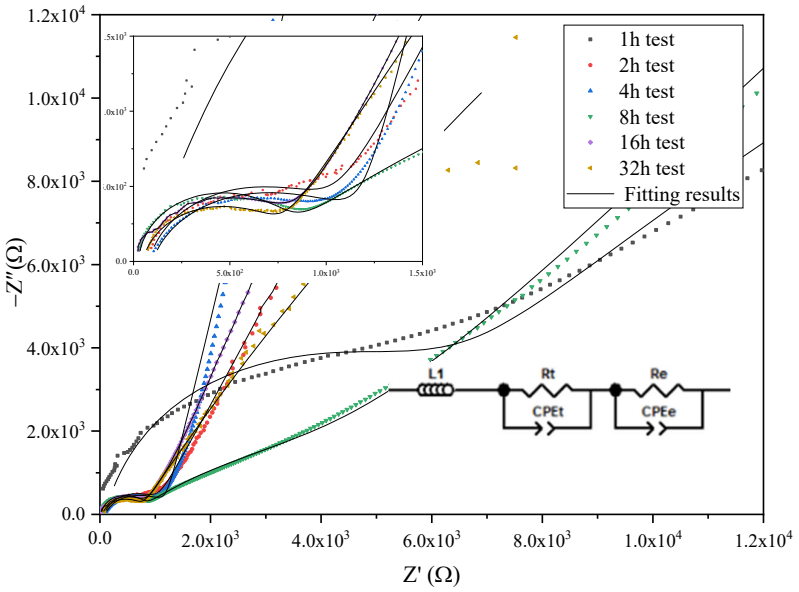

Figure 6.5 RT impedance spectra of LLZTO pellets prepared with $Zr(OH)_4$ salt and sintered at 1100°C for different sintering time. Data were fitted using the presented equivalent circuit of $L(R_tCPE_t)(R_eCPE_e)$

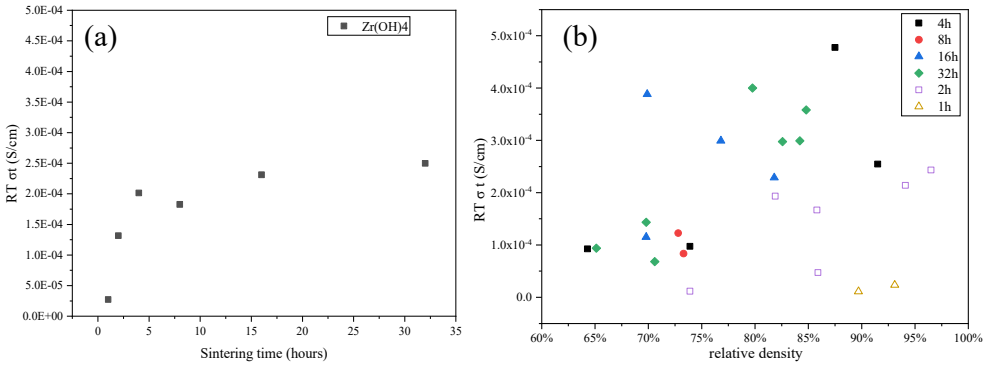

Figure 6.6 (a) Average RT total Li-ion conductivities of LLZTO prepared with $Zr(OH)_4$ salt and sintered at 1100°C for different sintering times, (b) The RT total Li-ion conductivities of LLZTO prepared with $Zr(OH)_4$ salt and sintered for different sintering times at different relative densities

The activation energy range of LLZTO samples sintered for different sintering time is listed in Table 6.2. Arrhenius plot of total Li-ion conductivities for LLZTO samples (for one sintering time, the sample which has a RT total σ_{Li^+} close to the average value was selected) are shown in Figure 6.7. The impedance spectra are shown in Appendix VII. The activation energy of LLZTO sample sintered for 1 hour is a little larger than others. LLZTO samples sintered for 2-32 hours have similar activation energy in the range of 0.23-0.30 eV, which is also shown in Table 6.2.

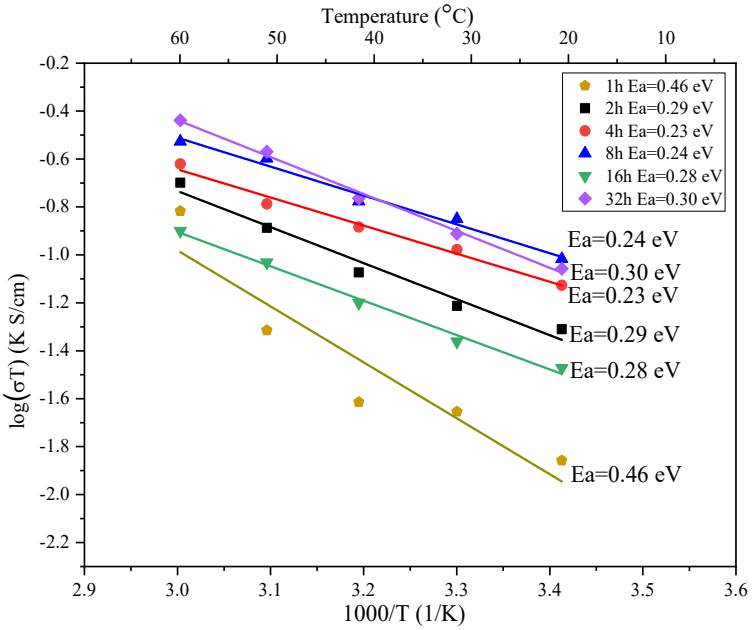

Figure 6.7 Arrhenius plot of total Li-ion conductivities for LLZTO pellets prepared with $Zr(OH)_4$ salt and sintered at 1100°C for different sintering time

The relative density and the corresponding diameter are plotted in Figure 6.8. The relative density decreased with the increasing diameter and be used to quickly identify samples with higher density. Figure 6.8 indicates that a 9 mm diameter corresponds to a relative density higher than 75% and a RT total σ_{Li^+} larger than 2×10^{-4} S/cm.

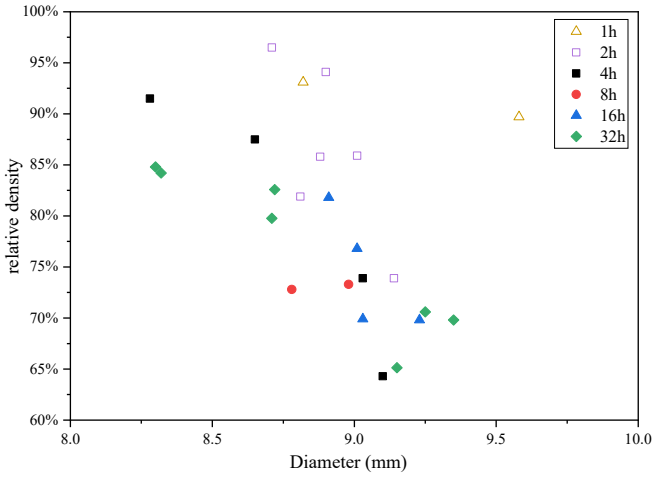

Figure 6.8 The relative density and the corresponding diameter for LLZTO prepared with $Zr(OH)_4$ salt and sintered at 1100°C for different sintering time

6.4 Difference between LLZTO prepared with two different Zr salts

The average relative density and the average RT total σ_{Li+} at different sintering time for LLZTO prepared by two different Zr sources are listed in Table 6.3 and plotted in Figure 6.9(a)(b). In Figure 6.9(a), when $ZrOCl_2*8H_2O$ is used, 8 hours is needed to obtain a relative density higher than 70%. While when $Zr(OH)_4$ salt is used, the relative densities for all sintering hours are higher than 70%. However, when the sintering time is 8 hours or longer, LLZTO prepared with $ZrOCl_2*8H_2O$ has a higher relative density than these prepared by $Zr(OH)_4$ salt, which resulted in a higher RT total σ_{Li+} in Figure 6.9(b). Although Cl was not necessary in the densification as discussed in Section 6.2, using Cl-containing salt could slightly improve the relative density which resulted in an average RT σ_{total} around 3.4×10^{-4} S/cm (2.3×10^{-4} S/cm for LLZTO prepared by no

Cl-containing salt, sintered for 16 hours), which are shown in Table 6.3.

Table 6.3 The average relative density, average RT total σ_{Li+}, at different sintering times for LLZTO prepared by two different Zr salts

Sintering time (hours)	$Zr(OH)_4$		$ZrOCl_2*8H_2O$	
	Relative density (mean ± SD)	RT total σ_{Li+} (mean ± SD)	Relative density (mean ± SD)	RT total σ_{Li+} (mean ± SD)
1	80±14	$(2.74±0.2) \times 10^{-5}$	-	-
2	79±8	$(1.32±0.9) \times 10^{-4}$	-	-
4	83±9	$(2.01±0.7) \times 10^{-4}$	61±9	$(5.7±2) \times 10^{-5}$
8	74±3	$(1.83±0.9) \times 10^{-4}$	82±3	$(4.3±0.8) \times 10^{-4}$
16	75±5	$(2.31±0.9) \times 10^{-4}$	90±1	$(3.4±1) \times 10^{-4}$
32	76±8	$(2.50±1.1) \times 10^{-4}$	90±1	$(3.1±1) \times 10^{-4}$

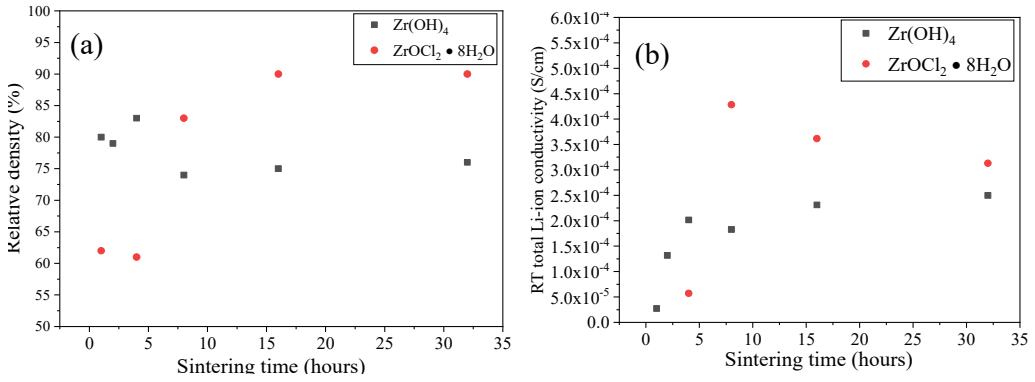

Figure 6.9 (a) The average relative density, (b) the average RT total σ_{Li+}, at different sintering time for LLZTO prepared by two different Zr salts

6.5 Conclusion

Chlorine is not necessary for the densification of LLZTO. LLZTO prepared with $Zr(OH)_4$ has a relative density of ~75%, which is smaller than that of ~90% for LLZTO prepared with $ZrOCl_2*8H_2O$ salt. Because of the lower relative density, LLZTO prepared with $Zr(OH)_4$ has a smaller Li-ion conductivity than that prepared with $ZrOCl_2*8H_2O$ salt. Therefore, although Cl is not necessary in the densification, using Cl-containing salt could slightly improve the relative density (RT total σ_{Li+} of 4.4×10^{-4} S/cm for LLZTO prepared by $ZrOCl_2*8H_2O$ and 3.2×10^{-4} S/cm for LLZTO prepared by $Zr(OH)_4$).

Chapter 7. LLZTO-PEO($LiClO_4$) composites

In this chapter, LLZTO based composites of LLZTO-PEO($LiClO_4$) with a continuous LLZTO ceramic body were prepared and characterized. The schematic of the LLZTO-PEO($LiClO_4$) composite is shown in Figure 7.1. The properties of porous LLZTO, which is sintered at 1100°C for 16 hours, could be found in Chapter 4.

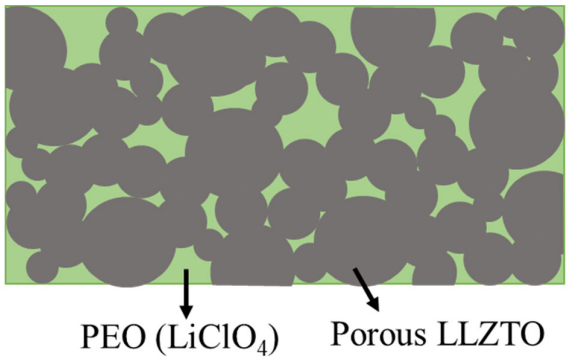

Figure 7.1 Schematic of LLZTO-PEO($LiClO_4$) composite with a continuous LLZTO ceramic body

7.1 LLZTO-PEO($LiClO_4$) composites prepared by the multi-time dip process

SEM images of the cross-section area of LLZTO-PEO($LiClO_4$) prepared by the multi-time dip process are shown in Figure 7.2. The samples are almost dense and have only a few pores in the cross-section area. Cracks were found in the polymer, which may have formed when the sample was broken to prepare samples for observing the cross-section area.

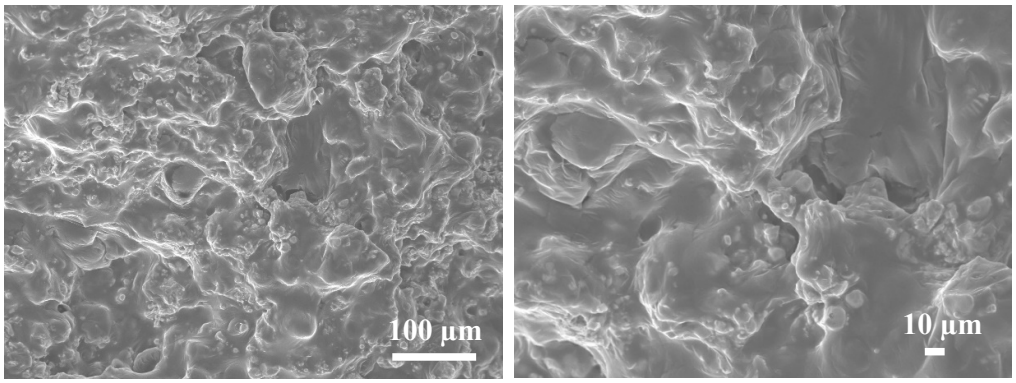

Figure 7.2 SEM images of the cross-section area of LLZTO-PEO($LiClO_4$) composite prepared by the multi-time dip process

The measured conductivity of LLZTO-PEO($LiClO_4$) composite prepared by the multi-time dip process is shown in Figure 7.3. Figure 7.3(a) shows an example of a typical Nyquist plot. The experimental data were fitted with an equivalent circuit consisting of (R_bCPE_b)($R_{gb}CPE_{gb}$)(CPE_e). The first semicircle at high frequency is attributed to the bulk electrolyte resistance (R_b), and the second semicircle is attributed to the grain boundary resistance (R_{gb}), which is similar to the literature [125–127]. The total resistance can be calculated as $R_{total} = (R_g + R_{gb})$. For LLZTO-PEO($LiClO_4$) composite prepared by the multi-time dip process, the room temperature total conductivity is 7.2×10^{-7} S/cm. The activation energy estimated from the slope of the log(σT) versus 1000/T in Figure 7.3(b) is 0.60 eV for bulk and 0.52 eV for grain boundary. The LLZTO-PEO($LiClO_4$) composite has a lower total Li-ion conductivity

compared to LLZTO, which may result from the low ionic conductivity of 1×10^{-7} S/cm of the solid polymer electrolyte of PEO($LiClO_4$) [4]. The other possible reason for the low total Li-ion conductivity may be the long-time exposure to the air during the multi-time dip process, as the structure of PEO($LiClO_4$) could be greatly affected by the humidity which is due to the interactions of water with lithium salt of ($LiClO_4$) [128].

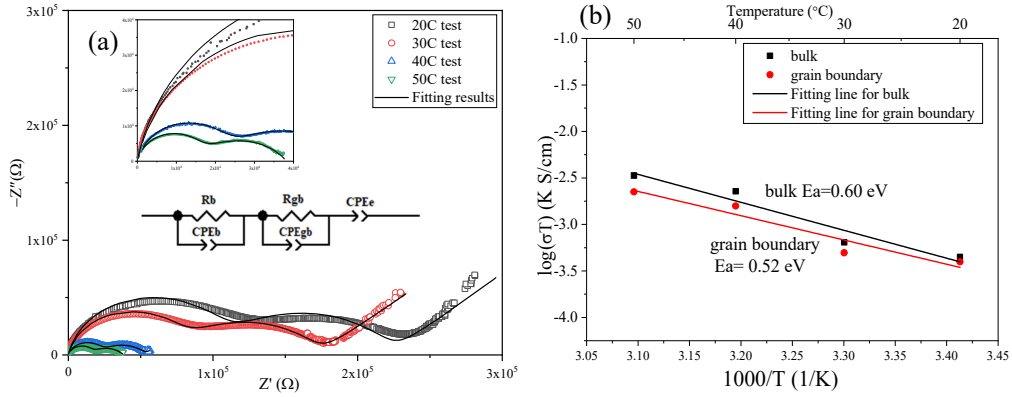

Figure 7.3 Ionic conductivity data of LLZTO-PEO($LiClO_4$) composite prepared by the multi-time dip process, (a) room temperature impedance spectra, (b) Arrhenius plot, data were fitted using the presented equivalent circuit of (R_bCPE_b)($R_{gb}CPE_{gb}$)(CPE_e)

7.2 LLZTO-PEO($LiClO_4$) composites prepared by the one-time dip process

SEM images of the cross-section area of LLZTO-PEO($LiClO_4$) composite prepared by the one-time dip process are shown in Figure 7.4. The LLZTO-PEO($LiClO_4$) composite is also found to be denser than the LLZTO. Compared to the

SEM images of Figure 7.2, LLZTO-PEO($LiClO_4$) composite prepared by the multi-time dip process is denser than this prepared by the one-time dip process.

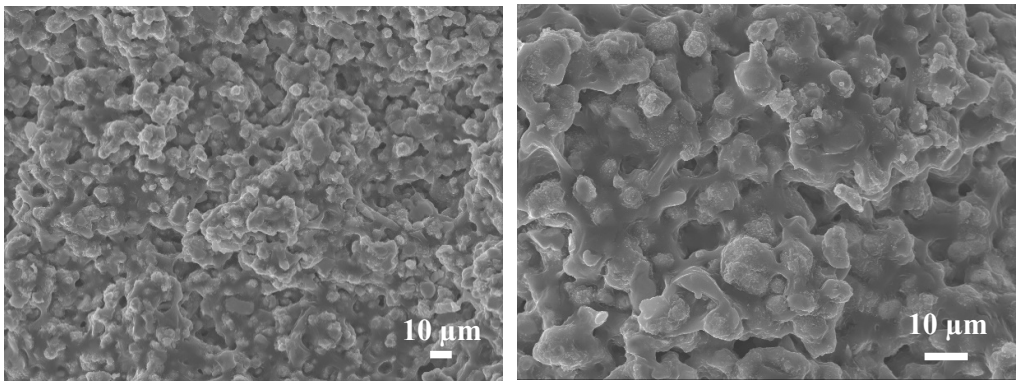

Figure 7.4 SEM images of the cross-section area of LLZTO-PEO($LiClO_4$) composite prepared by the one-time dip process

The measured conductivity of LLZTO-PEO($LiClO_4$) composite prepared by the one-time dip process is shown in Figure 7.5. The Nyquist plots show one semicircle in the high range and a low frequency tail, which is different from that prepared by multi-time dip process. The experimental data were fitted with an equivalent circuit consisting of (R_tCPE_t)(CPE_e). In this sample, the bulk and grain boundary contributions cannot be separated, which is consistent with other works [43,55]. Besides, this also indicates that the long-time exposure to the air will greatly increase the grain boundary contribution as shown in the results of that prepared by the one-time dip process. The room temperature total conductivity is 1.15×10^{-6} S/cm, which is larger than that prepared

by multi-time dip process of 7.2×10^{-7} S/cm. The activation energy estimated from the slope of the log(σT) versus 1000/T in Figure 7.5(b) is 0.58 eV for total, which is similar to that prepared by the multi-time dip process.

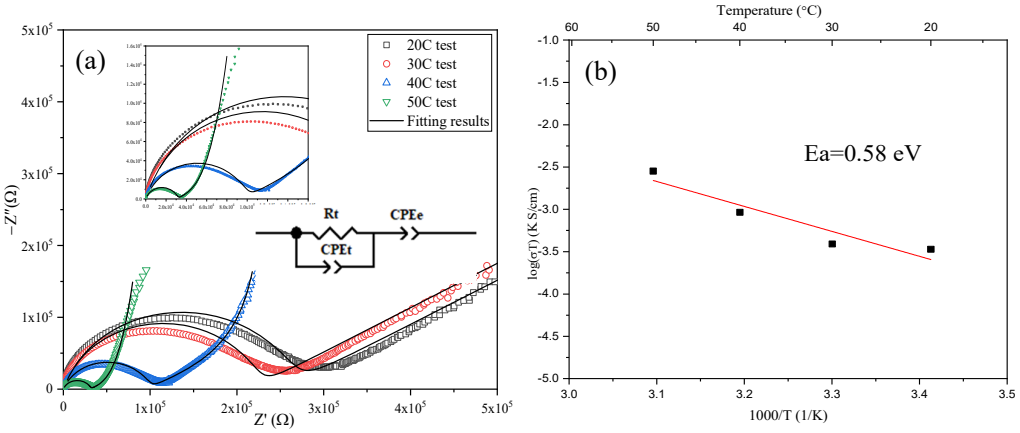

Figure 7.5 Ionic conductivity data of LLZTO-PEO($LiClO_4$) composite prepared by the one-time dip process, (a) room temperature impedance spectra, (b) Arrhenius plot, data were fitted using the presented equivalent circuit of (R_tCPE_t)(CPE_e)

Total conductivity and activation energy of LLZTO and LLZTO-PEO($LiClO_4$) composite are shown in Table 7.1. The room temperature total Li-ion conductivity of LLZTO-PEO($LiClO_4$) composite prepared by one-time dip of 1.15×10^{-6} S/cm is larger than that prepared by multi-time dip process of 7.2×10^{-7} S/cm. The exposure to the air during the multi-time dip is the reason for the lower conductivity, as PEO($LiClO_4$) is sensitive to moisture [101,128–130]. The structure of PEO($LiClO_4$) could be greatly affected by the humidity which is due to the interactions of water with lithium salt of ($LiClO_4$) [128]. Dense LLZTO-based composite did not show better electrical

properties than LLZTO samples. One possible reason could be the synthesis of this composite, as the sample were exposed to the air several times during the multi-dip process. The EIS measurement performed in the air may be another possible reason for the low conductivity of LLZTO-PEO($LiClO_4$) composite.

Table 7.1 Conductivity and activation energy of LLZTO and LLZTO-PEO($LiClO_4$) composite

	LLZTO	PEO($LiClO_4$)	LLZTO-PEO($LiClO_4$) composite	
			multi-time dip	one-time dip
Total conductivity (S/cm)	8.9×10^{-6}	1×10^{-7} [4]	7.2×10^{-7}	1.15×10^{-6}
Activation energy (eV)	0.37	-	0.60 bulk	0.58
			0.52 grain boundary	

7.3 Conclusion

Dense LLZTO-PEO($LiClO_4$) composites have been prepared by both multi-time dip and one-time dip process. But the Li-ion conductivities of the composites are very low, which may due to the exposure to the air during both sample preparation and EIS tests.

8. Conclusions

The cubic phase structure has been stabilized by doing elements of Al and Ta. However, both Al-doped and Ta-doped LLZO are porous (~60% for Ta-doped LLZO), and thereby resulting in a low Li-ion conductivity, which is smaller than 2×10^{-5} S/cm. For both undoped and Ta-doped LLZO, aluminum was detected by ICP. The concentration of Al is low (0.04 - 0.07 mole pfu) and is presumably from Al_2O_3 crucible.

Using a simple co-precipitation method with cold uniaxial pressing and sintering in a lithium-rich air atmosphere, which was created by the addition of LiOH to the LLZTO cover powder, the densification of LLZTO pellets was observed. A relative density of 92% was obtained, which resulted in a high Li-ion conductivity of 4.6×10^{-4} S/cm. Compared to other high-cost techniques used for densification, this work introduces a simple co-precipitation method with cold uniaxial pressing and sintering in air for the densification. The 15Li + LiOH cover powder results in the formation of an Al-containing interparticle phase, which facilitates the densification of LLZTO. The aluminum concentration increases during sintering and is located in the grain boundary. The increased aluminum content promoted phase stabilization and densification, but the Al-containing phase also limits LLZTO phase continuity.

The element of chlorine was detected in the interparticle phase for 65Li sintered at 1100°C for 1 and 2 hours, which presumably comes from the starting material of $ZrOCl_2\cdot8H_2O$. Chlorine was not necessary for the densification as the densification was

also observed in LLZTO pellets prepared with no Cl-containing salts. However, using Cl-containing salt could slightly improve the relative density (~90% vs ~75%) and thereby resulting in a slightly higher Li-ion conductivity (RT total σ_{Li+} of 3.4×10^{-4} S/cm for LLZTO prepared by $ZrOCl_2*8H_2O$ and 2.3×10^{-4} S/cm for LLZTO prepared by $Zr(OH)_4$).

The tetrahedral and octahedral Li site occupancy in the cubic phase garnet structure with a high Li concentration affect the lithium-ion conductivity. As the lithium content increases, the portion of lithium occupying the 96h octahedral site increases, which due to the higher mobility of these sites, and leads to an increase in the Li-ion conductivity. There appears to be a limit to this increase as the conductivity for occupancies greater than 90% is lower which may be due to the decrease in the vacancy concentration.

Dense LLZTO-PEO($LiClO_4$) composites have been prepared by both multi-time dip and one-time dip process. But the Li-ion conductivities of the composites are very low, which may due to the exposure to the air during both sample preparation and EIS tests. PEO($LiClO_4$) is sensitive to moisture [101,128–130], and the structure could be greatly affected by the humidity which is due to the interactions of water with lithium salt of ($LiClO_4$) [128].

9. Future work

In the densification of Ta-doped LLZO ($Li_{6.75}La_3Zr_{1.75}Ta_{0.25}O_{12}$) pellet, the 15Li + LiOH cover powder results in the formation of an Al-containing interparticle phase, which facilitate the densification of LLZTO. However, with the same experiment settings, the densification of Al-doped LLZO pellets did not occur. In addition, the pure cubic phase structure could not be obtained, which are shown in Appendix VIII. It would be helpful to understand the factors which are in charge of the formation of the Al-containing interparticle phases and eventually densify the sample.

The suggested experiments will be the fabrication of LLZO with dual doping of Al and Ta. Different sintering parameters and different cover powders of 15Li and 15Li + LiOH will be studied. Using the same Ta doping level of 0.25 mol.% and the same sintering parameter of 1100°C for 16h, by changing the doping level of Al, the effect of Al on the densification of LLZO will be studied. It is reported by Allen et al. [38] that the addition of Al into Ta-doped LLZO ($Li_{6.15}Al_{0.2}La_3Zr_{1.75}Ta_{0.25}O_{12}$) lead to a decrease in the ionic conductivity from 8.7×10^{-4} S/cm to 3.7×10^{-4} S/cm. Therefore, in the experiment, a smaller Al doping level of 0.05-0.2 mol% will be tried.

Another type of LLZO with dual doping of Al and Ta would be with the same Al doping level of 0.24 mol.%, which has been studied in this work, but a small Ta doping level of 0.05 mol.%. This experiment will be helpful to determine if the Ta at Zr site help with the formation of Al-containing interparticle phases.

Li-ion conductivity of both Al-doped and Ta-doped LLZO has been studied in the temperature range of 20-160°C and 20-100°C, respectively. The future study on the Li-ion conductivities at lower temperature of -100 - 20°C or higher temperature of 100 - 250°C will help with the understanding of Li conducting behavior at different temperatures. At the same time, the Li occupancy study on the corresponding samples of will be helpful in understanding the Li transport, as there are limited works on the Li site occupancy at different temperatures.

As the LLZTO-PEO($LiClO_4$) composites prepared in this work has a low Li-ion conductivity of 1.15×10^{-6} S/cm, which is much smaller than reported works [98–100], it would be the interest to figure out a better processing for obtaining a LLZTO-PEO($LiClO_4$) composite with a higher Li-ion conductivity. The composite will be fabricated by dipping the porous LLZO pellet in the PEO($LiClO_4$), will be performed inside a glove box.

9. Appendices

Appendix I. The needed modified alumina crucible for the densification of LLZTO

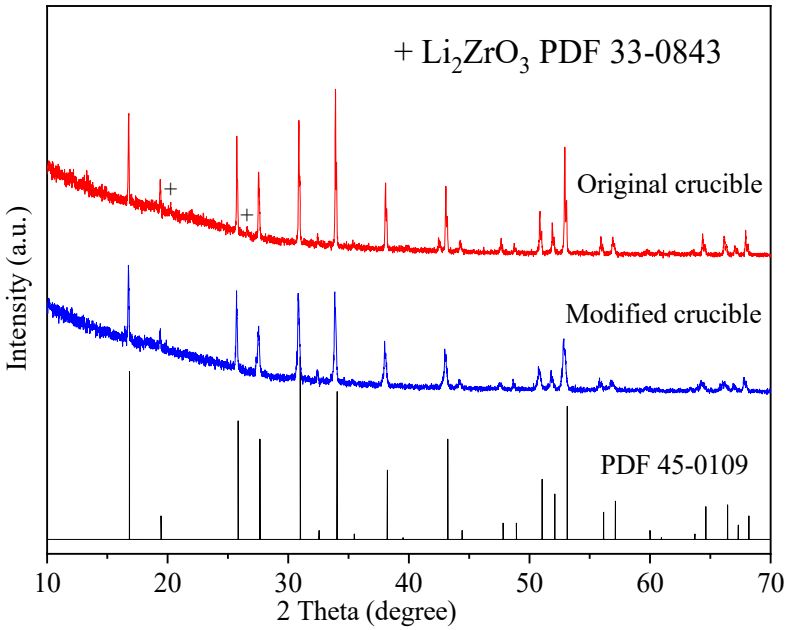

XRD patterns of 65Li sintered at 1100°C for 16 hours with cover powder of 15Li + LiOH in original and modified alumina crucible

The XRD patterns of 65Li samples sintered at 1100°C for 16 hours covered with the same cover powder of 15Li + LiOH are shown in above figure. A pure cubic garnet phase was obtained when the modified alumina crucible was used. Li_2ZrO_3 phase was observed in addition to the cubic garnet phase, when the original crucible was used, indicating that there was excess Li content. The notches on the sides were found to be necessary to allow an optimal amount of gas exchange between inside of the crucible and surrounding atmosphere.

Appendix II. The impedance spectra used in Figure 5.8

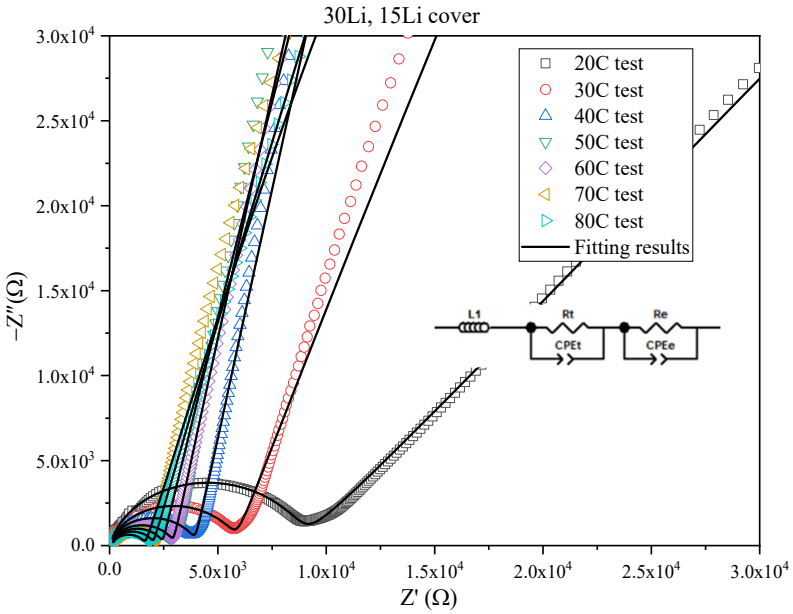

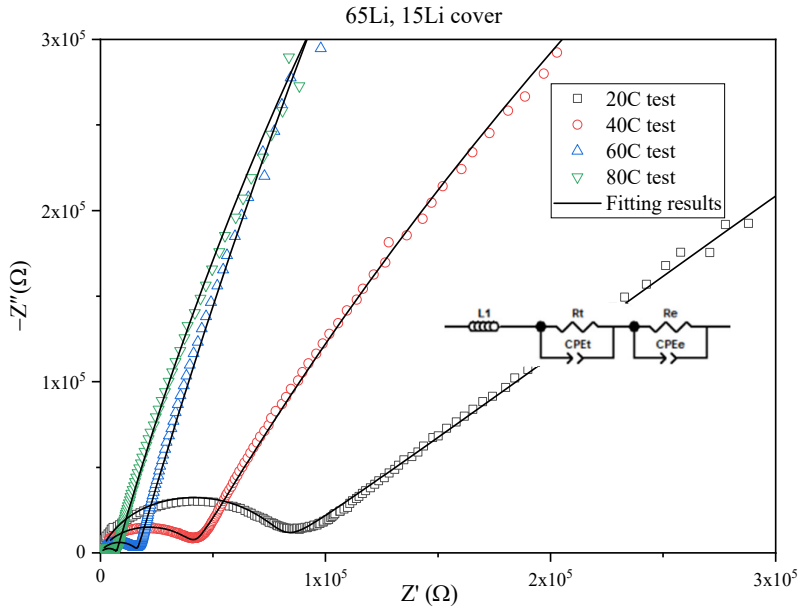

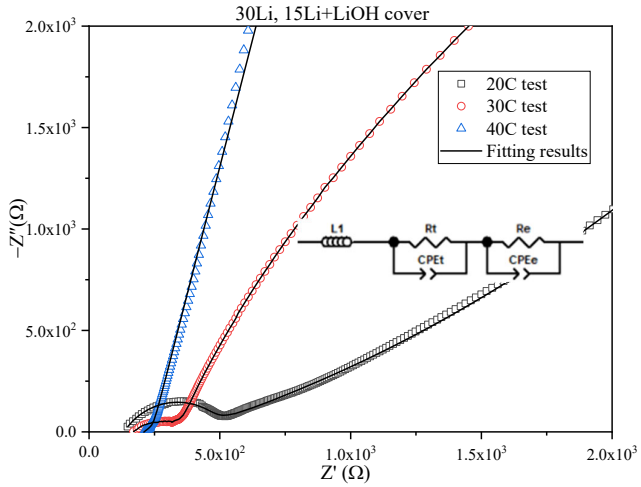
30Li, 15Li+LiOH cover
20C test
30C test
40C test
Fitting results
L1
Rt
Re
CPEt
CPEe
−Z''(Ω)
Z' (Ω)
0.0
5.0x10²
1.0x10³
1.5x10³
2.0x10³

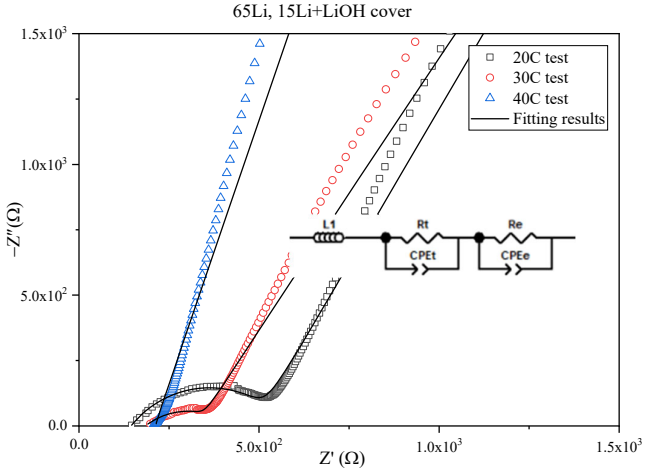
65Li, 15Li+LiOH cover
20C test
30C test
40C test
Fitting results
L1
Rt
Re
CPEt
CPEe
−Z''(Ω)
Z' (Ω)
0.0
5.0x10²
1.0x10³
1.5x10³

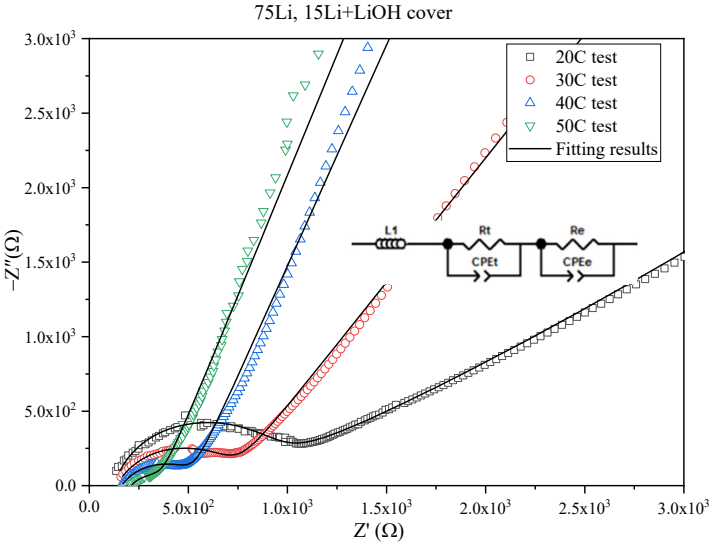
75Li, 15Li+LiOH cover
20C test
30C test
40C test
50C test
Fitting results
L1
Rt
Re
CPEt
CPEe
−Z''(Ω)
Z' (Ω)
0.0
5.0x10²
1.0x10³
1.5x10³
2.0x10³
2.5x10³
3.0x10³

Appendix III. Atomic probe tomography (APT) results

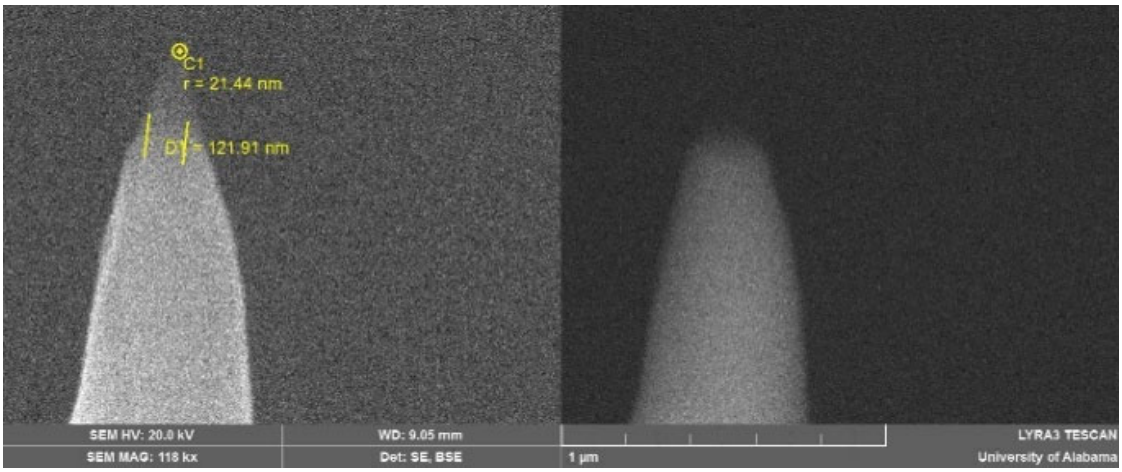

SEM image of the tip prepared by FIB and used for APT

Appendix IV. Laser ablation inductively coupled plasma mass spectrometry (LA-ICPMS) results

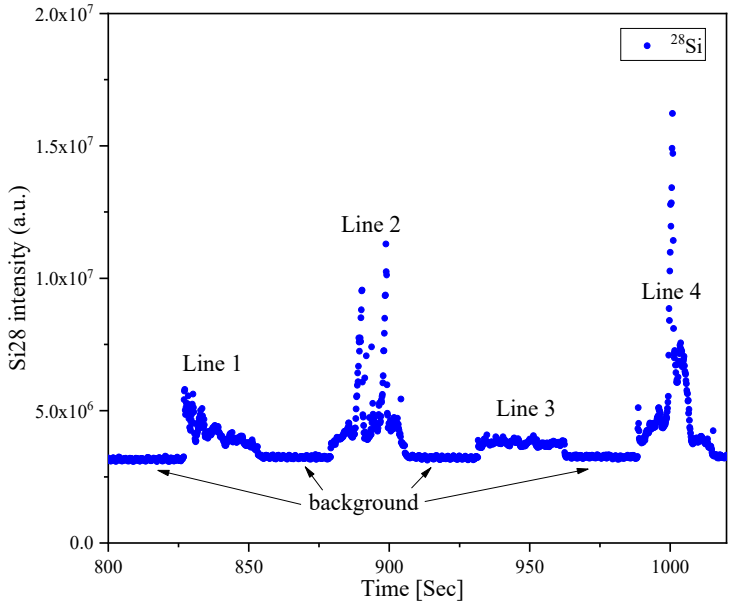

Appendix V. The table of the RT total Li-ion conductivities of 65Li pellets sintered for 4 to 32 hours

Table. RT total Li-ion conductivities of 65Li sintered at 1100°C for different sintering time of 4, 8, 16, and 32 hours with the cover powder of 15Li + LiOH

Sintering time (hours)	RT total σ_{Li+} (S/cm)	Average RT total σ_{Li+} (S/cm)
4	3.22×10^{-5}	5.70×10^{-5}
	4.70×10^{-5}	
	6.66×10^{-5}	
	8.23×10^{-5}	
8	3.53×10^{-4}	4.28×10^{-4}
	4.29×10^{-4}	
	5.04×10^{-4}	
16	1.91×10^{-4}	3.37×10^{-4}
	2.25×10^{-4}	
	2.61×10^{-4}	
	3.27×10^{-4}	
	4.47×10^{-4}	
	4.51×10^{-4}	
	4.59×10^{-4}	
32	1.70×10^{-4}	3.13×10^{-4}
	1.86×10^{-4}	
	1.98×10^{-4}	
	3.35×10^{-4}	
	3.75×10^{-4}	
	3.82×10^{-4}	
	5.46×10^{-4}	

Appendix VI. EDS results of $Li_{6.75}La_3Zr_{1.75}Ta_{0.25}O_{12}$ prepared with $Zr(OH)_4$ and sintered at 1100°C for different times

1 hour

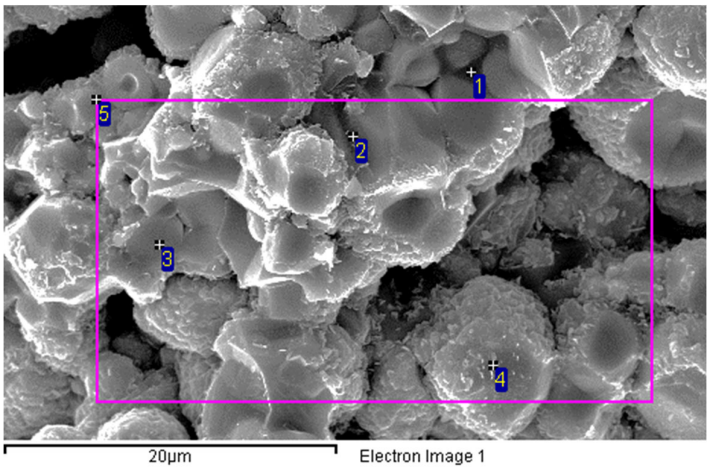

Spectrum	Al	Zr	La	Ta
1	19	0	81	0
2	55	13	28	4
3	17	0	83	0
4	0	36	56	8
5	23	23	48	6

2 hours

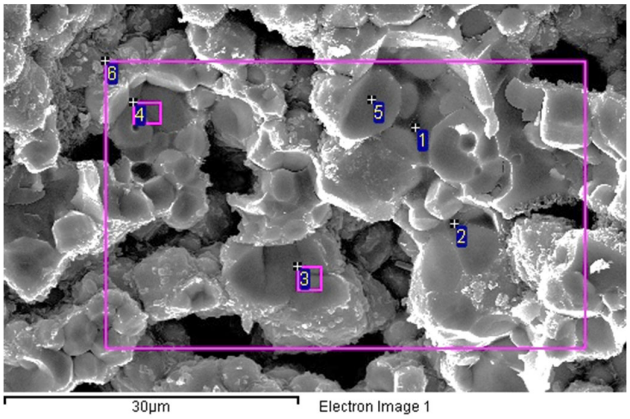

Spectrum	Al	Zr	La	Ta
1	40	13	44	3
2	43	8	47	3
3	0	34	58	8
4	0	23	70	7
5	0	36	52	11
6	10	28	54	8

4 hours

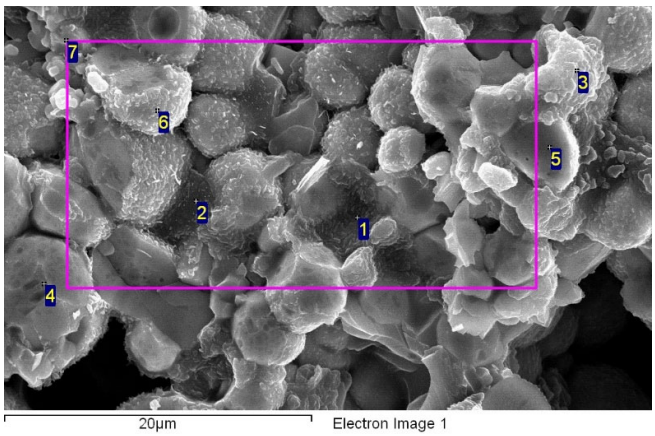

Spectrum	O	Al	Si	Zr	La	Ta
1	76	15	0	3	5	1
2	76	14	0	5	5	0
3	82	5	0	11	2	0
4	63	0	5	11	20	1
5	86	9	0	3	1	0
6	77	1	0	8	12	2
7	80	4	0	7	8	1

8 hours

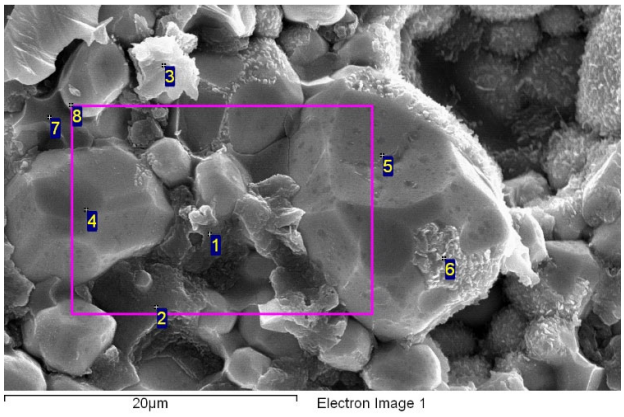

Spectrum	O	Al	Si	Zr	La	Ta
1	82	12	1	2	3	0
2	75	23	0	2	1	0
3	82	11	0	3	4	0
4	25	3	0	19	53	0
5	29	0	0	17	55	0
6	38	0	7	21	35	0
7	43	0	0	53	2	2
8	69	5	0	9	16	2

32 hours

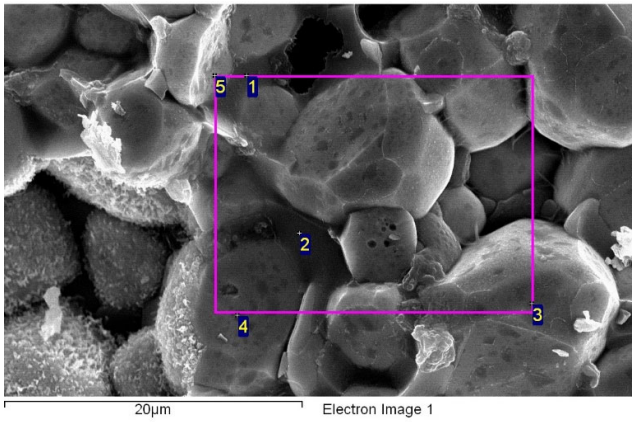

Spectrum	O	Al	Si	Zr	La	Ta
1	67	11	0	6	17	0
2	72	25	0	1	2	0
3	49	0	0	18	28	4
4	60	2	3	13	21	3
5	68	9	3	7	11	1

EDS results of $Li_{6.75}La_3Zr_{1.75}Ta_{0.25}O_{12}$ prepared with different Zr salts and sintered at 1100°C for different hours, all results are in atomic%

Appendix VII. The impedance spectra used in Figure 6.7

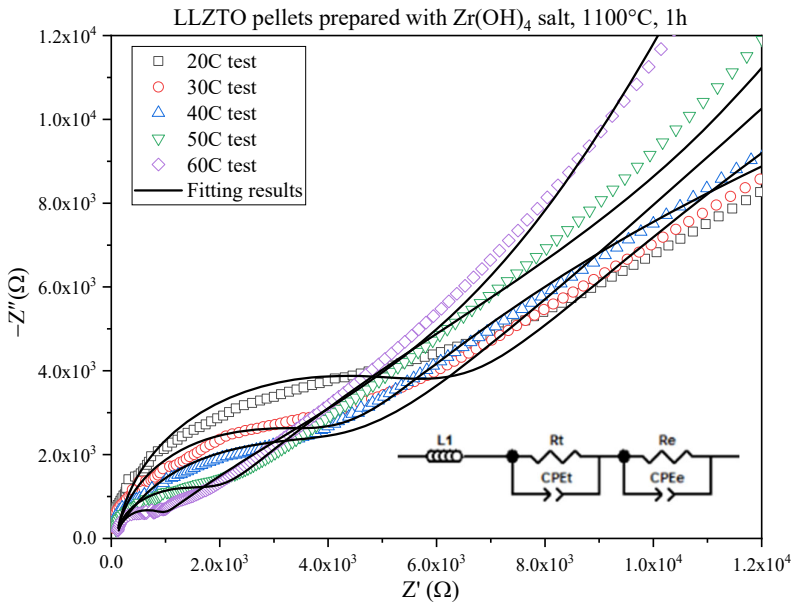

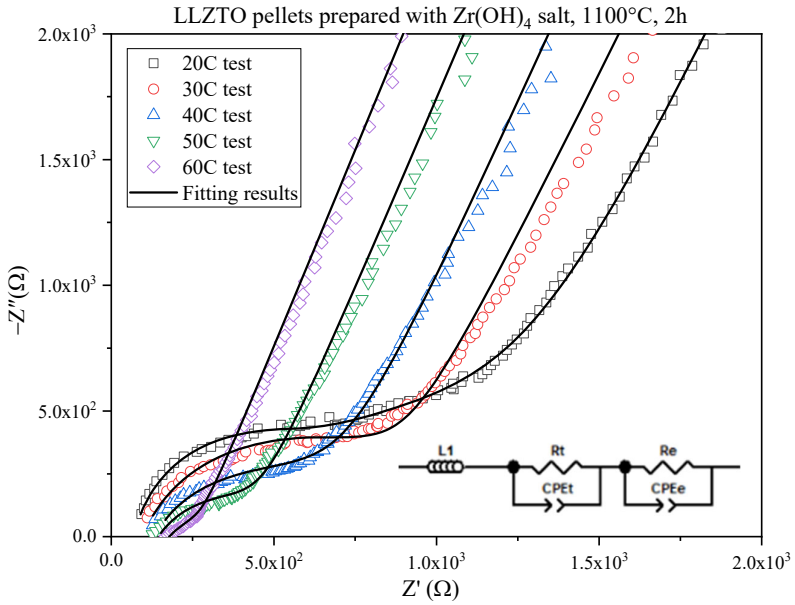

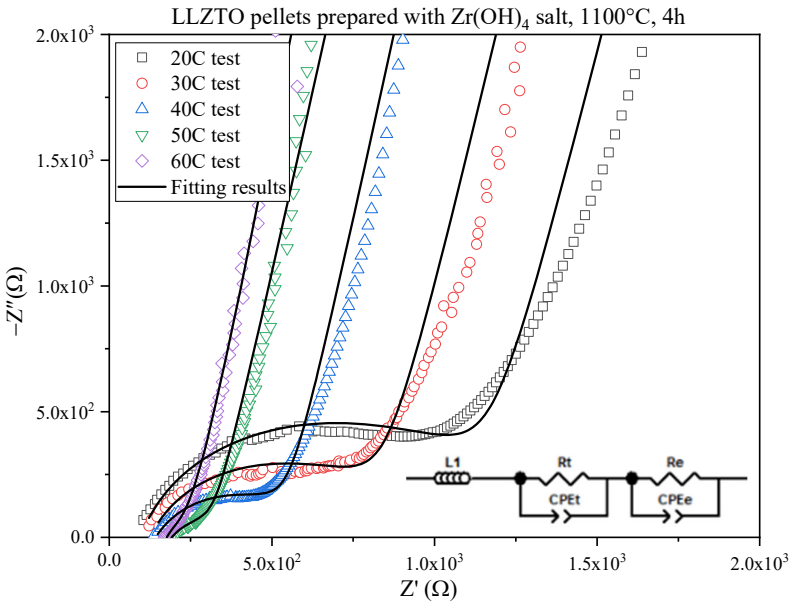
LLZTO pellets prepared with Zr(OH)4 salt, 1100°C, 4h
20C test
30C test
40C test
50C test
60C test
Fitting results
L1
Rt
CPEt
Re
CPEe
−Z''(Ω)
Z' (Ω)
0.0
5.0x10^2
1.0x10^3
1.5x10^3
2.0x10^3

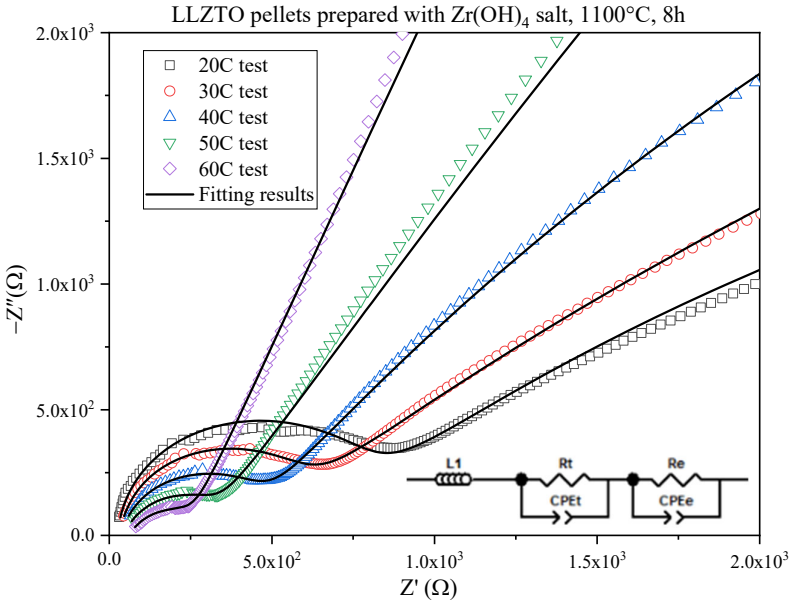
LLZTO pellets prepared with Zr(OH)4 salt, 1100°C, 8h
20C test
30C test
40C test
50C test
60C test
Fitting results
L1
Rt
CPEt
Re
CPEe
−Z''(Ω)
Z' (Ω)
0.0
5.0x10^2
1.0x10^3
1.5x10^3
2.0x10^3

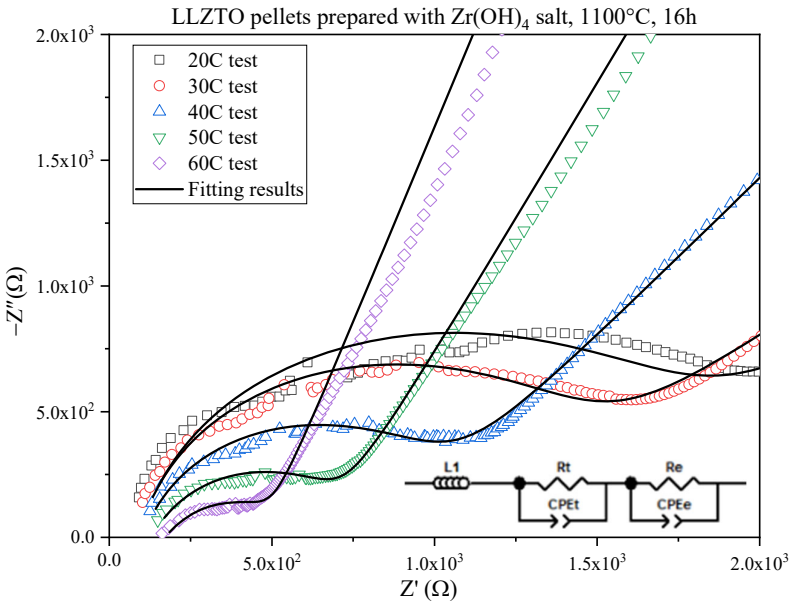
LLZTO pellets prepared with Zr(OH)4 salt, 1100°C, 16h
20C test
30C test
40C test
50C test
60C test
Fitting results
L1
Rt
Re
CPEt
CPEe
−Z'' (Ω)
Z' (Ω)
0.0
5.0x10^2
1.0x10^3
1.5x10^3
2.0x10^3

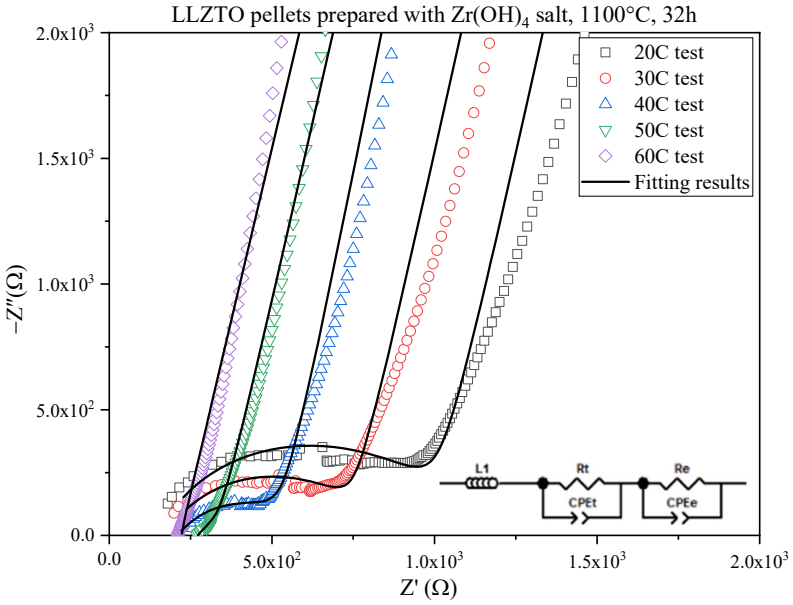
LLZTO pellets prepared with Zr(OH)4 salt, 1100°C, 32h
20C test
30C test
40C test
50C test
60C test
Fitting results
L1
Rt
Re
CPEt
CPEe
−Z'' (Ω)
Z' (Ω)
0.0
5.0x10^2
1.0x10^3
1.5x10^3
2.0x10^3

Appendix VIII. The XRD results of Al-doped LLZO prepared with PVA and 15Li + LiOH cover powders

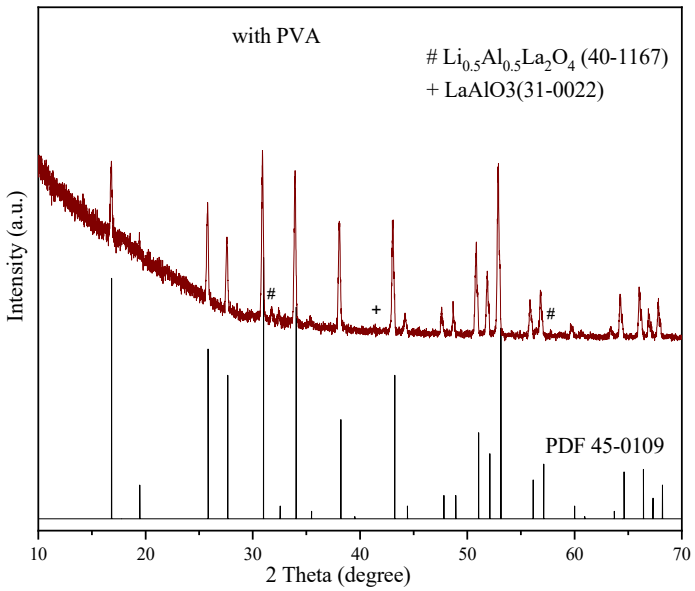

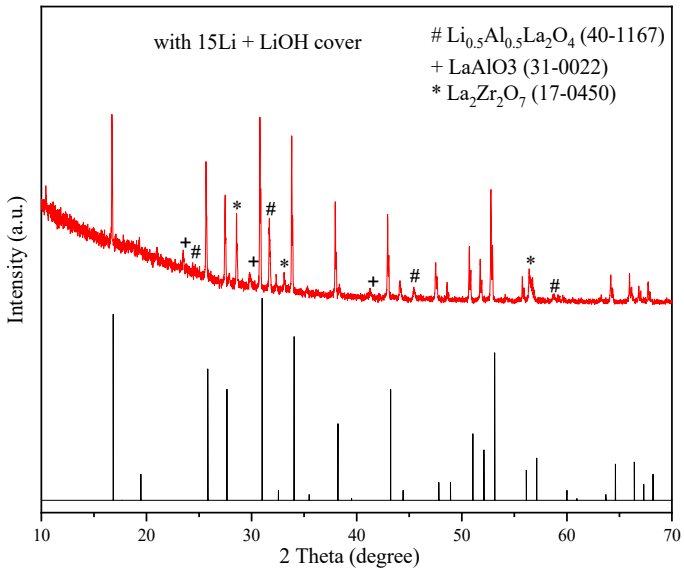

With the addition of PVA, a common additive used to densify ceramics, Al-doped LLZO ($Li_{6.28}Al_{0.24}La_3Zr_2O_{12}$) pellets were still porous. Two additional phases of $Li_{0.5}Al_{0.5}La_2O_4$ and $LaAlO_3$ phases were observed in XRD results. With cover powder

of 15Li + LiOH, Al-doped LLZO pellets were not densified. Three additional phases of $Li_{0.5}Al_{0.5}La_2O_4$, $LaAlO_3$ and $La_2Zr_2O_7$ phases were observed.

Reference

[1] R. Sudo, Y. Nakata, K. Ishiguro, M. Matsui, A. Hirano, Y. Takeda, O. Yamamoto, N. Imanishi, Interface behavior between garnet-type lithium-conducting solid electrolyte and lithium metal, Solid State Ionics. 262 (2014) 151–154.

[2] C.A. Geiger, E. Alekseev, B. Lazic, M. Fisch, T. Armbruster, R. Langner, M. Fechtelkord, N. Kim, T. Pettke, W. Weppner, Crystal chemistry and stability of "$Li_7La_3Zr_2O_{12}$" garnet: A fast lithium-ion conductor, Inorg. Chem. 50 (2011) 1089–1097.

[3] A. Manthiram, X. Yu, S. Wang, Lithium battery chemistries enabled by solid-state electrolytes, Nat. Rev. Mater. 2 (2017) 16103.

[4] R.C. Agrawal, G.P. Pandey, Solid polymer electrolytes: Materials designing and all-solid-state battery applications: An overview, J. Phys. D. Appl. Phys. 41 (2008) 223001–18.

[5] H. Zhang, C. Li, M. Piszcz, E. Coya, T. Rojo, L.M. Rodriguez-Martinez, M. Armand, Z. Zhou, Single lithium-ion conducting solid polymer electrolytes: advances and perspectives, Chem. Soc. Rev. 46 (2017) 797–815.

[6] Y. Zhao, C. Wu, G. Peng, X. Chen, X. Yao, Y. Bai, F. Wu, S. Chen, X. Xu, A new solid polymer electrolyte incorporating $Li_{10}GeP_2S_{12}$ into a polyethylene oxide matrix for all-solid-state lithium batteries, J. Power Sources. 301 (2016) 47–53.

[7] Y. Ren, K. Chen, R. Chen, T. Liu, Y. Zhang, C.W. Nan, Oxide Electrolytes for

Lithium Batteries, J. Am. Ceram. Soc. 98 (2015) 3603–3623.

[8] E. Quartarone, P. Mustarelli, Electrolytes for solid-state lithium rechargeable batteries: Recent advances and perspectives, Chem. Soc. Rev. 40 (2011) 2525–2540.

[9] C. Wang, Y. Yang, X. Liu, H. Zhong, H. Xu, Z. Xu, H. Shao, F. Ding, Suppression of Lithium Dendrite Formation by Using LAGP-PEO (LiTFSI) Composite Solid Electrolyte and Lithium Metal Anode Modified by PEO (LiTFSI) in All-Solid-State Lithium Batteries, ACS Appl. Mater. Interfaces. 9 (2017) 13694–13702.

[10] D. Aurbach, Y. Talyosef, B. Markovsky, E. Markevich, E. Zinigrad, L. Asraf, J.S. Gnanaraj, H.J. Kim, Design of electrolyte solutions for Li and Li-ion batteries: A review, in: Electrochim. Acta, Pergamon, 2004: pp. 247–254.

[11] B.K. Money, J. Swenson, Dynamics of poly(ethylene oxide) around its melting temperature, Macromolecules. 46 (2013) 6949–6954.

[12] S. Das, A. Ghosh, Ionic conductivity and dielectric permittivity of PEO-$LiClO_4$ solid polymer electrolyte plasticized with propylene carbonate, AIP Adv. 5 (2015).

[13] S.U. Patil, S.S. Yawale, S.P. Yawale, Conductivity study of PEO-$LiClO_4$ polymer electrolyte doped with ZnO nanocomposite ceramic filler, Bull. Mater. Sci. 37 (2014) 1403–1409.

[14] A.M. Stephan, Review on gel polymer electrolytes for lithium batteries, Eur. Polym. J. 42 (2006) 21–42.

[15] M. Zhang, K. Takahashi, N. Imanishi, Y. Takeda, O. Yamamoto, B. Chi, J. Pu, J. Li, Preparation and Electrochemical Properties of $Li_{1+x}Al_xGe_{2-x}(PO_4)_3$ Synthesized by

a Sol-Gel Method, J. Electrochem. Soc. 159159 (2012) 1114–1119.

[16] T. Ohtomo, A. Hayashi, M. Tatsumisago, K. Kawamoto, Glass Electrolytes with High Ion Conductivity and High Chemical Stability in the System LiI-Li_2O-Li_2S-P_2S_5, Electrochemistry. 81 (2013) 428–431.

[17] N. Kamaya, K. Homma, Y. Yamakawa, M. Hirayama, R. Kanno, M. Yonemura, T. Kamiyama, Y. Kato, S. Hama, K. Kawamoto, A. Mitsui, A lithium superionic conductor, Nat. Mater. 10 (2011) 682–686.

[18] R. Murugan, V. Thangadurai, W. Weppner, Fast lithium ion conduction in garnet-type $Li_7La_3Zr_2O_{12}$, Angew. Chemie - Int. Ed. 46 (2007) 7778–7781.

[19] V. Thangadurai, H. Kaack, W.J.F. Weppner, Novel Fast Lithium Ion Conduction in Garnet-Type $Li_5La_3M_2O_{12}$, J. Am. Ceram. Soc. 40 (2003) 437–440.

[20] J.E. Ni, E.D. Case, J.S. Sakamoto, E. Rangasamy, J.B. Wolfenstine, Room temperature elastic moduli and Vickers hardness of hot-pressed LLZO cubic garnet, J. Mater. Sci. 47 (2012) 7978–7985.

[21] J. Awaka, N. Kijima, H. Hayakawa, J. Akimoto, Synthesis and structure analysis of tetragonal $Li_7La_3Zr_2O_{12}$ with the garnet-related type structure, J. Solid State Chem. 182 (2009) 2046–2052.

[22] J. Awaka, N. Kijima, Y. Takahashi, H. Hayakawa, J. Akimoto, Synthesis and crystallographic studies of garnet-related lithium-ion conductors $Li_6CaLa_2Ta_2O_{12}$ and $Li_6BaLa_2Ta_2O_{12}$, Solid State Ionics. 180 (2009) 602–606.

[23] N. Bernstein, M.D. Johannes, K. Hoang, Origin of the structural phase transition

in $Li_7La_3Zr_2O_{12}$ Phys. Rev. Lett. 109 (2012) 1–5.

[24] S. Teng, J. Tan, A. Tiwari, Recent developments in garnet based solid state electrolytes for thin film batteries, Curr. Opin. Solid State Mater. Sci. 18 (2014) 29–38.

[25] V. Thangadurai, S. Narayanan, D. Pinzaru, Garnet-type solid-state fast Li ion conductors for Li batteries: critical review., Chem. Soc. Rev. 43 (2014) 4714–27.

[26] J. Awaka, A. Takashima, K. Kataoka, N. Kijima, Y. Idemoto, J. Akimoto, Crystal Structure of Fast Lithium-ion-conducting Cubic $Li_7La_3Zr_2O_{12}$, Chem. Lett. 40 (2011) 60-62.

[27] K. Meier, T. Laino, A. Curioni, Solid-state electrolytes: Revealing the mechanisms of Li-Ion conduction in tetragonal and cubic LLZO by first-principles calculations, J. Phys. Chem. C. 118 (2014) 6668–6679.

[28 L.J. Miara, W.D. Richards, Y.E. Wang, G. Ceder, First-Principles Studies on Cation Dopants and Electrolyte|Cathode Interphases for Lithium Garnets, Chem. Mater. 27 (2015) 4040–4047.

[29] Y. Jin, P.J. McGinn, Al-doped $Li_7La_3Zr_2O_{12}$ synthesized by a polymerized complex method, J. Power Sources. 196 (2011) 8683–8687.

[30] J. Wolfenstine, J. Ratchford, E. Rangasamy, J. Sakamoto, J.L. Allen, Synthesis and high Li-ion conductivity of Ga-stabilized cubic $Li_7La_3Zr_2O_{12}$, Mater. Chem. Phys. 134 (2012) 571–575.

[31] D. Rettenwander, C.A. Geiger, G. Amthauer, Synthesis and crystal chemistry of the fast Li-ion conductor $Li_7La_3Zr_2O_{12}$ doped with Fe, Inorg. Chem. 52 (2013) 8005–

8009.

[32] Y. Zhang, F. Chen, R. Tu, Q. Shen, X. Zhang, L. Zhang, Effect of lithium ion concentration on the microstructure evolution and its association with the ionic conductivity of cubic garnet-type nominal $Li_7Al_{0.25}La_3Zr_2O_{12}$ solid electrolytes, Solid State Ionics. 284 (2016) 53–60.

[33] H. Buschmann, J. Dölle, S. Berendts, A. Kuhn, P. Bottke, M. Wilkening, P. Heitjans, A. Senyshyn, H. Ehrenberg, A. Lotnyk, V. Duppel, L. Kienle, J. Janek, Structure and dynamics of the fast lithium ion conductor "$Li_7La_3Zr_2O_{12}$," Phys. Chem. Chem. Phys. 13 (2011) 19378.

[34] L.J. Miara, S.P. Ong, Y. Mo, W.D. Richards, Y. Park, J.-M. Lee, H.S. Lee, G. Ceder, Effect of Rb and Ta Doping on the Ionic Conductivity and Stability of the Garnet $Li_{7+2x-y}(La_{3-x}Rb_x)(Zr_{2-y}Ta_y)O_{12}$ ($0 \leq x \leq 0.375$, $0 \leq y \leq 1$) Superionic Conductor: A First Principles Investigation, Chem. Mater. 25 (2013) 3048–3055.

[35] E. Hanc, W. Zając, J. Molenda, Synthesis procedure and effect of Nd, Ca and Nb doping on structure and electrical conductivity of $Li_7La_3Zr_2O_{12}$ garnets, Solid State Ionics. 262 (2014) 617–621.

[36] R. Murugan, V. Thangadurai, W. Weppner, Lattice parameter and sintering temperature dependence of bulk and grain-boundary conduction of garnet-like solid li-electrolytes, J. Electrochem. Soc. 155 (2008) A90–A101.

[37] S. Ohta, T. Kobayashi, T. Asaoka, High lithium ionic conductivity in the garnet-type oxide $Li_{7-X}La_3(Zr_{2-X}, Nb_X)O_{12}$ (X = 0-2), J. Power Sources. 196 (2011) 3342–3345.

[38] J.L. Allen, J. Wolfenstine, E. Rangasamy, J. Sakamoto, Effect of substitution (Ta, Al, Ga) on the conductivity of $Li_7La_3Zr_2O_{12}$, J. Power Sources. 206 (2012) 315–319.

[39] Y. Li, Z. Wang, Y. Cao, F. Du, C. Chen, Z. Cui, X. Guo, W-Doped $Li_7La_3Zr_2O_{12}$ Ceramic Electrolytes for Solid State Li-ion Batteries, Electrochim. Acta. 180 (2015) 37–42.

[40] Y. Li, J.-T. Han, C.-A. Wang, H. Xie, J.B. Goodenough, Optimizing Li+ conductivity in a garnet framework, J. Mater. Chem. 22 (2012) 15357.

[41] R. Inada, K. Kusakabe, T. Tanaka, S. Kudo, Y. Sakurai, Synthesis and properties of Al-free $Li_{7-X}La_3Zr_{2-x}Ta_xO_{12}$ garnet related oxides, Solid State Ionics. 262 (2014) 568–572.

[42] K. Liu, J.T. Ma, C.A. Wang, Excess lithium salt functions more than compensating for lithium loss when synthesizing $Li_{6.5}La_3Ta_{0.5}Zr_{1.5}O_{12}$ in alumina crucible, J. Power Sources. 260 (2014) 109–114.

[43] Y. Li, Y. Cao, X. Guo, Influence of lithium oxide additives on densification and ionic conductivity of garnet-type $Li_{6.75}La_3Zr_{1.75}Ta_{0.25}O_{12}$ solid electrolytes, Solid State Ionics. 253 (2013) 76–80.

[44] Y. Li, C.A. Wang, H. Xie, J. Cheng, J.B. Goodenough, High lithium ion conduction in garnet-type $Li_6La_3ZrTaO_{12}$, Electrochem. Commun. 13 (2011) 1289–1292.

[45] Y. Ren, T. Liu, Y. Shen, Y. Lin, C.-W. Nan, Chemical compatibility between garnet-like solid state electrolyte $Li_{6.75}La_3Zr_{1.75}Ta_{0.25}O_{12}$ and major commercial lithium

battery cathode materials, J. Mater. 2 (2016) 256–264.

[46] M. Kotobuki, K. Kanamura, Y. Sato, T. Yoshida, Fabrication of all-solid-state lithium battery with lithium metal anode using Al_2O_3-added $Li_7La_3Zr_2O_{12}$ solid electrolyte, J. Power Sources. 196 (2011) 7750–7754.

[47] E. Rangasamy, J. Wolfenstine, J. Sakamoto, The role of Al and Li concentration on the formation of cubic garnet solid electrolyte of nominal composition $Li_7La_3Zr_2O_{12}$, Solid State Ionics. 206 (2012) 28–32.

[48] T. Thompson, J. Wolfenstine, J.L. Allen, M. Johannes, A. Huq, I.N. David, J. Sakamoto, Tetragonal vs. cubic phase stability in Al-free Ta doped $Li_7La_3Zr_2O_{12}$ (LLZO), J. Mater. Chem. A. 2 (2014) 13431–13436.

[49] H. El-Shinawi, G.W. Paterson, D.A. MacLaren, E.J. Cussen, S.A. Corr, Low-temperature densification of Al-doped $Li_7La_3Zr_2O_{12}$: a reliable and controllable synthesis of fast-ion conducting garnets, J. Mater. Chem. A. 5 (2017) 319–329.

[50] R. Takano, K. Tadanaga, A. Hayashi, M. Tatsumisago, Low temperature synthesis of Al-doped $Li_7La_3Zr_2O_{12}$ solid electrolyte by a sol-gel process, Solid State Ionics. 255 (2014) 104–107.

[51] A.A. Hubaud, D.J. Schroeder, B. Key, B.J. Ingram, F. Dogan, J.T. Vaughey, Low temperature stabilization of cubic $(Li_{7-x}Al_{x/3})La_3Zr_2O_{12}$: Role of aluminum during formation, J. Mater. Chem. A. 1 (2013) 8813–8818.

[52] N. Rosenkiewitz, J. Schuhmacher, M. Bockmeyer, J. Deubener, Nitrogen-free sol-gel synthesis of Al-substituted cubic garnet $Li_7La_3Zr_2O_{12}$ (LLZO), J. Power Sources.

278 (2015) 104–108.

[53] S. Narayanan, V. Epp, M. Wilkening, V. Thangadurai, Macroscopic and microscopic Li+ transport parameters in cubic garnet-type "$Li_{6.5}La_{2.5}Ba_{0.5}ZrTaO_{12}$" as probed by impedance spectroscopy and NMR, RSC Adv. 2 (2012) 2553.

[54] E. Yi, W. Wang, J. Kieffer, R.M. Laine, Key parameters governing the densification of cubic- $Li_7La_3Zr_2O_{12}$ Li^+ conductors, J. Power Sources. 352 (2017) 156–164.

[55] Y.X. Gao, X.P. Wang, H. Lu, L.C. Zhang, L. Ma, Q.F. Fang, Mechanism of lithium ion diffusion in the hexad substituted $Li_7La_3Zr_2O_{12}$ solid electrolytes, Solid State Ionics. 291 (2016) 1–7.

[56] W. Xia, B. Xu, H. Duan, Y. Guo, H. Kang, H. Li, H. Liu, Ionic Conductivity and Air Stability of Al-Doped $Li_7La_3Zr_2O_{12}$ Sintered in Alumina and Pt Crucibles, ACS Appl. Mater. Interfaces. 8 (2016) 5335–5342.

[57] A. Lasia, Electrochemical Impedance Spectroscopy and its Applications, Springer, 2014.

[58] J.T.S. Irvine, D.C. Sinclair, A.R. West, Electroceramics: Characterization by Impedance Spectroscopy, Adv. Mater. 2 (1990) 132–138.

[59] K. Ishiguro, H. Nemori, S. Sunahiro, Y. Nakata, R. Sudo, M. Matsui, Y. Takeda, O. Yamamoto, N. Imanishi, Ta-Doped $Li_7La_3Zr_2O_{12}$ for Water-Stable Lithium Electrode of Lithium-Air Batteries, J. Electrochem. Soc. 161 (2014) A668–A674.

[60] C. Chen, Z. Lu, F. Ciucci, Data mining of molecular dynamics data reveals Li

diffusion characteristics in garnet $Li_7La_3Zr_2O_{12}$, Sci. Rep. 7 (2017) 40769.

[61] B. Andriyevsky, K. Doll, T. Jacob, Ab initio molecular dynamics study of lithium diffusion in tetragonal $Li_7La_3Zr_2O_{12}$, Mater. Chem. Phys. 185 (2017) 210–217.

[62] E.J. Cussen, M.P. O'Callaghan, A.S. Powell, J.J. Titman, G.Z. Chen, Switching on fast lithium ion conductivity in garnets: The structure and transport properties of $Li_{3+x}Nd_3Te_{2-x}Sb_xO_{12}$, Chem. Mater. 20 (2008) 2360–2369.

[63] Y. Zhang, F. Chen, J. Li, L. Zhang, J. Gu, D. Zhang, K. Saito, Q. Guo, P. Luo, S. Dong, Regulation mechanism of bottleneck size on Li^+ migration activation energy in garnet-type $Li_7La_3Zr_2O_{12}$, Electrochim. Acta. 261 (2018) 137–142.

[64] M.P. O'Callaghan, D.R. Lynham, E.J. Cussen, G.Z. Chen, Structure and ionic-transport properties of lithium-containing garnets $Li_3Ln_3Te_2O_{12}$ (Ln = Y, Pr, Nd, Sm-Lu), Chem. Mater. 18 (2006) 4681–4689.

[65] L. Truong, M. Howard, O. Clemens, K.S. Knight, P.R. Slater, V. Thangadurai, Facile proton conduction in H^+/Li^+ ion-exchanged garnet-type fast Li-ion conducting $Li_5La_3Nb_2O_{12}$, J. Mater. Chem. A. 1 (2013) 13469–13475.

[66] J.F. Wu, E.Y. Chen, Y. Yu, L. Liu, Y. Wu, W.K. Pang, V.K. Peterson, X. Guo, Gallium-doped $Li_7La_3Zr_2O_{12}$ garnet-type electrolytes with high lithium-ion conductivity, ACS Appl. Mater. Interfaces. 9 (2017) 1542–1552.

[67] T. Thompson, A. Sharafi, M.D. Johannes, A. Huq, J.L. Allen, J. Wolfenstine, J. Sakamoto, A tale of two sites: On defining the carrier concentration in Garnet-based ionic conductors for advanced Li batteries, Adv. Energy Mater. 5 (2015) 1–9.

[68] S. Song, D. Sheptyakov, A.M. Korsunsky, H.M. Duong, L. Lu, High Li ion conductivity in a garnet-type solid electrolyte via unusual site occupation of the doping Ca ions, Mater. Des. 93 (2016) 232–237.

[69] E.J. Cussen, T.W.S. Yip, A neutron diffraction study of the d0 and d10 lithium garnets $Li_3Nd_3W_2O_{12}$ and $Li_5La_3Sb_2O_{12}$, J. Solid State Chem. 180 (2007) 1832–1839.

[70] E.J. Cussen, The structure of lithium garnets: Cation disorder and clustering in a new family of fast Li^+ conductors, Chem. Commun. (2006) 412–413.

[71] M.P. O'Callaghan, E.J. Cussen, Lithium dimer formation in the Li-conducting garnets $Li_{5+x}Ba_xLa_{3-x}Ta_2O_{12}$ ($0 < x \leq 1.6$), Chem. Commun. (2007) 2048–2050.

[72] J. Percival, D. Apperley, P.R. Slater, Synthesis and structural characterisation of the Li ion conducting garnet-related systems, $Li_6ALa_2Nb_2O_{12}$ (A = Ca, Sr), Solid State Ionics. 179 (2008) 1693–1696.

[73] M.P. O'Callaghan, E.J. Cussen, The structure of the lithium-rich garnets $Li_6SrLa_2M_2O_{12}$ and $Li_{6.4}Sr_{1.4}La_{1.6}M_2O_{12}$ (M = Sb, Ta), Solid State Sci. 10 (2008) 390–395.

[74] E.J. Cussen, T.W.S. Yip, G. Oneill, M.P. Ocallaghan, A comparison of the transport properties of lithium-stuffed garnets and the conventional phases $Li_3Ln_3Te_2O_{12}$, J. Solid State Chem. 184 (2011) 470–475.

[75] A. Logéat, T. Köhler, U. Eisele, B. Stiaszny, A. Harzer, M. Tovar, A. Senyshyn, H. Ehrenberg, B. Kozinsky, From order to disorder: The structure of lithium-conducting garnets $Li_{7-x}La_3Ta_xZr_{2-x}O_{12}$ (x=0-2), Solid State Ionics. 206 (2012) 33–38.

[76] H. Xie, J.A. Alonso, Y. Li, M.T. Fernández-Díaz, J.B. Goodenough, Lithium distribution in aluminum-free cubic $Li_7La_3Zr_2O_{12}$, Chem. Mater. 23 (2011) 3587–3589.

[77] H. El-Shinawi, G.W. Paterson, D.A. MacLaren, E.J. Cussen, S.A. Corr, Low-temperature densification of Al-doped $Li_7La_3Zr_2O_{12}$: a reliable and controllable synthesis of fast-ion conducting garnets, J. Mater. Chem. A. 5 (2017) 319–329.

[78] J.B. Goodenough, Rechargeable batteries: Challenges old and new, J. Solid State Electrochem. 16 (2012) 2019–2029.

[79] H. Peng, Q. Wu, L. Xiao, Low temperature synthesis of $Li_5La_3Nb_2O_{12}$ with cubic garnet-type structure by sol–gel process, J. Sol-Gel Sci. Technol. 66 (2013) 175–179.

[80] X. Zhang, J. Fergus, Conductivity of Garnet-Type Lithium Lanthanum Zirconate Based Composite Electrolytes, ECS Trans. 85 (2018) 1531–1537.

[81] J. Wolfenstine, E. Rangasamy, J.L. Allen, J. Sakamoto, High conductivity of dense tetragonal $Li_7La_3Zr_2O_{12}$, J. Power Sources. 208 (2012) 193–196.

[82] A. Sharafi, C.G. Haslam, R.D. Kerns, J. Wolfenstine, J. Sakamoto, Controlling and correlating the effect of grain size with the mechanical and electrochemical properties of $Li_7La_3Zr_2O_{12}$ solid-state electrolyte, J. Mater. Chem. A. 5 (2017) 21491–21504.

[83] S. Patra, V. Krupa B R, S. Chakravarty, R. Murugan, Microstructural engineering in lithium garnets by hot isostatic press to cordon lithium dendrite growth and negate interfacial resistance for all solid state battery applications, Electrochim. Acta. (2019).

[84] Y. Suzuki, K. Kami, K. Watanabe, A. Watanabe, N. Saito, T. Ohnishi, K. Takada,

R. Sudo, N. Imanishi, Transparent cubic garnet-type solid electrolyte of Al_2O_3-doped $Li_7La_3Zr_2O_{12}$, Solid State Ionics. 278 (2015) 172–176.

[85] H. Yamada, T. Ito, R. Hongahally Basappa, Sintering Mechanisms of High-Performance Garnet-type Solid Electrolyte Densified by Spark Plasma Sintering, Electrochim. Acta. 222 (2016) 648–656.

[86] C. Li, Y. Liu, J. He, K.S. Brinkman, Ga-substituted $Li_7La_3Zr_2O_{12}$: An investigation based on grain coarsening in garnet-type lithium ion conductors, J. Alloys Compd. 695 (2017) 3744–3752.

[87] J.F. Wu, X. Guo, Size effect in nanocrystalline lithium-ion conducting perovskite: $Li_{0.30}La_{0.57}TiO_3$, Solid State Ionics. 310 (2017) 38–43.

[88] M. Botros, R. Djenadic, O. Clemens, M. Möller, H. Hahn, Field assisted sintering of fine-grained $Li_{7-3x}La_3Zr_2Al_xO_{12}$ solid electrolyte and the influence of the microstructure on the electrochemical performance, J. Power Sources. 309 (2016) 108–115.

[89] Y. Deng, C. Eames, J.-N. Chotard, F. Lalère, V. Seznec, S. Emge, O. Pecher, C.P. Grey, C. Masquelier, M.S. Islam, Structural and Mechanistic Insights into Fast Lithium-Ion Conduction in Li_4SiO_4–Li_3PO_4 Solid Electrolytes, J. Am. Chem. Soc. 137 (2015) 9136–9145.

[90] S. Patra, V. Krupa B R, S. Chakravarty, R. Murugan, Microstructural engineering in lithium garnets by hot isostatic press to cordon lithium dendrite growth and negate interfacial resistance for all solid state battery applications, Electrochim. Acta. 312

(2019) 320–328.

[91] N. Janani, C. Deviannapoorani, L. Dhivya, R. Murugan, Influence of sintering additives on densification and Li^+ conductivity of Al doped $Li_7La_3Zr_2O_{12}$ lithium garnet, RSC Adv. 4 (2014) 51228–51238.

[92] X. Huang, C. Shen, K. Rui, J. Jin, M. Wu, X. Wu, Z. Wen, Influence of $La_2Zr_2O_7$ Additive on Densification and Li^+ Conductivity for Ta-Doped $Li_7La_3Zr_2O_{12}$ Garnet, JOM. 68 (2016) 2593–2600.

[93] N.C. Rosero-Navarro, T. Yamashita, A. Miura, M. Higuchi, K. Tadanaga, J.W. Stevenson, Effect of Sintering Additives on Relative Density and Li-ion Conductivity of Nb-Doped $Li_7La_3Zr_2O_{12}$ Solid Electrolyte, J. Am. Ceram. Soc. 100 (2017) 276–285.

[94] N.C. Rosero-Navarro, T. Yamashita, A. Miura, M. Higuchi, K. Tadanaga, Preparation of $Li_7La_3(Zr_{2-x},Nb_x)O_{12}$ (x=0–1.5) and $Li_3BO_3/LiBO_2$ composites at low temperatures using a sol–gel process, Solid State Ionics. 285 (2015) 6–12.

[95] J. Wolfenstine, H. Jo, Y.H. Cho, I.N. David, P. Askeland, E.D. Case, H. Kim, H. Choe, J. Sakamoto, A preliminary investigation of fracture toughness of $Li_7La_3Zr_2O_{12}$ and its comparison to other solid Li-ionconductors, Mater. Lett. 96 (2013) 117–120.

[96] X. Han, Y. Gong, K. (Kelvin) Fu, X. He, G.T. Hitz, J. Dai, A. Pearse, B. Liu, H. Wang, G. Rubloff, Y. Mo, V. Thangadurai, E.D. Wachsman, L. Hu, Negating interfacial impedance in garnet-based solid-state Li metal batteries, Nat. Mater. 16 (2016) 572–579.

[97] F. Croce, G.B. Appetecchi, L. Persi, B. Scrosati, Nanocomposite polymer

electrolytes for lithium batteries, Nature. 394 (1998) 456–458.

[98] J.-H.H. Choi, C.-H.H. Lee, J.-H.H. Yu, C.-H.H. Doh, S.-M.M. Lee, Enhancement of ionic conductivity of composite membranes for all-solid-state lithium rechargeable batteries incorporating tetragonal $Li_7La_3Zr_2O_{12}$ into a polyethylene oxide matrix, J. Power Sources. 274 (2015) 458–463.

[99] J. Zheng, H. Dang, X. Feng, P.-H. Chien, Y.-Y. Hu, Li-ion transport in a representative ceramic–polymer–plasticizer composite electrolyte: Li7La3Zr2O12-polyethylene oxide-tetraethylene glycol dimethyl ether, J. Mater. Chem. A. (2017).

[100] S.H.S. Cheng, K.Q. He, Y. Liu, J.W. Zha, M. Kamruzzaman, R.L.W. Ma, Z.M. Dang, R.K.Y. Li, C.Y. Chung, Electrochemical performance of all-solid-state lithium batteries using inorganic lithium garnets particulate reinforced PEO/$LiClO_4$ electrolyte, Electrochim. Acta. 253 (2017) 430–438.

[101] T. Yang, J. Zheng, Q. Cheng, Y.Y. Hu, C.K. Chan, Composite Polymer Electrolytes with $Li_7La_3Zr_2O_{12}$ Garnet-Type Nanowires as Ceramic Fillers: Mechanism of Conductivity Enhancement and Role of Doping and Morphology, ACS Appl. Mater. Interfaces. 9 (2017) 21773–21780.

[102] K. (Kelvin) Fu, Y. Gong, J. Dai, A. Gong, X. Han, Y. Yao, C. Wang, Y. Wang, Y. Chen, C. Yan, Y. Li, E.D. Wachsman, L. Hu, Flexible, solid-state, ion-conducting membrane with 3D garnet nanofiber networks for lithium batteries, Proc. Natl. Acad. Sci. 113 (2016) 7094–7099.

[103] K. Tadanaga, R. Takano, T. Ichinose, S. Mori, A. Hayashi, M. Tatsumisago, Low

temperature synthesis of highly ion conductive $Li_7La_3Zr_2O_{12}$-Li_3BO_3 composites, Electrochem. Commun. 33 (2013) 51–54.

[104] R.H. Shin, S.I. Son, Y.S. Han, Y. Do Kim, H.T. Kim, S.S. Ryu, W. Pan, Sintering behavior of garnet-type $Li_7La_3Zr_2O_{12}$-Li_3BO_3 composite solid electrolytes for all-solid-state lithium batteries, Solid State Ionics. 301 (2017) 10–14.

[105] E. Rangasamy, G. Sahu, J.K. Keum, A.J. Rondinone, N.J. Dudney, C. Liang, A high conductivity oxide-sulfide composite lithium superionic conductor, J. Mater. Chem. A. 2 (2014) 4111–4116.

[106] K. Chen, M. Huang, Y. Shen, Y. Lin, C.W. Nan, Improving ionic conductivity of $Li_{0.35}La_{0.55}TiO_3$ ceramics by introducing $Li_7La_3Zr_2O_{12}$ sol into the precursor powder, Solid State Ionics. 235 (2013) 8–13.

[107] E. Rangasamy, G. Sahu, J.K. Keum, A.J. Rondinone, N.J. Dudney, C. Liang, A high conductivity oxide–sulfide composite lithium superionic conductor, J. Mater. Chem. A. 2 (2014) 4111–4116.

[108] S.H.-S. Cheng, K.-Q. He, Y. Liu, J.-W. Zha, M. Kamruzzaman, R.L.-W. Ma, Z.-M. Dang, R.K.Y. Li, C.Y. Chung, Electrochemical performance of all-solid-state lithium batteries using inorganic lithium garnets particulate reinforced PEO/$LiClO_4$ electrolyte, Electrochim. Acta. (2017).

[109] N.C.C. Rosero-Navarro, T. Yamashita, A. Miura, M. Higuchi, K. Tadanaga, Preparation of $Li_7La_3(Zr_{2-x}, Nb_x)O_{12}$ (x = 0-1.5) and $Li_3BO_3/LiBO_2$ composites at low temperatures using a sol-gel process, Solid State Ionics. 285 (2016) 6–12.

[110] A.A. Coelho, TOPAS and TOPAS-Academic: An optimization program integrating computer algebra and crystallographic objects written in C++: An, J. Appl. Crystallogr. 51 (2018) 210–218.

[111] D. Mazza, Remarks on a ternary phase in the $La_2O_3Me_2O_5Li_2O$ system (Me=Nb, Ta), Mater. Lett. 7 (1988) 205–207.

[112] I. Kokal, M. Somer, P.H.L. Notten, H.T. Hintzen, Sol-gel synthesis and lithium ion conductivity of $Li_7La_3Zr_2O_{12}$ with garnet-related type structure, Solid State Ionics. 185 (2011) 42–46.

[113] S. Nasrazadani, S. Hassani, Modern analytical techniques in failure analysis of aerospace, chemical, and oil and gas industries, 2016.

[114] V. Thangadurai, W. Weppner, $Li_6ALa_2Nb_2O_{12}$ (A = Ca, Sr, Ba): A new class of fast lithium ion conductors with garnet-like structure, J. Am. Ceram. Soc. 88 (2005) 411–418.

[115] V. Thangadurai, D. Pinzaru, S. Narayanan, A.K. Baral, Fast Solid-State Li Ion Conducting Garnet-Type Structure Metal Oxides for Energy Storage, J. Phys. Chem. Lett. 6 (2015) 292–299.

[116] S. Smetaczek, M. Bonta, A. Wachter-Welzl, S. Taibl, R. Wagner, D. Rettenwander, J. Fleig, A. Limbeck, Spatially resolved stoichiometry determination of $Li_7La_3Zr_2O_{12}$ solid-state electrolytes using LA-ICP-OES, J. Anal. At. Spectrom. 35 (2020) 972–983.

[117] M. Wang, J. Sakamoto, Correlating the interface resistance and surface adhesion of the Li metal-solid electrolyte interface, J. Power Sources. 377 (2018) 7–11.

[118] M. Keller, G.B. Appetecchi, G.T. Kim, V. Sharova, M. Schneider, J. Schuhmacher, A. Roters, S. Passerini, Electrochemical performance of a solvent-free hybrid ceramic-polymer electrolyte based on $Li_7La_3Zr_2O_{12}$ in $P(EO)_{15}$LiTFSI, J. Power Sources. 353 (2017) 287–297.

[119] D.K. Schwanz, A. Villa, M. Balasubramanian, B. Helfrecht, E.E. Marinero, Ionic conductivity enhancements and low temperature synthesis of $Li_7La_3Zr_2O_{12}$ garnets by Bi aliovalent substitutions, n.d.

[120] H. Hou, L. Cheng, T. Richardson, G. Chen, M. Doeff, R. Zheng, R. Russo, V. Zorba, Three-dimensional elemental imaging of Li-ion solid-state electrolytes using fs-laser induced breakdown spectroscopy (LIBS), J. Anal. At. Spectrom. 30 (2015) 2295–2302.

[121] J. Christensen, P. Albertus, R.S. Sanchez-Carrera, T. Lohmann, B. Kozinsky, R. Liedtke, J. Ahmed, A. Kojic, A critical review of Li/air batteries, J. Electrochem. Soc. 159 (2012) R1–R30.

[122] K.B. Dermenci, E. Çekiç, S. Turan, Al stabilized $Li_7La_3Zr_2O_{12}$ solid electrolytes for all-solid state Li-ion batteries, Int. J. Hydrogen Energy. 41 (2016) 9860–9867.

[123] J. Hu, R.E. Sturgeon, K. Nadeau, X. Hou, C. Zheng, L. Yang, Copper Ion Assisted Photochemical Vapor Generation of Chlorine for Its Sensitive Determination by Sector Field Inductively Coupled Plasma Mass Spectrometry, Anal. Chem. 90 (2018) 4112–4118.

[124] N.S. Kulkarni, T.M. Besmann, K.E. Spear, Thermodynamic optimization of

lithia-alumina, J. Am. Ceram. Soc. 91 (2008) 4074–4083.

[125] S.S. Lee, Y.J. Lim, H.W. Kim, J.K. Kim, Y.G. Jung, Y. Kim, Electrochemical properties of a ceramic-polymer-composite-solid electrolyte for Li-ion batteries, Solid State Ionics. 284 (2016) 20–24.

[126] L. Chen, Y. Li, S.P. Li, L.Z. Fan, C.W. Nan, J.B. Goodenough, PEO/garnet composite electrolytes for solid-state lithium batteries: From “ceramic-in-polymer” to “polymer-in-ceramic,” Nano Energy. 46 (2018) 176–184.

[127] F. Langer, I. Bardenhagen, J. Glenneberg, R. Kun, Microstructure and temperature dependent lithium ion transport of ceramic–polymer composite electrolyte for solid-state lithium ion batteries based on garnet-type $Li_7La_3Zr_2O_{12}$, Solid State Ionics. 291 (2016) 8–13.

[128] X. Zhang, L. Zhou, Y. Wang, Q. Zhou, Influence of Humidity on the Complex Structure of PEO-Lithium Salt Polymer Electrolyte, Polym. Sci. - Ser. A. 60 (2018) 50-56.

[129] L. Chen, Y. Li, S.P. Li, L.Z. Fan, C.W. Nan, J.B. Goodenough, PEO/garnet composite electrolytes for solid-state lithium batteries: From “ceramic-in-polymer” to “polymer-in-ceramic,” Nano Energy. 46 (2018) 176–184.

[130] F. Langer, M.S. Palagonia, I. Bardenhagen, J. Glenneberg, F. La Mantia, R. Kun, Impedance Spectroscopy Analysis of the Lithium Ion Transport through the $Li_7La_3Zr_2O_{12}$/$P(EO)_{20}Li$ Interface, J. Electrochem. Soc. 164 (2017) A2298–A2303.